FUNCTIONAL ASSESSMENTS OF PLATELET-DERVIED GROWTH FACTOR GENE DELIVERY ON ACCELERATING ORAL IMPLANT OSSEOINTEGRATION

By

Po-Chun Chang

A dissertation submitted in partial fulfillment
of the requirements for the degree of
Doctor of Philosophy
(Biomedical Engineering)
in The University of Michigan
2009

Doctoral Committee:

Professor William V. Giannobile, Chair
Professor Steven A. Goldstein
Professor Noboru Kikuchi
Professor Paul H. Krebsbach

DEDICATION

To My Beloved Family

ACKNOWLEDGEMENTS

First of all, I would like to express my sincere thanks and gratitude to my advisor, Professor William V. Giannobile, for his valuable mentorship and support throughout the period of Ph.D work. His expertise in periodontology and tissue engineering provided me the insight of research, kept me on the right direction of study, and helped to develop my own philosophy on the academics. I would also like to thank the great support from my dissertation committee members: Professor Steven A. Goldstein, Professor Noboru Kikuchi, and Professor Paul H. Krebsbach. They not only generous searched and share the resources, but their critique also helped me to think deeper and pointed out important issues I neglected.

A great work could not be achieved solely. I am very lucky to stay and work with a wonderful lab group in a friendly environment, and I would like to express my appreciation to the “research family” in Giannobile Lab. James V. Sugai, the manager of the lab, is like the mother in the lab. He not only helped organizing the lab and grant stuff,

but he also assisted the experiments as well as negotiation in this family. Dr. Qiming Jin, an experienced researcher and surgeon, provided me numerous valuable instructions and advises on the research. Based on the high-quality surgery from Professor Joni A. Cirrelli and Dr. Yang-Jo Seol, the research was able to complete effectively and achieve favorable outcomes. Chan Ho Park, my PhD colleague in Biomedical Engineering, usually offered me the thought from engineering side and helped me to develop a more comprehensive research plan. Dr. Zhao Lin instructed me several molecular biology techniques as well as assisted in several experiments. Lea Franco, our lab specialist, helped me to organize the surgical stuff and lab activities. I was always encouraged by Dr. Hector Rios and Dr. Julie Marchesan, although we did not have too much overlap on research, they were always interested in my projects and pointed out several tricks to make my presentation better. I would also like to thank Dr. Gaia Pellegrini, Dr. Valeria P.N. Tedeschi, Dr. Reinhard Gruber, Dr. Salvatore Batia, Dr. Andrea Ottonello, Katie MacKool, Lindsay Rayburn, Zachary Abramson, Michelle Webb, Ashley Chung, Megan Bland, TJ Daws, and Nancy Chen, for their help during my PhD stage.

As an engineering PhD student without any engineering background, I would like to thank the Department of Biomedical Engineering for giving me great opportunities to

learn engineering, and the Orthopaedic Research Laboratory providing me valuable resources to make it biologically available, especially for the great support from Jeff Megnack, Jacklynn Kreider, and Edward Sihler in establishing the micro-CT protocol and troubleshooting, and Dennis Kayner, a key man for making the custom dental step drills and performing the push-out test. I also appreciate the technical support of process resin-embedding specimens from Rochelle Taylor.

Besides, I would also like to thank the ULAM staffs, especially the technical support from Dan Hall, Amanda Welton, Anna Colvig, Rob Mcnish, and Dr. John Erby Wilkinson, and acknowledge the help from the faculty and staff in the School of Dentistry, including Dr. Taocong Jin's instruction and assistance on the PCR analysis, Dr. Nisha J. D'Silva and Dr. Theodore E. Danciu's effort on examining the histologic sections, and Dr. Helena Ritchie's generous support in the facility of preparing the specimens.

I would also like to acknowledge the financial support from NIH/NIDCR grant (DE13397), AO Foundation, and ITI Foundation, and the generous gifts from ITI Institut for the mini-titanium implants, and Tissue Repair Company for the gene-activated matrix and adenovirus vectors.

The last, but the most important, I want to address my gratitude and dedicate this dissertation for my family, for their endless love, tolerance, patience, and support during my PhD study.

TABLE OF CONTENTS

LIST OF FIGURES

LIST OF TABLES

ABSTRACT

The main purpose of dental implants is to restore the function of the dentition. Despite utilizing structural analyses to investigate treatment outcomes, the therapeutic effect is sometimes unclear due to a lack of direct relevance to the biomechanical function of the peri-implant tissue. While the effective function of tissue depends on the growth pattern, maturation, and load bearing situation of the apparatus, in this dissertation I homogenized the peri-implant tissue parameters under simulated loading situations to generate functional bone apparent modulus (FBAM) and functional composite tissue apparent modulus (FCAM) through the finite element (FE) optimization process. Both FBAM and FCAM were correlated to the structural parameters, and FCAM was determined to be more relevant to interfacial biomechanical characteristics with a pre-existing extraction defect, whereas FBAM within a 200 μm peri-implant concentric layer was more relevant to the implant osteotomy defect.

Platelet-derived growth factor (PDGF) has been utilized for periodontal tissue

regeneration based on its effects on chemotaxis and mitogenesis, which are also key events which occur during early osseointegration. However, the bioactivity of recombinant growth factor application may be significantly reduced due to its rapid degradation and diffusion *in vivo*. To ensure the efficiency of PDGF expression, we delivered PDGF to peri-implant osseous defects using adenovirus gene therapy vectors (AdPDGF-B) and evaluated the treatment outcome histologically, radiographically, and functionally. The results demonstrate that AdPDGF-B significantly accelerates defect fill and promotes early bone-implant contact (BIC) in a dose-dependent manner. AdPDGF-B also facilitated favorable functional implant support in the early stages of osseointegration.

There also exist some considerations regarding the potential of adenovirus-mediated gene therapy to induce virus-related pathologic changes. Thus, the local and systemic safety profile of AdPDGF-B was thoroughly examined in this dissertation in order to alleviate concerns about future gene therapy applications for clinical use. AdPDGF-B was eliminated within two weeks without significant dissemination *in vivo*, and no histopathologic changes or alterations of systemic parameters were noted. Taken together, this dissertation contributes a novel methodology to functionally evaluate the dynamics

of osseointegration and demonstrates the feasibility of AdPDGF-B for accelerating osseointegration while maintaining an acceptable safety profile.

CHAPTER 1

INTRODUCTION

1.1 Dental Implant Osseointegration: Mechanisms and Clinical Significance

Osseointegration, which histologically is defined as direct bone-to-implant contact, is believed to provide rigid fixation of a dental implant within the alveolar bone and can promote the long-term success of dental implants [1,2]. The process of osseointegration involves an initial interlocking between alveolar bone and the implant fixture (primary implant stability), and later, biological fixation through continuous bone apposition and remodeling toward the dental implant (secondary implant stability) [3].

While Soballe and colleagues [4] demonstrated that excessive mobility may cause fibrous tissue formation and lead to failure of osseointegration, in order to limit the micromotion and achieve primary stability of the implant, a slightly undersized osteotomy is usually performed for press-fitting of the implant. However, a ~60 micrometer gap between the implant and host bone has been noted under microscopic investigations [5,6], and depending on the extent of injury to the host bone, this gap may

later extend to 100-500 micrometers [7]. Therefore, this gap is covered with blood and forms a water layer incorporated with hydrated ions on implant surfaces immediately after placement [3,8]. The small proteins adsorbed on the surface are subsequently replaced by larger proteins based on the 'Vroman effect'. Although the different implant surface properties may affect the composition and conformational states of the binding proteins, the biological aggregates on the surface interact with the cell extensions, cell membrane, or membrane-bound proteins or receptors, and initial cell attachment eventually establishes on the implant surface [9]. The interface area is first occupied by red blood cells, inflammatory cells, and degenerating cellular elements, then is gradually replaced with spindle-shaped or flattened cells, concurrent with initiation of osteolysis on the host bone surface until day 3 [6]. Osteoblasts begin to attach and deposit a collagen matrix at this stage [10].

Early bone formation is not evident until days 5-7 [3,5] and is consistent with the sequence of appositional matrix deposition and calcification from the lamina limitans of host bone onto the implant surface [11]. Most of the interfacial zone is occupied by provisional matrix rich in collagen fibrils and vasculature, and woven bone can be observed around the vascular areas by day seven [3]. Through continuous deposition, trabecular bone fills the

initial gap and arranges in a three-dimensional network by day fourteen [1]. The *de novo* formation of primary bone spongiosa offers not only a biological fixation to ensure secondary implant stability [12], but also a biological scaffold for cell attachment and bone deposition [1]. After 28 days, a delineated bone marrow space and thickened bone trabeculae with parallel-fibered and lamellar bone can be found within the interfacial area. After 8 to 12 weeks, the interfacial area appears histologically to be completely replaced by mature lamellar bone in direct contact with titanium [3].

1.2 Current Assessments of Dental Implant Osseointegration

Stiffness of the tissue-implant interface and implant-supporting tissues is considered as the main determinant factors in osseointegration [13,14]. While the structure and heterogeneity of mineralization affects the stiffness of bone [15], Johansson et al [16] demonstrated that biomechanical testing may be a more suitable indicator to evaluate the dynamic changes of osseointegration than any single structural parameter. However, biomechanical testing, such as push-out and pull-out measurements, is destructive and only available for preclinical use [17]. The clinical value of non-destructive measurements, such as resonance frequency analysis (RFA) or damping characteristics by the Periotest technique, remain limited due to the lower resolution and higher variability during examinations [18]. Thus, development of effective approaches to functionally assess osseointegration for the evaluation of peri-implant wound healing and prognosis of implant therapy would be of significant clinical value.

1.2.1 Preclinical Biomechanical Assessments for Osseointegration

Tensional Test

The interfacial tensile strength was originally measured by detaching the implant plate from the supporting bone [19]. Branemark later modified this technique by applying

the lateral load to the cylindrical fixture [20] (Fig 1.1a). However, they also addressed the difficulties of translating the test results to any area-independent mechanical properties.

Push-out and Pull-out Testing

The 'push-out' or 'pull-out' test is the most commonly used approach to investigate the healing capabilities within the bone-implant interface [21,22]. In the typical push-out or pull-out test, a cylinder-type implant is placed transcortically or intramedullarly in bone structures and then removed by applying a force parallel to the interface (Fig 1.1b,c). The maximum load capability (or failure load) is defined as the maximum force on the force-displacement plot, and the interfacial stiffness is visualized as the slope of a tangent approximately at the linear region of the force-displacement curve prior to breakpoint [22,23]. Therefore, the general loading capacity of the interface (or interfacial shear strength) can be measured by dividing the maximum force by the area of the implant in contact with the host bone [17]. However, the push-out and pull-out tests are only applicable for non-threaded cylinder-type implants, whereas most of clinically available fixtures are of threaded design, and their interfacial failures are solely dependent on shear stress without any consideration for either tensile or compressive stresses [22].

Removal Torque

The removal torque refers to the torsional force necessary for unscrewing the fixture (Fig 1.1d) and was first investigated by Johansson and Albrektsson [16]. The removal torque value was recorded using a torque manometer calibrated in Newton-centimeters. This technique primarily focuses on interfacial shear properties, however the results may be affected by implant geometry and topography [24,25].

Combination Trial

A trial was introduced by Branemark and colleagues by applying torsional force until reaching the maximum torque and then pulling the implant out [20]. In this investigation, the removal torque was related to the interfacial bonding capability, and the pull-out strength was related to the shear properties from the implant-supporting structure.

1.2.2 Clinical Biomechanical Assessments for Osseointegration

Cutting Resistance/Insertional Torque

The cutting resistance refers to the energy required in cutting of a unit volume of bone [26] while the insertional torque occurs during the fixture tightening procedure [27].

Both of these measurements apply to the lateral compression force and friction at the interface during implant insertion and are mainly influenced by the tolerance of the fixture thread design [28]. Many researchers have also used the peak insertional torque value, which is generated during the final fixture tightening step, as an indicator of primary implant stability. A positive correlation between insertional and removal torque is evident however, any relationship between the cutting resistance and the peak insertional torque is still unclear [29].

Periotest

Significant deformation of the bone-implant unit is not measurable for most clinical situations. To overcome this limitation, damping characteristics, or the dynamic tissue recovery processes after loading, were recommended for noninvasive assessment of osseointegration [18]. The Periotest (Siemens, Bensheim, Germany) was originally designed to assess the damping characteristics of the periodontal ligament (PDL) for teeth by calculating the contact time between the test subject and the percussion rod (Figure 1e) and are reported as Periotest value (PTV) [30].

The main limitation of the Periotest is a lack of sensitivity in evaluating

osseointegration, whereby the range of PTV in osseointegrated implants falls to a narrow zone (-5 to +5) within a wide scale (-8 to +50) [31]. This could be accounted for by physical differences between alveolar bone and the bone-implant interface, because bone is much stiffer and does not allow for significant deformation as compared to the soft tissue of the periodontium [25]. Moreover, results may also be influenced by the position and direction of the percussion rod [32].

Resonance Frequency Analysis (RFA)

RFA was first introduced by Meredith and co-workers [25]. They utilized an L-shaped transducer connected to the implant to provide a high frequency mechanical vibration and record the frequency and amplitude of the signal received (Fig 1.1f). The resonance frequency was thus defined as the peak of the frequency-amplitude plot and converted to a value representing stiffness of the bone-implant interface. Currently, Osstell (Integration Diagnostic AB, Goteborg, Sweden), a commercialized product utilizing the concept of RFA, has translated the resonance frequency ranging from 3000 to 8500 Hz as the implant stability quotient (ISQ) of 0 to 100 [33].

While moderate to strong correlation is found between cutting resonance and ISQ

value upon implant placement [13,34], and because of the noninvasive nature of the measurement, RFA has been widely used for clinically assessing osseointegration, as well as for prognostic evaluation [18,25]. However, RFA measurement is still somewhat affected by the orientation and position of the transducer [25].

1.2.3 Relevance of the Peri-Implant Structure to Interfacial Biomechanics

Considering that intrinsic properties of the peri-implant bone may affect the stiffness of bone-implant interface [22,35], a number of studies have attempted to provide insight into the correlation between peri-implant structure and implant stability (Tables 1.1 and 1.2).

Correlations between Primary Implant Stability and Peri-Implant Structures

The relationship between the primary implant stability and peri-implant structures was first reported by Niimi and colleagues [36]. They applied torque to implants within the fibulae, iliac crest, and scapula of human cadavers and found that the removal torque value was significantly correlated to cortical bone thickness but was not associated with the trabecular bone area based on histological sections. This same correlation was also observed in a later investigation using implant pull out methods from dog mandibulae [37].

Primary implant stability can also be related to the bone mineral density (BMD) by analyzing and interpreting three-dimensional (3D) computed tomography (CT) images [13,38], and is strongly correlated with increasing implant diameter [13]. Akca et al also found significant correlation between the trabecular bone structure and the insertional torque value [39]. However, most of these investigations also revealed that the insertional torque value tended to be more sensitive to the peri-implant structure than the ISQ value (Table 1.1).

Correlations between Secondary Implant Stability and Peri-Implant Structures

A prior animal study first demonstrated a similar tendency of change in removal torque value and bone-implant contact over a period of time [16], demonstrating that results could be influenced by implant topography or metal biocompatibility [16]. However, a relationship between the amount of bone within the threaded area and the removal torque value could not fully elucidated using these approaches due to a lack of available clinical biomechanical assessments or more definitive imaging techniques [40].

Measuring specimens during and after implant removal, Branemark and co-workers demonstrated that the total bone thickness (TBT) 50 μm from the interface and bone

implant contact area (BIC) were significantly correlated to the maximal and breakpoint torque, and the TBT also strongly correlated to the subsequent pull-out force [20]. The correlation between insertional torque value and cortical bone thickness was recently reported [41]. However, the opposite result was found from a study on dog mandibulae, where the pull-out force was correlated to primary implant stability, but this correlation became non-significant in the latter healing stages [37].

Using non-destructive biomechanical assessments (i.e., Periotest, RFA) on dog mandibulae, a high correlation was found between the mechanical impedance from the Periotest and BIC as well as bone density from histology and radiography at 3 months post-implantation[14]. Sykaras et al also demonstrated significant correlation between PTV and BIC based on histology, however, using a different treatment modality such as the pull-out test, the PTV was not sensitive to the osseous wound repair [42]. Modest correlations between ISQ value and BIC have been shown in some reports [43,44], while others have not observed a correlation [45].

Recent investigations utilizing micro-CT technology have demonstrated moderate to strong correlations between the structural parameters (i.e., BIC, bone volume, trabecular

bone thickness, trabecular number, and connectivity density) and pull-out results. Different treatment strategies resulted in similar a correlation between the biomechanical and structural properties [46].

1.3 Approaches for Enhancing Osseointegration

The chemical composition of the implant interface or its charges on the implant surface were shown to affect initial cell attachment [9]. This has aroused concern for using implant surface modification as a way to accelerate the rate of osseointegration. The general aspect of this philosophy is to modify the surface topography by chemical or mechanical treatments, which can mediate cell behavior via the surface energy. Surface coating, including plasma-sprayed hydroxyapatite and bio-adhesive motifs from biomimetic approaches, in order to promote cell attachment and matrix deposition on the interface is also under investigation. Another strategy to promote osseointegration is to deliver osteogenic factors, such as bone morphogenetic proteins (BMPs) or platelet-derived growth factors (PDGFs), and several delivery modes had been tested for ensuring the efficiency of the treatment.

1.3.1 Implant Surface Alteration

Surface Roughness

Depending on the scale of the features, surface roughness can be divided into three categories: macro- (roughness > 10 μm), micro- (roughness 1-10 μm), and nano-topographies (roughness < 1 μm) [47]. Macro-level roughness is associated with

implant geometry, such as screw structure, and macroporous surface treatments. Previous studies demonstrated that this higher roughness allowed for bone ongrowth and provided mechanical interlocking shortly after implant placement [1,3]. Higher BIC and removal torque force suggested enhanced secondary stability compared to smooth-cylinder implants [40,48].

There are two main theories regarding the influence of implant surface microtopography on peri-implant tissue formation – 1) the surface energy and 2) the distortional strain. The smaller grain size on the surface results in higher surface energy, which is more favorable for cell adherence [49,50]. Bowers and colleague [51] first demonstrated that the intermediate roughness with sandblasted and acid-etching treatments significantly promoted cell attachment. Anselme and Bigerelle [52] later investigated long-term osteoblast adherence and behavior *in vitro* and demonstrated that a low amplitude of the surface roughness induced cell spreading more intimately than the rougher one. Therefore, the microtopography of the implant surface also influences differentiation events by providing the distortional signals. While osteoblastic cells show a cuboidal shape with polarized nuclei, the inactive bone-lining cells tended to have a flattened morphology without polarization [53]. Later studies further demonstrated that

minor distortional strain and low compressive hydrostatic stress on mesenchymal stem cells were most likely for promoting osteogenic differentiation, whereas excessive distortional strain resulted in fibrogenesis as well as chondrogenesis, due to significant hydrostatic pressure [54]. Based on the mesenchymal cell size of about 5 to 12 μm in length, surface microtopographic pits with a 4 μm diameter and 1.5 μm depth are thought to be optimal for cells to attach and subsequently differentiate on the implant surface [55,56].

Based on the large proportion of grain boundaries increasing surface energy, significant enhancement of cell attachment, proliferation, viability, spreading, and early osteogenic differentiation on these nano-/ultrafine-grained structures has been demonstrated in several investigations [57-59]. However, reproducible surface roughness on a nanoscale level is difficult to achieve, thus optimal surface nanotopography for rapid osseointegration is still not achievable [47].

Surface Coating and Biomimetic Approaches

Another category of implant surface modification is to coat the implant with layers of bioactive materials. One approach is to coat the titanium surface of implants with calcium phosphates, mainly composed of hydroxyapatite (HA), by plasma-spraying. The

calcium phosphates are released to the peri-implant area after implantation and precipitated biological apatites, which serve as matrices for subsequent osteogenic cell attachment and growth [47]. Compared to a titanium surface without coating, osteogenic cells attach, proliferate, and differentiate on the HA-coated surface [60], and result in superior initial rates of osseointegration *in vivo* [61]. However, the delamination of the coating and particle release from the implant surface causes long-term failure in some studies [62,63]. To prevent this, recent investigations have focused on depositing HA onto the implant surface through biomimetic approaches, such as electrodeposition or immersion in SBF [47].

Implant surfaces may be also coated with the biomolecules, such as bio-adhesive motifs or growth factors, to enhance osseointegration. The RGD sequence from fibronectin is the most commonly used bio-adhesive motif, which binds adhesion receptors and promotes cell adhesion [64]. RGD-functionalized, tissue-engineered constructs have shown improvement during early bone ingrowth and matrix mineralization *in vivo* [23,65]. However, RGD immobilization on titanium implant surfaces has not improved bone-implant contact or osteoblast differentiation [45,66], presumably due to neglecting the conformation-dependent effects and absence of crucial modulatory

domains from the native fibronectin, thus diminishing the RGD signals through non-specific adsorption of plasma protein and interactions with inflammatory components [67].

1.3.2 Growth Factor Applications

The rate of osseointegration is dependent on the matrix synthesis, replication, and differentiation of osteoprogenitor cells, and on interfacial tissue maturation [22,68]. Since growth factors, such as BMP-2 and platelet-derived growth factor (PDGF), enhance osteogenesis and were suggested to regenerate the periodontal and dentoalveolar tissues [69,70], several of those biomolecules were also introduced to accelerate peri-implant wound healing and osseointegration.

Bone Morphogenetic Proteins (BMPs)

Belonging to the transforming growth factor-beta (TGF-β) superfamily, BMPs have been proven to drive the multipotent cells into an osteogenic lineage and promote extracellular matrix formation through the Smad signaling pathway [71]. Among all of the BMPs isoforms, BMP-2 and BMP-7 are the most commonly investigated. BMP can induce ectopic and periosteal bone formation *in vivo* [72,73]. Within the dental field, BMP

has been shown to promote tooth extraction socket healing, peri-implant wound healing, and sinus floor and alveolar ridge augmentation in preclinical studies [74-77]. Some investigations have also reported that BMP exhibits superior short- but not long-term effects over controls [78-80]. A commercialized BMP-2 formulation (Infuse®, Medtronic Inc., Memphis, TN, USA) has been made clinically available. In clinical trials, BMP tended to accelerate extraction socket and alveolar ridge augmentation compared to collagen vehicle alone within the period of 4-6 months [81,82]. However, no significant difference could be found between BMP application and bone grafting in the treatment of sinus floor and alveolar ridge augmentation [83,84].

Platelet-Derived Growth Factors (PDGFs)

PDGF is a potent mitogen and chemotactic factor for cells of mesenchymal origin, including periodontal ligament (PDL) cells and osteoblasts [85]. PDGF can also regulate the expression of vascular endothelial growth factor (VEGF) to promote angiogenesis and is reported as an essential hormone in the healing process of soft tissue and bone [86]. PDGF exists as a dimer form (-AA, -AB, -BB, -CC, and -DD) and signals through binding to tyrosine kinase receptors, termed PDGF receptors alpha and beta [87], with PDGF-BB the most widely used isoform of PDGF based on its capability to bind to all known PDGF

receptor isotypes [86].

PDGF plays an indirect role in osteogenesis by recruiting and expanding the osteogenic cell populations, and subsequent differentiation of those cells is achieved by BMPs [88,89]. *In vivo* investigations also indicate that applying PDGF to denuded tooth root surfaces increase proliferation of PDL cells, osteoblasts, and perivascular cells, and accelerate alveolar bone regeneration [90-92]. A multicenter clinical trial validated PDGF-BB is capable of promoting periodontal defect regeneration [93]. Furthermore, a significant amount of *in vivo* bone regeneration was also noted in a 'pure' orthopaedic environment such as the calvarial or femoral critical-sized osteomtomy using a combination of calcium phosphate graft and PDGF [94,95]. Combination of PDGF and insulin-like growth factor-1 (IGF-1) had shown to stimulate bone regeneration around the press-fit titanium implants [96,97], however, to date, there is no investigation using PDGF alone to accelerate the implant osseointegration.

On the other hand, the possible inhibitory effects on osteogenesis have also been documented. Kono and colleague reported that PDGF treatment negatively regulates osteogenic differentiation [98], and Tokunaga et al demonstrated that specifically the PDGF

receptor beta had a determinable effect on mesenchymal cell differentiation [99]. Therefore, the bidirectional effect on osteogenesis is associated with the expression profile of PDGF, with pulse PDGF application stimulating osteogenesis while continuous PDGF exposure elicites an inhibitory effect [100].

Other Growth Factors and Combinations

Besides BMP and PDGF, there are still several growth factors being investigated for accelerating osteogenesis, such as transforming growth factor-beta (TGF-β), insulin-like growth factor (IGF), and fibroblast growth factor (FGF) [101,102]. TGF-β1 has been proposed as an osteoinductive factor based on its ability to promote proliferation of osteoblasts [103]. However, studies also demonstrate that TGF-β1 enhances chondrogenesis rather than osteogenesis in MSCs [104,105]. IGF-1 and IGF-2 regulate the bone formation process through increasing type I collagen synthesis, decreasing collagen degradation, modestly enhancing mitogenesis, and stabilizing β-catenin, a key regulator in Wnt pathway of osteogenic differentiation [106]. FGF-2 promotes mitogenesis and reduces apoptosis of osteoprogenitor cells, which increases the population of functional osteoblasts, but induces apoptosis in more differentiated osteoblasts, thus limiting the early increase of mature cells in the osteoblast pool [68]. A recent clinical investigation

demonstrated that FGF-2 significantly increased the alveolar bone height after 36 weeks in patients with periodontitis suggesting that FGF-2 could be a potential stimulator for bone regeneration [107].

The process of osteogenesis is regulated through several growth factors, and cross-talk most likely exists among them [68,108]. Thus, combination of growth factors is a viable approach to amplify osteogenesis. The first approach was proposed by Lynch and colleagues based on the synergistic effects on wound healing using a combination of PDGF-BB and IGF-1 [109]. This combination exhibited greater alveolar bone and cementum regeneration than single growth factor application [91,110], and promoted dental implant osseointegration in later investigations [96,97,111]. The combination of angiogenic (ie., VEGF) and osteogenic growth factors (ie., BMP) promoted bone regeneration [112,113], and dual delivery of BMP/TGF-β or BMP/FGF also enhanced osseointegration *in vivo* [114,115]. However, application should be controlled by sequential release profile of the growth factors in order to maximize the beneficial effects of combinatorial delivery[21].

1.3.3 Growth Factor Delivery Modes

Recombinant Proteins

According to previous investigations, the half-life of the polypeptide growth factors was about 3-5 hours, and more than 96% was cleared within 96 hours when using *in vivo* local delivery [116]. This highly transient nature of recombinant protein usually limits the effects *in vivo* [69]. The high initial dose of growth factors could be toxic, and repeated dosing is usually unsatisfactory for localized bone regeneration [117,118]. Thus, using a biocompatible delivery vehicle to control the release kinetics of growth factors has become a pivotal issue to achieve favorable therapeutic results [119]. For this purpose, an optimal delivery system often considers biodegradable natural materials, such as collagen and chitosan [120,121], or a synthetic polymer with a controllable degradation profile, such as polylatic acid, and poly-D,L-lactide-co-glycolide (PLGA) [72,122,123].

Gene Delivery

Gene therapy is an alternative method for growth factor delivery whereby transfer or transfection of the gene sequence, cells are then capable of producing the biologically active protein *in situ* without the concerns of exogenous protein degradation [69]. DNA is a stable molecule with a long shelf life and is considerably less expensive in manufacturing process. Thus, it may be more effective for achieving favorable results than the use of recombinant proteins [124]. The critical issues in gene therapy application are ensuring entry

of gene sequences to the cells, avoiding lysosmal degradation, and transcription of the gene[118].

Gene delivery is usually accomplished through the use of nonviral or viral vectors [69]. Nonviral-based gene therapy makes use of plasmid DNA or DNA polymer complexes to permit gene transfer and allow specific cell targeting using a tissue-specific promoter. Its main drawback is the low transduction rate (<10%) [125]. Viral-based gene delivery (eg., retrovirus, adenovirus) yields high transduction efficiency (>50%) to the cells. However, concerns include the potential for mutagenesis, carcinogenesis, or immunogenicity of the viral proteins [124,125].

Adenovirus (Ad) has a highly evolved mechanism for delivery of DNA to cells and permits effective short-term expression of growth factors [126,127]. Ads infect cells by receptor-mediated binding, internalization, endosomal escape, nuclear translocation, and finally, expression of delivered genes [128]. The viral DNA rarely incorporates into the human genome and does not induce any apparent phenotypic changes in infected cells [129]. The capability of carrier gene delivery to somatic cells and a prolonged activation of subsequent signaling pathways has also been documented by our group [130,131].

Some extensive investigations using Ad gene transfer reveal an early dose-dependent, neutrophil-predominant infiltrate and a delayed lymphocyte-predominant infiltrate, which results in the generation of humoral immunity and diminishes the efficiency of gene transfer [132,133]. Thus, the novel approach is to delete the E1 (the transforming region) and E3 (the immune modulatory region) gene regions, which not only permits insertion of growth factor genes, but also reduces the problem of Ad replication, oncogenic transformation, and possible immune response [134]. Systemic dissemination is another critical issue to be considered. Ad particles can be detected in liver, spleen, lung, and kidney within a few hours in mice, and death of Kupffer cells can be noted shortly after systemic administration of Ad [135,136]. Although most of vectors are digested by local phagocytes, fetal dissemination and transgene expression can still be noted in some of the localized Ad delivery studies [137,138].

Coating on the Implant Surface

The implant surface can be rendered osteoinductive by introducing growth factors, such as bone morphogenetic protein (BMP). Current technology involves incorporation or adsorption of the BMP into a three-dimensional crystal latticework of the calcium

phosphate layer, from which BMP can be released simultaneously as the layer undergoes degradation [139]. Significant promotion of *in vivo* osteogenesis and osseointegration is evident based on previous investigations [139-141], however, transient inflammatory responses induce bone-resorptive responses due to an initially high concentration of BMP [122], and foreign-body reactions due to the degradation of the coating [140] have also been reported from previous investigations.

1.4 Statement of Purpose and Dissertation Overview

Osseointegration involves both osteogenesis events and titanium-tissue interactions. Functional restoration may be more clinically relevant than validation from the bone architecture. However, most investigations of biomolecule-enhanced peri-implant tissue regeneration have focused solely on radiographic and histologic evaluations, yet correlations between structural and biomechanical measurements is still unclear. Although several biomolecule applications, such as platelet-derived growth factor (PDGF), have successfully enhanced bone and periodontal tissue regeneration, the effects of PDGF on peri-implant osseous wound repair have not been clearly elucidated.

Thus, the major objectives of this dissertation include

(1) To establish a functional parameter of osseointegration bridging the discrepancy between biomechanical and structural measurements.

(2) To investigate the promotive effects of PDGF during peri-implant osseous wound repair via different delivery strategies (i.e., human recombinant protein versus adenovirus-encoding gene delivery).

(3) Evaluate adenovirus-mediated gene delivery for accelerating osseointegration, and to determine the *in vivo* safety profile of this strategy.

There are three specific aims in this dissertation,

1. To Develop A Morphometry-Based Biomechanical Model to Evaluate the Dynamics of Oral Implant Osseointegration

Hypothesis: Functional dynamics of osseointegration can be predicted from the structural parameters

In this specific aim we utilized micro-computed tomography (micro-CT) images to establish the finite element (FE) model and we generated functional apparent moduli to represent the functional capability of the peri-implant tissues. To eliminate any scattering effects of titanium under micro-CT scanning, we removed the implant prior to imaging, and any possible tissue damage was evaluated using FE analyses. Both functional bone apparent modulus (FBAM) and functional composite tissue apparent modulus (FCAM) were generated through simulation of the functional scheme on the oral implant, and then these values were correlated with micro-CT parameters. We then investigated the best-match between the interfacial biomechanics and functional/micro-CT parameters within a range of the peri-implant layer to clarify the functional contribution of the peri-implant tissue. Our results demonstrated that the functional apparent moduli better

correlated with the micro-CT parameters. Bone mineral content (BMC) was the most sensitive micro-CT parameter contributing to the functional resistance. FCAM was functionally relevant to a pre-exisiting peri-implant defect, whereas FBAM was more reliable when a pre-existing defect was not presented. We conclude that FBAM and FCAM are capable to represent the peri-implant osseous wound repair as well as predict of the biomechanics of osseointegration. All of the above validations are stated in **Chapter 2**.

2. To Functionally Assess the Effects of Platelet-Derived Growth Factor (PDGF) Gene Delivery to Peri-Implant Tissue

Hypothesis: PDGF application is favorable for peri-implant tissue repair

PDGF has been known to promote mitogenesis and our previous investigations demonstrate significant periodontal osteogenesis and cementogenesis *in vivo* using PDGF [127]. However, the expression profile of PDGF may influence the result [100]. In **Chapter 3**, we evaluate the effects of PDGF on mitogenesis and osteogenic differentiation *in vitro* via recombinant protein (rhPDGF-BB) and adenovirus-mediated gene delivery (AdPDGF-B). A preclinical animal study was also conducted for advanced *in vivo* validation. Using delivery of rhPDGF-BB or AdPDGF-B to the peri-implant

circumferential bony defect, the extent of osseous wound repair was evaluated two-dimensionally, three-dimensionally, biomechanically, and functionally. Our results revealed that both delivery strategies promoted mitogenesis but, AdPDGF-B may prolong down-regulation of the osteogenic markers *in vitro*. The *in vivo* validations demonstrated that AdPDGF-B (especially the higher dose group) and rhPDGF-BB significantly promoted osteogenesis, defect fill, bone maturation, BIC, and FCAM by the early time point. We conclude that both rhPDGF-BB and AdPDGF-B accelerate peri-implant osseous wound repair and promote functional osseointegration.

3. To Evaluate the Safety Profile of Adenovirus-Mediated Gene Therapy

Hypothesis: AdPDGF-B delivery is safe for clinical dental use

Adenovirus has been regarded as an efficient vector to delivery genomic sequences. Based on the conclusion of specific aim 2, whereby AdPDGF-B significantly promoted osseous wound repair, we investigate the preclinical safety profile of local adenoviral vector delivery in **Chapter 4**. A maxillary peri-implant osseous defect and a comparable mandibular osteotomy was created in the Sprague-Dawley rat, and adenovirus vectors were applied to fill the defect area. The vector distribution and vector-related pathologies were evaluated locally and systemically. From our results, neither significant alteration of

systemic parameters nor distant spreading of vector was noted, and the expression of vectors within the delivery site was dramatically eliminated within 1 month. Thus, we conclude that local delivery of the adenoviral vectors to the jaw bone area reveal an acceptable preclinical safety profile.

1.5 Tables

Table 1.1 Correlations between biomechanical testing and peri-implant structures (primary stability)

Testing method	Model	Structure Assessment	Structural Parameters	Correlation	Reference
PO	Canine	Histology	CBT	r=0.44 *	[37]
IT	Human cadaver	CT (3D)	BMD	r=0.690 *	[13]
RFA	Human cadaver	CT (3D)	BMD	r=0.557 *	[13]
IT	Human cadaver	Micro-CT (3D)	Tb.Th Tb.N Tb.Sp	r=0.825 * r=0.718 * r=-0.795 *	[39]
RFA	Human cadaver	Micro-CT (3D)	Tb.Th Tb.N Tb.Sp	N.S. in any of parameter	[39]
IT	Human cadaver	CT (3D)	BMD	r^2=0.81 *	[38]
IT	Human	CT (3D)	BMD	r=0.10-0.83 *	[142]
RFA	Human	CT (3D)	BMD	r=0.34-0.91 *	[142]
IT	Human cadaver	CT (3D)	BMD	r=0.86 *	[143]
IT	Human	CT (3D)	BMD (ID<4 mm) BMD (ID>4 mm)	r=0.33-0.59 * r=0.05-0.29	[144]
RT	Human cadaver	Calipers	CBT TBT	p<0.05 * N.S.	[36]

* $p<0.05$

Abbreviations: IT: insertional torque; PO: pull-out; PS: push-out; RFA: resonance frequency analysis; CT: computed tomography; CBT: cortical bone thickness; BIC: bone-implant contact; BVD: bone-volume density; BMD: bone mineral density; BV/TV: bone volume/total volume; ID: implant diameter; TBT: total bone thickness; Tb.Th: trabecular thickness; Tb.N: trabecular number; Tb.Sp: trabecular separation; Conn.D: connectivity density; N.S.: no significant difference ($p>0.05$)

Table 1.2 Correlations between biomechanical testing and peri-implant structures (secondary stability)

Testing method	Model	Structure Assessment	Structural Parameters	Correlation	Reference
IT	Human	CT (2D)	CBT	r=0.320*	[41]
PO	Canine	Histology	CBT	N.S.	[37]
RFA	Human	Histology	BIC	P=0.016 *	[44]
RFA	Canine	Histology	BIC BVD	r=0.128, p=0.264 r=0.206, p=0.072	[45]
Periotest	Canine	Radiography	BIC	r=0.38 *	[42]
Periotest	Canine	Histology & radiography	BIC (His) BIC (Rad) BVD (His)	r^2=0.72 * r^2=0.88 * r^2=0.80 *	[14]
RFA	Porcine	Histology	BIC	r=0.221 *	[145]
RT	Rodent	Histology	BIC TBT	r=0.78-0.84 * r=0.68-0.76 *	[146]
PO	Rodent	Histology	TBT	r=0.87 *	[146]
PO	Rodent	Micro-CT (3D)	BIC BV/TV Tb.Th Tb.N Conn.D	r^2=0.52 (FL)* 0.24 (IS)* r^2=0.72 (FL)* 0.43 (IS)* r^2=0.60 (FL)* 0.31 (IS)* r^2=0.47 (FL)* 0.32 (IS)* r^2=0.37 (FL)* 0.28 (IS)*	[46]

* $p<0.05$ ** list the highest correlation coefficient in each parameter

Abbreviations: IT: insertional torque; PO: pull-out; PS: push-out; RFA: resonance frequency analysis; CT: computed tomography; CBT: cortical bone thickness; BIC: bone-implant contact; BV: bone volume; BVD: bone-volume density; BMC: bone mineral content; BMD: bone mineral density; BV/TV: bone volume/total volume; FBAM: functional bone apparent modulus; FCAM: functional composite tissue apparent modulus; ID: implant diameter; FL: failure load; IS: interfacial stiffness; OS: implant placing in osteotomy hole with osseous defect situation (0.6x1 mm circumferential); OA: implant placing in osteotomy-alone without any surrounding defect situation; TBT: total bone thickness; Tb.Th: trabecular thickness; Tb.N: trabecular number; Tb.Sp: trabecular separation; Conn.D: connectivity density; N.S.: no significant difference ($p>0.05$)

1.6 Figures

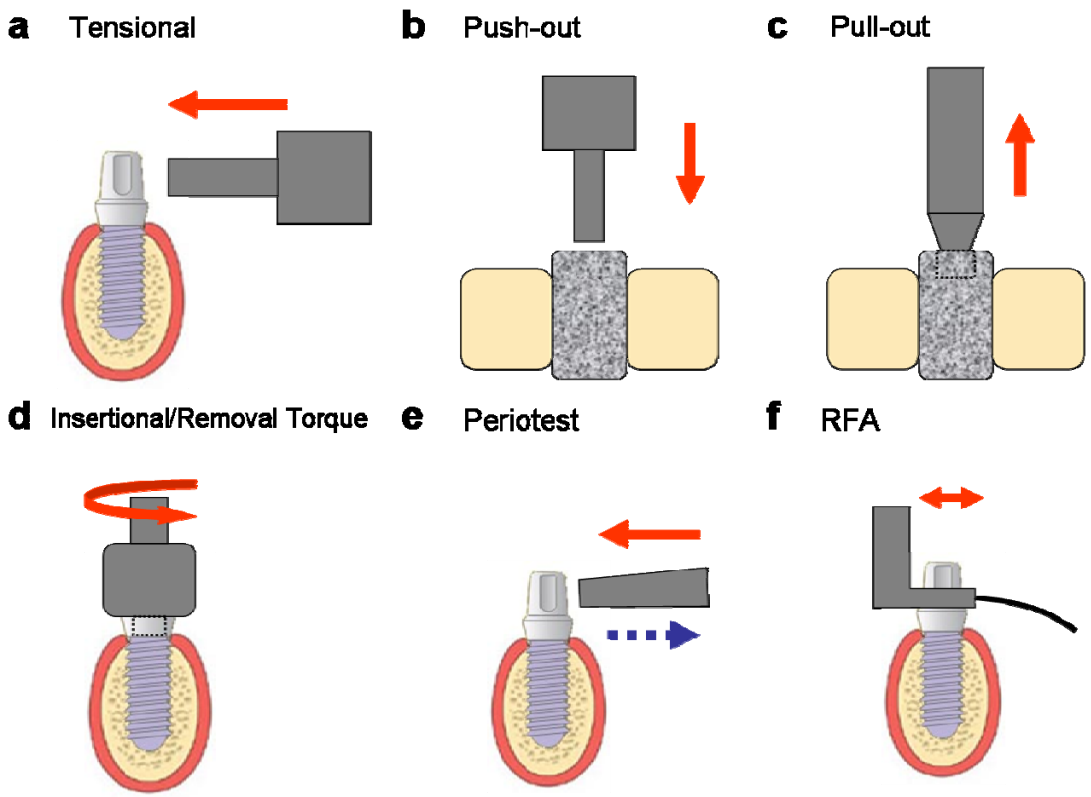

Figure 1.1 Biomechanical assessments for oral implant osseointegration (**a**) tensional test, (**b**) push-out test, (**c**) pull-out test, (**d**) insertional/removal torque test, (**e**) Periotest, and (e) resonance frequency analysis (RFA).

1.7 References

1. Franchi, M. et al. Biological fixation of endosseous implants. *Micron* **36**, 665-71 (2005).
2. Joos, U., Wiesmann, H.P., Szuwart, T. & Meyer, U. Mineralization at the interface of implants. *Int J Oral Maxillofac Surg* **35**, 783-90 (2006).
3. Berglundh, T., Abrahamsson, I., Lang, N.P. & Lindhe, J. De novo alveolar bone formation adjacent to endosseous implants. *Clin Oral Implants Res* **14**, 251-62 (2003).
4. Huiskes, R., Van Driel, W.D., Prendergast, P.J. & Soballe, K. A biomechanical regulatory model for periprosthetic fibrous-tissue differentiation. *J Mater Sci Mater Med* **8**, 785-8 (1997).
5. Colnot, C. et al. Molecular analysis of healing at a bone-implant interface. *J Dent Res* **86**, 862-7 (2007).
6. Futami, T. et al. Tissue response to titanium implants in the rat maxilla: ultrastructural and histochemical observations of the bone-titanium interface. *J Periodontol* **71**, 287-98 (2000).
7. Eriksson, R.A., Albrektsson, T. & Magnusson, B. Assessment of bone viability after heat trauma. A histological, histochemical and vital microscopic study in the rabbit. *Scand J Plast Reconstr Surg* **18**, 261-8 (1984).
8. Park, J.Y. & Davies, J.E. Red blood cell and platelet interactions with titanium implant surfaces. *Clin Oral Implants Res* **11**, 530-9 (2000).
9. Kasemo, B. & Gold, J. Implant surfaces and interface processes. *Adv Dent Res* **13**, 8-20 (1999).
10. Meyer, U. et al. Ultrastructural characterization of the implant/bone interface of immediately loaded dental implants. *Biomaterials* **25**, 1959-67 (2004).
11. Marco, F., Milena, F., Gianluca, G. & Vittoria, O. Peri-implant osteogenesis in health and osteoporosis. *Micron* **36**, 630-44 (2005).
12. Ferguson, S.J. et al. Biomechanical evaluation of the interfacial strength of a chemically modified sandblasted and acid-etched titanium surface. *J Biomed Mater Res A* **78**, 291-7 (2006).
13. Turkyilmaz, I., Sennerby, L., McGlumphy, E.A. & Tozum, T.F. Biomechanical Aspects of Primary Implant Stability: A Human Cadaver Study. *Clin Implant Dent Relat Res* (2008).
14. Ramp, L.C. & Jeffcoat, R.L. Dynamic behavior of implants as a measure of

osseointegration. *Int J Oral Maxillofac Implants* **16**, 637-45 (2001).
15. Hoffler, C.E. et al. Heterogeneity of bone lamellar-level elastic moduli. *Bone* **26**, 603-9 (2000).
16. Johansson, C.B., Han, C.H., Wennerberg, A. & Albrektsson, T. A quantitative comparison of machined commercially pure titanium and titanium-aluminum-vanadium implants in rabbit bone. *Int J Oral Maxillofac Implants* **13**, 315-21 (1998).
17. Berzins, A., Shah, B., Weinans, H. & Sumner, D.R. Nondestructive measurements of implant-bone interface shear modulus and effects of implant geometry in pull-out tests. *J Biomed Mater Res* **34**, 337-40 (1997).
18. Aparicio, C., Lang, N.P. & Rangert, B. Validity and clinical significance of biomechanical testing of implant/bone interface. *Clin Oral Implants Res* **17 Suppl 2**, 2-7 (2006).
19. Kitsugi, T. et al. Bone bonding behavior of titanium and its alloys when coated with titanium oxide (TiO2) and titanium silicate (Ti5Si3). *J Biomed Mater Res* **32**, 149-56 (1996).
20. Branemark, R., Ohrnell, L.O., Skalak, R., Carlsson, L. & Branemark, P.I. Biomechanical characterization of osseointegration: an experimental in vivo investigation in the beagle dog. *J Orthop Res* **16**, 61-9 (1998).
21. Kempen, D.H. et al. Effect of local sequential VEGF and BMP-2 delivery on ectopic and orthotopic bone regeneration. *Biomaterials* (2009).
22. Brunski, J.B., Puleo, D.A. & Nanci, A. Biomaterials and biomechanics of oral and maxillofacial implants: current status and future developments. *Int J Oral Maxillofac Implants* **15**, 15-46 (2000).
23. Lutolf, M.P. et al. Repair of bone defects using synthetic mimetics of collagenous extracellular matrices. *Nat Biotechnol* **21**, 513-8 (2003).
24. Yeo, I.S., Han, J.S. & Yang, J.H. Biomechanical and histomorphometric study of dental implants with different surface characteristics. *J Biomed Mater Res B Appl Biomater* **87**, 303-11 (2008).
25. Meredith, N., Shagaldi, F., Alleyne, D., Sennerby, L. & Cawley, P. The application of resonance frequency measurements to study the stability of titanium implants during healing in the rabbit tibia. *Clin Oral Implants Res* **8**, 234-43 (1997).
26. Friberg, B. et al. Evaluation of bone density using cutting resistance measurements and microradiography: an in vitro study in pig ribs. *Clin Oral Implants Res* **6**, 164-71 (1995).
27. Ueda, M., Matsuki, M., Jacobsson, M. & Tjellstrom, A. Relationship between

insertion torque and removal torque analyzed in fresh temporal bone. *Int J Oral Maxillofac Implants* **6**, 442-7 (1991).

28. O'Sullivan, D., Sennerby, L. & Meredith, N. Measurements comparing the initial stability of five designs of dental implants: a human cadaver study. *Clin Implant Dent Relat Res* **2**, 85-92 (2000).
29. Molly, L. Bone density and primary stability in implant therapy. *Clin Oral Implants Res* **17 Suppl 2**, 124-35 (2006).
30. Schulte, W. & Lukas, D. Periotest to monitor osseointegration and to check the occlusion in oral implantology. *J Oral Implantol* **19**, 23-32 (1993).
31. Olive, J. & Aparicio, C. Periotest method as a measure of osseointegrated oral implant stability. *Int J Oral Maxillofac Implants* **5**, 390-400 (1990).
32. Schulte, W. & Lukas, D. The Periotest method. *Int Dent J* **42**, 433-40 (1992).
33. Atsumi, M., Park, S.H. & Wang, H.L. Methods used to assess implant stability: current status. *Int J Oral Maxillofac Implants* **22**, 743-54 (2007).
34. Friberg, B., Sennerby, L., Meredith, N. & Lekholm, U. A comparison between cutting torque and resonance frequency measurements of maxillary implants. A 20-month clinical study. *Int J Oral Maxillofac Surg* **28**, 297-303 (1999).
35. Bischof, M., Nedir, R., Szmukler-Moncler, S., Bernard, J.P. & Samson, J. Implant stability measurement of delayed and immediately loaded implants during healing. *Clin Oral Implants Res* **15**, 529-39 (2004).
36. Niimi, A., Ozeki, K., Ueda, M. & Nakayama, B. A comparative study of removal torque of endosseous implants in the fibula, iliac crest and scapula of cadavers: preliminary report. *Clin Oral Implants Res* **8**, 286-9 (1997).
37. Salmoria, K.K. et al. Insertional torque and axial pull-out strength of mini-implants in mandibles of dogs. *Am J Orthod Dentofacial Orthop* **133**, 790 e15-22 (2008).
38. Homolka, P. et al. Bone mineral density measurement with dental quantitative CT prior to dental implant placement in cadaver mandibles: pilot study. *Radiology* **224**, 247-52 (2002).
39. Akca, K., Chang, T.L., Tekdemir, I. & Fanuscu, M.I. Biomechanical aspects of initial intraosseous stability and implant design: a quantitative micro-morphometric analysis. *Clin Oral Implants Res* **17**, 465-72 (2006).
40. Wennerberg, A., Albrektsson, T. & Lausmaa, J. Torque and histomorphometric evaluation of c.p. titanium screws blasted with 25- and 75-microns-sized particles of Al2O3. *J Biomed Mater Res* **30**, 251-60 (1996).
41. Motoyoshi, M., Yoshida, T., Ono, A. & Shimizu, N. Effect of cortical bone

thickness and implant placement torque on stability of orthodontic mini-implants. *Int J Oral Maxillofac Implants* **22**, 779-84 (2007).

42. Sykaras, N., Iacopino, A.M., Triplett, R.G. & Marker, V.A. Effect of recombinant human bone morphogenetic protein-2 on the osseointegration of dental implants: a biomechanics study. *Clin Oral Investig* **8**, 196-205 (2004).
43. Itoh, K., Suzuki, S. & Kuroda, T. Effects of local administration of insulin-like growth factor-I on mandibular condylar growth in rats. *J Med Dent Sci* **50**, 79-85 (2003).
44. Scarano, A., Degidi, M., Iezzi, G., Petrone, G. & Piattelli, A. Correlation between implant stability quotient and bone-implant contact: a retrospective histological and histomorphometrical study of seven titanium implants retrieved from humans. *Clin Implant Dent Relat Res* **8**, 218-22 (2006).
45. Schliephake, H. et al. Effect of RGD peptide coating of titanium implants on periimplant bone formation in the alveolar crest. An experimental pilot study in dogs. *Clin Oral Implants Res* **13**, 312-9 (2002).
46. Gabet, Y. et al. Parathyroid hormone 1-34 enhances titanium implant anchorage in low-density trabecular bone: a correlative micro-computed tomographic and biomechanical analysis. *Bone* **39**, 276-82 (2006).
47. Le Guehennec, L., Soueidan, A., Layrolle, P. & Amouriq, Y. Surface treatments of titanium dental implants for rapid osseointegration. *Dent Mater* **23**, 844-54 (2007).
48. Buser, D. et al. Influence of surface characteristics on bone integration of titanium implants. A histomorphometric study in miniature pigs. *J Biomed Mater Res* **25**, 889-902 (1991).
49. Kilpadi, D.V. & Lemons, J.E. Surface energy characterization of unalloyed titanium implants. *J Biomed Mater Res* **28**, 1419-25 (1994).
50. Kim, T.N. et al. In vitro fibroblast response to ultra fine grained titanium produced by a severe plastic deformation process. *J Mater Sci Mater Med* **19**, 553-7 (2008).
51. Bowers, K.T., Keller, J.C., Randolph, B.A., Wick, D.G. & Michaels, C.M. Optimization of surface micromorphology for enhanced osteoblast responses in vitro. *Int J Oral Maxillofac Implants* **7**, 302-10 (1992).
52. Anselme, K. & Bigerelle, M. Topography effects of pure titanium substrates on human osteoblast long-term adhesion. *Acta Biomater* **1**, 211-22 (2005).
53. Kieswetter, K., Schwartz, Z., Dean, D.D. & Boyan, B.D. The role of implant surface characteristics in the healing of bone. *Crit Rev Oral Biol Med* **7**, 329-45 (1996).

54. Andreykiv, A., van Keulen, F. & Prendergast, P.J. Computational mechanobiology to study the effect of surface geometry on peri-implant tissue differentiation. *J Biomech Eng* **130**, 051015 (2008).
55. Hansson, S. & Norton, M. The relation between surface roughness and interfacial shear strength for bone-anchored implants. A mathematical model. *J Biomech* **32**, 829-36 (1999).
56. Schwartz, Z. et al. Implant surface characteristics modulate differentiation behavior of cells in the osteoblastic lineage. *Adv Dent Res* **13**, 38-48 (1999).
57. Misra, R.D. et al. Cellular response of preosteoblasts to nanograined/ultrafine-grained structures. *Acta Biomater* (2009).
58. Brett, P.M. et al. Roughness response genes in osteoblasts. *Bone* **35**, 124-33 (2004).
59. Puckett, S., Pareta, R. & Webster, T.J. Nano rough micron patterned titanium for directing osteoblast morphology and adhesion. *Int J Nanomedicine* **3**, 229-41 (2008).
60. Knabe, C., Howlett, C.R., Klar, F. & Zreiqat, H. The effect of different titanium and hydroxyapatite-coated dental implant surfaces on phenotypic expression of human bone-derived cells. *J Biomed Mater Res A* **71**, 98-107 (2004).
61. Geurs, N.C., Jeffcoat, R.L., McGlumphy, E.A., Reddy, M.S. & Jeffcoat, M.K. Influence of implant geometry and surface characteristics on progressive osseointegration. *Int J Oral Maxillofac Implants* **17**, 811-5 (2002).
62. Chang, Y.L., Lew, D., Park, J.B. & Keller, J.C. Biomechanical and morphometric analysis of hydroxyapatite-coated implants with varying crystallinity. *J Oral Maxillofac Surg* **57**, 1096-108; discussion 1108-9 (1999).
63. Lee, J.J., Rouhfar, L. & Beirne, O.R. Survival of hydroxyapatite-coated implants: a meta-analytic review. *J Oral Maxillofac Surg* **58**, 1372-9; discussion 1379-80 (2000).
64. Shakesheff, K., Cannizzaro, S. & Langer, R. Creating biomimetic micro-environments with synthetic polymer-peptide hybrid molecules. *J Biomater Sci Polym Ed* **9**, 507-18 (1998).
65. Alsberg, E., Anderson, K.W., Albeiruti, A., Franceschi, R.T. & Mooney, D.J. Cell-interactive alginate hydrogels for bone tissue engineering. *J Dent Res* **80**, 2025-9 (2001).
66. Tosatti, S. et al. RGD-containing peptide GCRGYGRGDSPG reduces enhancement of osteoblast differentiation by poly(L-lysine)-graft-poly(ethylene glycol)-coated titanium surfaces. *J Biomed Mater Res A* **68**, 458-72 (2004).

67. Garcia, A.J. & Reyes, C.D. Bio-adhesive surfaces to promote osteoblast differentiation and bone formation. *J Dent Res* **84**, 407-13 (2005).
68. Marie, P.J. Fibroblast growth factor signaling controlling osteoblast differentiation. *Gene* **316**, 23-32 (2003).
69. Ramseier, C.A., Abramson, Z.R., Jin, Q. & Giannobile, W.V. Gene therapeutics for periodontal regenerative medicine. *Dent Clin North Am* **50**, 245-63, ix (2006).
70. Taba, M., Jr., Jin, Q., Sugai, J.V. & Giannobile, W.V. Current concepts in periodontal bioengineering. *Orthod Craniofac Res* **8**, 292-302 (2005).
71. Chen, D., Zhao, M. & Mundy, G.R. Bone morphogenetic proteins. *Growth Factors* **22**, 233-41 (2004).
72. Chang, P.C. et al. Bone tissue engineering with novel rhBMP2-PLLA composite scaffolds. *J Biomed Mater Res A* **81**, 771-80 (2007).
73. Hak, D.J. et al. Recombinant human BMP-7 effectively prevents non-union in both young and old rats. *J Orthop Res* **24**, 11-20 (2006).
74. Barboza, E.P. et al. Effect of recombinant human bone morphogenetic protein-2 in an absorbable collagen sponge with space-providing biomaterials on the augmentation of chronic alveolar ridge defects. *J Periodontol* **75**, 702-8 (2004).
75. Brandao, A.C. et al. Histomorphometric analysis of rat alveolar wound healing with hydroxyapatite alone or associated to BMPs. *Braz Dent J* **13**, 147-54 (2002).
76. Cochran, D.L., Schenk, R., Buser, D., Wozney, J.M. & Jones, A.A. Recombinant human bone morphogenetic protein-2 stimulation of bone formation around endosseous dental implants. *J Periodontol* **70**, 139-50 (1999).
77. Nevins, M. et al. Bone formation in the goat maxillary sinus induced by absorbable collagen sponge implants impregnated with recombinant human bone morphogenetic protein-2. *Int J Periodontics Restorative Dent* **16**, 8-19 (1996).
78. Jovanovic, S.A. et al. Bone reconstruction following implantation of rhBMP-2 and guided bone regeneration in canine alveolar ridge defects. *Clin Oral Implants Res* **18**, 224-30 (2007).
79. Jones, A.A., Buser, D., Schenk, R., Wozney, J. & Cochran, D.L. The effect of rhBMP-2 around endosseous implants with and without membranes in the canine model. *J Periodontol* **77**, 1184-93 (2006).
80. Matin, K., Nakamura, H., Irie, K., Ozawa, H. & Ejiri, S. Impact of recombinant human bone morphogenetic protein-2 on residual ridge resorption after tooth extraction: an experimental study in the rat. *Int J Oral Maxillofac Implants* **16**, 400-11 (2001).
81. Bianchi, J. et al. Measuring the efficacy of rhBMP-2 to regenerate bone: a

radiographic study using a commercially available software program. *Int J Periodontics Restorative Dent* **24**, 579-87 (2004).

82. Howell, T.H. et al. A feasibility study evaluating rhBMP-2/absorbable collagen sponge device for local alveolar ridge preservation or augmentation. *Int J Periodontics Restorative Dent* **17**, 124-39 (1997).
83. Boyne, P.J. et al. De novo bone induction by recombinant human bone morphogenetic protein-2 (rhBMP-2) in maxillary sinus floor augmentation. *J Oral Maxillofac Surg* **63**, 1693-707 (2005).
84. Jung, R.E. et al. Effect of rhBMP-2 on guided bone regeneration in humans. *Clin Oral Implants Res* **14**, 556-68 (2003).
85. Graves, D.T., Kang, Y.M. & Kose, K.N. Growth factors in periodontal regeneration. *Compend Suppl*, S672-7; quiz S714-7 (1994).
86. Hollinger, J.O., Hart, C.E., Hirsch, S.N., Lynch, S. & Friedlaender, G.E. Recombinant human platelet-derived growth factor: biology and clinical applications. *J Bone Joint Surg Am* **90 Suppl 1**, 48-54 (2008).
87. Seifert, R.A. et al. Two different subunits associate to create isoform-specific platelet-derived growth factor receptors. *J Biol Chem* **264**, 8771-8 (1989).
88. Chaudhary, L.R. & Hruska, K.A. The cell survival signal Akt is differentially activated by PDGF-BB, EGF, and FGF-2 in osteoblastic cells. *J Cell Biochem* **81**, 304-11 (2001).
89. Cho, T.J., Gerstenfeld, L.C. & Einhorn, T.A. Differential temporal expression of members of the transforming growth factor beta superfamily during murine fracture healing. *J Bone Miner Res* **17**, 513-20 (2002).
90. Wang, H.L. et al. The effect of platelet-derived growth factor on the cellular response of the periodontium: an autoradiographic study on dogs. *J Periodontol* **65**, 429-36 (1994).
91. Giannobile, W.V. et al. Comparative effects of platelet-derived growth factor-BB and insulin-like growth factor-I, individually and in combination, on periodontal regeneration in Macaca fascicularis. *J Periodontal Res* **31**, 301-12 (1996).
92. Park, J.B. et al. Periodontal regeneration in class III furcation defects of beagle dogs using guided tissue regenerative therapy with platelet-derived growth factor. *J Periodontol* **66**, 462-77 (1995).
93. Nevins, M. et al. Platelet-derived growth factor stimulates bone fill and rate of attachment level gain: results of a large multicenter randomized controlled trial. *J Periodontol* **76**, 2205-15 (2005).
94. Lee, Y.M. et al. The bone regenerative effect of platelet-derived growth factor-BB

delivered with a chitosan/tricalcium phosphate sponge carrier. *J Periodontol* **71**, 418-24 (2000).

95. Nash, T.J. et al. Effect of platelet-derived growth factor on tibial osteotomies in rabbits. *Bone* **15**, 203-8 (1994).
96. Becker, W. et al. A comparison of ePTFE membranes alone or in combination with platelet-derived growth factors and insulin-like growth factor-I or demineralized freeze-dried bone in promoting bone formation around immediate extraction socket implants. *J Periodontol* **63**, 929-40 (1992).
97. Lynch, S.E. et al. Effects of the platelet-derived growth factor/insulin-like growth factor-I combination on bone regeneration around titanium dental implants. Results of a pilot study in beagle dogs. *J Periodontol* **62**, 710-6 (1991).
98. Kono, S.J. et al. Erk pathways negatively regulate matrix mineralization. *Bone* **40**, 68-74 (2007).
99. Tokunaga, A. et al. PDGF receptor beta is a potent regulator of mesenchymal stromal cell function. *J Bone Miner Res* **23**, 1519-28 (2008).
100. Hsieh, S.C. & Graves, D.T. Pulse application of platelet-derived growth factor enhances formation of a mineralizing matrix while continuous application is inhibitory. *J Cell Biochem* **69**, 169-80 (1998).
101. Mukherjee, A. & Rotwein, P. Akt promotes BMP2-mediated osteoblast differentiation and bone development. *J Cell Sci* **122**, 716-26 (2009).
102. Andrades, J.A. et al. A recombinant human TGF-beta1 fusion protein with collagen-binding domain promotes migration, growth, and differentiation of bone marrow mesenchymal cells. *Exp Cell Res* **250**, 485-98 (1999).
103. Macdonald, K.K., Cheung, C.Y. & Anseth, K.S. Cellular delivery of TGFbeta1 promotes osteoinductive signalling for bone regeneration. *J Tissue Eng Regen Med* **1**, 314-7 (2007).
104. Ng, F. et al. PDGF, TGF-beta, and FGF signaling is important for differentiation and growth of mesenchymal stem cells (MSCs): transcriptional profiling can identify markers and signaling pathways important in differentiation of MSCs into adipogenic, chondrogenic, and osteogenic lineages. *Blood* **112**, 295-307 (2008).
105. Xu, Y., James, A.W. & Longaker, M.T. Transforming growth factor-beta1 stimulates chondrogenic differentiation of posterofrontal suture-derived mesenchymal cells in vitro. *Plast Reconstr Surg* **122**, 1649-59 (2008).
106. Giustina, A., Mazziotti, G. & Canalis, E. Growth hormone, insulin-like growth factors, and the skeleton. *Endocr Rev* **29**, 535-59 (2008).
107. Kitamura, M. et al. Periodontal tissue regeneration using fibroblast growth

factor-2: randomized controlled phase II clinical trial. *PLoS ONE* **3**, e2611 (2008).
108. Singhatanadgit, W., Salih, V. & Olsen, I. Up-regulation of bone morphogenetic protein receptor IB by growth factors enhances BMP-2-induced human bone cell functions. *J Cell Physiol* **209**, 912-22 (2006).
109. Lynch, S.E., Colvin, R.B. & Antoniades, H.N. Growth factors in wound healing. Single and synergistic effects on partial thickness porcine skin wounds. *J Clin Invest* **84**, 640-6 (1989).
110. Lynch, S.E. et al. A combination of platelet-derived and insulin-like growth factors enhances periodontal regeneration. *J Clin Periodontol* **16**, 545-8 (1989).
111. Stefani, C.M. et al. Platelet-derived growth factor/insulin-like growth factor-1 combination and bone regeneration around implants placed into extraction sockets: a histometric study in dogs. *Implant Dent* **9**, 126-31 (2000).
112. Huang, Y.C., Kaigler, D., Rice, K.G., Krebsbach, P.H. & Mooney, D.J. Combined angiogenic and osteogenic factor delivery enhances bone marrow stromal cell-driven bone regeneration. *J Bone Miner Res* **20**, 848-57 (2005).
113. Patel, Z.S. et al. Dual delivery of an angiogenic and an osteogenic growth factor for bone regeneration in a critical size defect model. *Bone* **43**, 931-40 (2008).
114. Lan, J., Wang, Z., Wang, Y., Wang, J. & Cheng, X. The effect of combination of recombinant human bone morphogenetic protein-2 and basic fibroblast growth factor or insulin-like growth factor-I on dental implant osseointegration by confocal laser scanning microscopy. *J Periodontol* **77**, 357-63 (2006).
115. Sumner, D.R., Turner, T.M., Urban, R.M., Virdi, A.S. & Inoue, N. Additive enhancement of implant fixation following combined treatment with rhTGF-beta2 and rhBMP-2 in a canine model. *J Bone Joint Surg Am* **88**, 806-17 (2006).
116. Lynch, S.E. et al. The effects of short-term application of a combination of platelet-derived and insulin-like growth factors on periodontal wound healing. *J Periodontol* **62**, 458-67 (1991).
117. Mason, J.M. et al. Expression of human bone morphogenic protein 7 in primary rabbit periosteal cells: potential utility in gene therapy for osteochondral repair. *Gene Ther* **5**, 1098-104 (1998).
118. Southwood, L.L., Frisbie, D.D., Kawcak, C.E. & McIlwraith, C.W. Delivery of growth factors using gene therapy to enhance bone healing. *Vet Surg* **33**, 565-78 (2004).
119. Chen, R.R. & Mooney, D.J. Polymeric growth factor delivery strategies for tissue engineering. *Pharm Res* **20**, 1103-12 (2003).
120. Park, Y.J. et al. Platelet derived growth factor releasing chitosan sponge for

periodontal bone regeneration. *Biomaterials* **21**, 153-9 (2000).

121. Sano, A. et al. Atelocollagen for protein and gene delivery. *Adv Drug Deliv Rev* **55**, 1651-77 (2003).
122. Ruhe, P.Q. et al. Controlled release of rhBMP-2 loaded poly(dl-lactic-co-glycolic acid)/calcium phosphate cement composites in vivo. *J Control Release* **106**, 162-71 (2005).
123. Jin, Q. et al. Nanofibrous scaffolds incorporating PDGF-BB microspheres induce chemokine expression and tissue neogenesis in vivo. *PLoS ONE* **3**, e1729 (2008).
124. Franceschi, R.T. Biological approaches to bone regeneration by gene therapy. *J Dent Res* **84**, 1093-103 (2005).
125. Partridge, K.A. & Oreffo, R.O. Gene delivery in bone tissue engineering: progress and prospects using viral and nonviral strategies. *Tissue Eng* **10**, 295-307 (2004).
126. Dunn, C.A. et al. BMP gene delivery for alveolar bone engineering at dental implant defects. *Mol Ther* **11**, 294-9 (2005).
127. Jin, Q., Anusaksathien, O., Webb, S.A., Printz, M.A. & Giannobile, W.V. Engineering of tooth-supporting structures by delivery of PDGF gene therapy vectors. *Mol Ther* **9**, 519-26 (2004).
128. Dinh, A.T., Theofanous, T. & Mitragotri, S. A model for intracellular trafficking of adenoviral vectors. *Biophys J* **89**, 1574-88 (2005).
129. Crombleholme, T.M. Adenoviral-mediated gene transfer in wound healing. *Wound Repair Regen* **8**, 460-72 (2000).
130. Chen, Q.P. & Giannobile, W.V. Adenoviral gene transfer of PDGF downregulates gas gene product PDGFalphaR and prolongs ERK and Akt/PKB activation. *Am J Physiol Cell Physiol* **282**, C538-44 (2002).
131. Lin, Z., Sugai, J.V., Jin, Q., Chandler, L.A. & Giannobile, W.V. Platelet-derived growth factor-B gene delivery sustains gingival fibroblast signal transduction. *J Periodontal Res* **43**, 440-9 (2008).
132. Schulick, A.H. et al. Established immunity precludes adenovirus-mediated gene transfer in rat carotid arteries. Potential for immunosuppression and vector engineering to overcome barriers of immunity. *J Clin Invest* **99**, 209-19 (1997).
133. Roessler, B.J., Allen, E.D., Wilson, J.M., Hartman, J.W. & Davidson, B.L. Adenoviral-mediated gene transfer to rabbit synovium in vivo. *J Clin Invest* **92**, 1085-92 (1993).
134. Kozarsky, K.F. & Wilson, J.M. Gene therapy: adenovirus vectors. *Curr Opin Genet Dev* **3**, 499-503 (1993).
135. Manickan, E. et al. Rapid Kupffer cell death after intravenous injection of

adenovirus vectors. *Mol Ther* **13**, 108-17 (2006).

136. Wang, Y. et al. Characterisation of systemic dissemination of nonreplicating adenoviral vectors from tumours in local gene delivery. *Br J Cancer* **92**, 1414-20 (2005).
137. Lenaerts, L., Verbeken, E., De Clercq, E. & Naesens, L. Mouse adenovirus type 1 infection in SCID mice: an experimental model for antiviral therapy of systemic adenovirus infections. *Antimicrob Agents Chemother* **49**, 4689-99 (2005).
138. Lohr, F., Huang, Q., Hu, K., Dewhirst, M.W. & Li, C.Y. Systemic vector leakage and transgene expression by intratumorally injected recombinant adenovirus vectors. *Clin Cancer Res* **7**, 3625-8 (2001).
139. Liu, Y., Huse, R.O., de Groot, K., Buser, D. & Hunziker, E.B. Delivery mode and efficacy of BMP-2 in association with implants. *J Dent Res* **86**, 84-9 (2007).
140. Liu, Y., de Groot, K. & Hunziker, E.B. BMP-2 liberated from biomimetic implant coatings induces and sustains direct ossification in an ectopic rat model. *Bone* **36**, 745-57 (2005).
141. Schmidmaier, G. et al. Bone morphogenetic protein-2 coating of titanium implants increases biomechanical strength and accelerates bone remodeling in fracture treatment: a biomechanical and histological study in rats. *Bone* **30**, 816-22 (2002).
142. Turkyilmaz, I., Tumer, C., Ozbek, E.N. & Tozum, T.F. Relations between the bone density values from computerized tomography, and implant stability parameters: a clinical study of 230 regular platform implants. *J Clin Periodontol* **34**, 716-22 (2007).
143. Beer, A., Gahleitner, A., Holm, A., Tschabitscher, M. & Homolka, P. Correlation of insertion torques with bone mineral density from dental quantitative CT in the mandible. *Clin Oral Implants Res* **14**, 616-20 (2003).
144. Turkyilmaz, I., Tozum, T.F., Tumer, C. & Ozbek, E.N. Assessment of correlation between computerized tomography values of the bone, and maximum torque and resonance frequency values at dental implant placement. *J Oral Rehabil* **33**, 881-8 (2006).
145. Ito, Y. et al. Relevance of resonance frequency analysis to evaluate dental implant stability: simulation and histomorphometrical animal experiments. *Clin Oral Implants Res* **19**, 9-14 (2008).
146. Branemark, R., Ohrnell, L.O., Nilsson, P. & Thomsen, P. Biomechanical characterization of osseointegration during healing: an experimental in vivo study in the rat. *Biomaterials* **18**, 969-78 (1997).

CHAPTER 2

FUNCTIONAL APPARENT MODULI FOR ASSESSING DENTAL IMPLANT OSSEOINTEGRATION

2.1 Abstract

Osseointegration is critical for the rehabilitation of dental implant patients. It remains a challenge to better understand biomechanical function during alveolar bone repair and osseointegration because of the limited availability of functional measures for assessment of implant function. The objective of this investigation was to establish a reproducible methodology for determining implant function by using micro-computed tomography (micro-CT) and finite element (FE) simulations in an *in vivo* rat animal model. Methodology validation of 3-D micro-CT, functional *bone* apparent modulus (FBAM) and *composite tissue* apparent modulus (FCAM) by FE optimization of maxillary osteotomy defects was performed. Strong correlations were found among bone mineral density (BMD), bone-implant contact (BIC), and FCAM in osteotomies alone or associated with large simulated extraction socket defects. Significant enhancement of FCAM indicated progressive functional osteogenesis during early osseointegration. Furthermore, the interfacial resistance at osteotomy defect sites was effectively predicted from bone mineral content (BMC) and FBAM within ~200 μm radial zone, while the contribution of extraction defects led to a highly-correlated zone of ~575 μm and 200 μm, for BMC and FCAM, respectively. In conclusion, the combination of micro-CT imaging

and functional simulation was capable of determining the functional dynamics of dental implant osseointegration *in vivo.*

2.2 Introduction

Dental implants are widely accepted for tooth replacement because they provide direct anchorage to the alveolar bone. The process of implant osseointegration has been extensively studied in several animal models, with most of the information being derived from radiographic and histologic analyses [1,2]. However, the functional dynamics of dentoalveolar tissue during healing remains unclear due to difficulty in three-dimensionally evaluating the topography of the implant-tissue interface by radiographic imaging [3] and the inability to link this data with current biomechanical tests. Over the past twenty years , finite element (FE) analysis has been used to predict and study the biomechanical aspects of dental implants [4-6]. However, evaluating the *in vivo* progress of osseointegration was still not feasible due to microscopic property assignments which increased the numerical complexity. Therefore, previous investigations on homogenizing the bone through FE optimizing under simulated loading situations reported significant agreement between 'effective stiffness' and experimental results [7-9]. Thus, functional homogenization of peri-implant tissue may be feasible for demonstrating the biomechanical dynamics of peri-implant tissue.

The aim of this study was to develop a model to determine implant tissue-supporting biomechanical properties during implant osseointegration. Given that implant stability depends primarily on the quality of bone-implant contact and the rigidity of peri-implant osteogenesis [10], we examined the interfacial stiffness of bone and implants via a push-out methodology and then three-dimensionally evaluating peri-implant tissue using micro-CT.

FE analyses were performed to validate micro-CT use, and functional parameters including functional bone apparent modulus (FBAM) and functional composite tissue apparent modulus (FCAM) were generated to evaluate peri-implant and interfacial osseous wound healing dynamics through functional homogenization. Our results demonstrated that micro-CT imaging was useful during early-stage osseointegration, and bone-implant interfacial properties could be predicted from the biomechanical and radiographic properties rendered from these methods.

2.3 Materials and Methods

2.3.1 Study materials

A total of 40 male Sprague-Dawley rats were utilized in this study, and cylindrical titanium implants with SLActive® surface treatment were the generous gifts from the Institut Straumann AG, Basel, Switerzland. A set of customized step-drills (Figure 2.1) were fabricated from Cutting Edge Technologies Inc. (Plymouth, MA, USA). A commercial radiographic phantom (Gammex Inc., Middleton WI, USA), with electron density-to-water of 1.09 and physical density of 1.12 g/cm^3 was utilized to simulate the alveolar bone structure during micro-CT scanning.

2.3.2 The Definition of parameters

To standardize the evaluations, a curve between 20% and 80% of the maximum removing load (MRL) was chosen and linear regression was utilized to calculate the interfacial stiffness (IS).

(1) Maximal removing load (MRL): The peak value of loading on the load-displacement curve during implant push-out, which represented the functional capability of whole implant supporting tissue.

(2) Interfacial stiffness (IS): The slope of linear region of load-displacement curve before complete implant push-out, which represents rigidity of interfacial tissues.

(3) Bone implant contact (BIC): the mineralized tissue directly contacting the implant surface.

(4) Bone volume fraction (BVF): the volume of mineralized tissue within the osseous wound divided by the volume of osseous wound.

(5) Tissue mineral density (TMD): the mineral content of the radiographically-defined mineralized tissue within the osseous wound divided by the volume of osseous wound.

(6) Bone mineral density (BMD): The mineral density within the radiographic-defined mineralized tissue in the osseous wound.

(7) Functional bone modulus (FBAM): The rigidity of bone toward the dental implant, which served as the indicator of the functionally available bone maturation.

(8) Functional composite tissue modulus (FCAM): The rigidity of composite tissues (including granulation tissue and bone) toward dental implant, which served as the indicator of the functional rigidity of the whole tissue.

(9) Mathematical bone modulus (MBM): The mean Young's modulus of bone toward the dental implant, which served as the general rigidity of bone.

(10) Mathematical composite tissue modulus (MCM): The mean Young's modulus of composite tissue (granulation tissue and bone), which served as the indicator of the general rigidity of the whole tissue.

2.3.3 The animal model

All animal surgical procedures followed the guidelines from the University Committee on Use and Care of Animals (UCUCA) at the University of Michigan. The rat dental implant osseous defect model [11] was utilized with modifications. Briefly, the animals were anesthesized by intraperitoneal injection of ketamine (87 mg/kg) and xyzaline (10 mg/kg), and analgesic administered by subcutaneous injection of buprenex (0.01-0.05 mg/kg). The maxillary first molars were extracted four weeks prior to implant installation. For implant placement, an 0.95mm diameter osteotomy was created from

oral cavity to maxillary sinus to facilitate implant (1mm diameter) installation for the osteotomy-alone (OA) group (Fig 2.2a). An 0.6x2 mm circumferential osseous defect (inferior region) was surgically created and filled with a 2.6% type I collagen matrix (Tissue Repair Company, San Diego, CA, USA) containing an adenoviral reporter gene (adenovirus-encoding luciferase) [12] which comprised the osteotomy+osseous defect (OS) group (Fig 2.2b). The intra-oral wounds were closed with tissue glue (Periacryl®, Glustitch Inc., Point Roberts, WA, USA).

2.3.4 Bone-implant interfacial stiffness determination

Twenty animals in the OA group were investigated for this part of study, with block biopsies being harvested at 7, 10, 14, and 21 days after implantation. These specimens were then secured in acrylic resin and the implants were pushed out of the maxillae using an MTS machine (Model 858, Mini-Bionix II., MTS Systems Corp., Eden Prairie, MN, USA) at a constant displacement rate of 0.1 mm/s. The maximum removing load (MRL) and interfacial stiffness (IS) were calculated from load-displacement curves (supplementary material, section 9.1). The score of osseointegration index system (OI) was evaluated after implant push-out (Table 2.1).

2.3.5 FE analysis to validate micro-CT examinations

The beam hardening and scattering effects from titanium implant micro-CT imaging can severely limit evaluation of implant-supporting tissues [13-15]. To validate use of micro-CT imaging within our study, we first evaluated the scattering effect from the titanium implants, and then designed a two-step FE model to evaluate potential tissue

damage after implant push-out.

To model the radiographic characteristics and spatial relationship of the implant within the alveolar bone, we cut the commercialized radiographic phantom to 3x3x2 mm-in-size and utilized a custom dental drill to make a 0.95 mm diameter penetration hole in the center and the titanium mini-implant was press-fitted into this pre-made hole. The phantom without implant placement was regarded as the control specimen. The micro-CT images were then processed using a GFHS Micro-CT system and analyzed with Micro-View Analysis (GE Healthcare) software. A higher voltage (90 kV) and copper filter were used to minimize any beam hardening effects, and images were reconstructed with a voxel size 27x27x27 μm^3. Imaging was repeated three times and the distributions of image grayscale were recorded.

Two computational models were developed to simulate the implant push-out procedure, and both of them were built axisymmetrically using ABAQUS v6.7-1 software (Simulia Inc., Northville MI, USA), which has been validated for studying biomechanical testing of dental implant systems [16]. All elements were assumed isotropic and the porosity of trabecular bone was neglected. Bone and implant were assumed to be bonded to each other, and a 5 μm cohesive layer was constructed between the implant and surrounding bone to simulate the interfacial proteoglycan layer. An automated mesh was generated for the dental implants and a Young's modulus value was assigned as 110 GPa, with a Poisson's Ratio as 0.35 [17]. A suspension-type boundary condition was assumed, meaning the outer border of bone tissue was constrained in the x-,

y-, and z- directions [18]. An interfacial break was dependent upon whether a cohesive element failure occurred, which had parameters set as strain in excess of 1.0%, and a fracture energy exceeding 4 joules [19].

In our first model, 20x20 μm^2 linear axisymmetric finite elements were assigned to the supporting bone, and three different Young's moduli (10000 MPa, 5000 MPa, and 1000 MPa) with a Poisson Ratio of 0.3 were utilized to simulate varying rigidities of bone. The cohesive layer property was assumed equivalent to the supporting bone. To simulate differences in bone-implant contact, 30%, 50%, 70%, and 100% implant surface area contacted by bone were analyzed. In total, 12 different quantities and qualities of supporting bone were created.

Our second model was based on an *in vivo* rat maxilla with a 1mm diameter osteotomy. Micro-CT scanning (GFHS Micro-CT system, GE HealthCare) with the voxel size of 18x18x18 μm^3 was performed to provide spatial relationships of mineralized structures, and the position of the implant was identified. The images were resampled and segmented using a previously described thresholding methodology [7,20], then transferred to an axisymmetric FE model with a customized MATLAB® (Mathworks Inc., Natick, MA, USA) program. Using the measurements from the maxillary micro-CT images, the mean transverse thickness of maxillae was 2.65 mm. From this peri-implant thickness value and isolation of the concentric area within a 1.3 mm radius from the center of the implant, we found no significant influence to the interfacial shear stress during push-out tests [21]. Based on a previous study, a 40 μm resolution is appropriate for numerical convergence

[22]. Considering the variation in density of the mineralized tissues, the supporting bone area was meshed using 18x18 μm^2 quadratic linear axisymmetric finite elements. The Young's modulus of each element was assigned by conversion of the mineral density data with the Poisson's ratio assumed as 0.3 [23], and the fail strain assumed as 1.0 % [24]. The bone and implant were assumed to be bonded to each other, and cohesive elements were utilized to simulate this interface, which was determined as 5 μm in thickness and 18 μm in length, with isotropic elasticity assumed for all the elements. To investigate the influence of the bone and implant contact (BIC) area, a 0.6 x 1mm circumferential peri-implant osseous defect was assumed, and based on observations from preliminary studies, several elements were removed to achieve 20% BIC (equivalent to wound healing at day 10) and 50% BIC (equivalent to day 14) models (Figure 2.3). IS of cohesive elements were assigned by conversion of the measurements from section 2.3.4, in which 'minimal' represented IS for day 7, 'moderate' for day 10, 'strong' for day 14, and 'maximal' for day 21.

The push-out process was simulated using linear static analysis in ABAQUS™, and the maximum principle strain was recorded after push-out. Considering possible deviation in load direction from the actual push-out procedure, a vertical load with 3 degree and 5 degree angulations to the vertical axis were also applied. The visible deformation under micro-CT was set at 2.5% strain level [19], and elements exceeding this threshold were colorized by greyscale. FE analyses were executed on a computer equipped with 3.2 GHz central processor unit and 2047MB RAM. Each simulation used approximately 10-20 seconds CPU time.

2.3.6 *In vivo* measurements

18 rats in the OS group were sacrificed at days 10, 14, and 21 following implant installation, with OA group animals serving as controls. All harvested specimens were processed for implant push-out testing, and interfacial biomechanical properties were recorded as described in section 2.3.4.

Following implant removal, micro-CT images were taken (Fig 2.1a-b, right panel), reconstructed, and segmented with a threshold determined by Otsu's adaptive technique [20]. Several parameters, including bone-implant contact (BIC), bone volume fraction (BVF), tissue mineral density (TMD), and bone mineral density (BMD), were evaluated to investigate osseous wound healing within the osseous defect area. Equivalent osseous defect areas were also segmented in the control group and served as the reference for complete osseointegration.

To determine the correlation between interfacial resistance and individual concentric area, the peri-implant tissue was concentrically segmented in 18 μm intervals ranging from 18-720 μm, and the total bone volume (BV), bone mineral content (BMC), and BMD from individual segments were calculated. Cumulative micro-CT parameters were also calculated to examine the range of supporting peri-implant tissues.

2.3.7 Functional Homogenization through FE optimization

FBAM and FCAM were generated from functional simulations in day-10 and

day-14 specimens in the OS and OA groups. Micro-CT images from section 2.3.6 were segmented and homogenized to establish FE models (Fig 2.2c,d) as described in section 2.3.5. The area of interest was assumed to be filled with mineral and granulation tissue. FBAM refers to the rigidity of bone within the area of interest toward the dental implant, and FCAM refers to rigidity of whole tissue (including mineral and granulation tissue) toward the dental implant. Two models for each parameter were established, and the 'microscopic model' contained all localized mechanical properties from the micro-CT images with 0.6 % yield strain and 1.0 % fail strain [24]. However, in the 'optimizing model', the local mechanical properties of native bone were still based on micro-CT images, whereas the area of interest was assumed homogeneous, and the rigidity was obtained through FE simulations described below. The Young's modulus was set at 200 MPa for the granulation tissue [25], and 110 GPa for the implant. The Poisson's ratio for all peri-implant elements was set at 0.3 except for the granulation tissue and titanium implant [17], which was set at 0.167 [25] and 0.35 [17] respectively. To simulate the interfacial area, 5x18 μm cohesive elements were used and were assumed to have the same Young's modulus and fail criteria as the supporting tissues. All elements were assumed to have isotropic elasticity.

A linear static analysis (ABAQUS™ v6.7-1 Simulia Inc., Northville MI, USA) was performed to simulate loading conditions of the submerged implant during early wound healing stages. A 0.1 μm axial displacement of the dental implants was applied for all simulations, which allowed all elements deformed not to exceed the 0.6% strain yield criterion [26]. The optimization was performed using a custom MATLAB® algorithm. A

total design of 31 experiments were performed and the square difference between the ‘microscopic’ and ‘optimizing’ models based on all principle strain values from all elements within the area of interest was recorded. The functional Young’s modulus was optimized through the cubic spline interpolations and least-square approximations.

FE analyses were executed on a computer equipped with 3.2 GHz central processor unit and 2047 RAM. Each simulation used 8-20 seconds CPU time, and the design of experiments and optimization procedures took 45-70 minutes per specimen. The functional apparent moduli ranged between the maximal and minimal Young’s modulus of bone or composite tissues.

Mathematical bone and composite tissue modulus (MBM & MCM) were calculated for comparison. Correlations between functional apparent modulus and either mathematical modulus or micro-CT structural parameters were examined to study the relevance between radiographic and functional information from the osseous defect sites. To investigate the efficacy of the functional parameters for predicting implant stability, FBAM and FCAM within the peri-implant concentric area were also generated and their correlation with IS and MRL was examined (Fig 2.2e,f).

2.3.8 Statistical analysis

All correlation analyses were determined by the Pearson correlation test. Differences in biomechanical, structural, and functionally-simulated parameters over time were determined by paired t tests for continuous data, and by Mann-Whitney U tests for

non-continuous data; $p<0.05$ was considered to mean statistically and significantly different.

2.4 Results

2.4.1 Promotion of interfacial biomechanics during dental implant osseointegration

The interfacial stiffness significantly ($p<0.01$) increased from day 7 through day 10 then gradually leveled off by day 21. The MRL and mean OI score also demonstrated similar tendencies as the IS. At day 21, most of the specimens revealed visible cortical bone fracture (Table 2.2, osteotomy-alone group).

2.4.2 Interfacial damage is not a significant factor following implant removal during early healing

All micro-CT images were normalized to the same brightness and contrast, and the grayscale histograms of a section passing through the center of the implant or surgical hole are shown on Fig 2.4. Irregular, high-intensity margins were detected surrounding the titanium implant, and the histograms demonstrated this area to be 120-150 μm from the borders of implant.

For our *in vitro* FE model, a total of 4207-7777 nodes and 4030-7600 elements (including 348 solid elements for the dental implant) were generated to evaluate any potential damage to the implant-supporting tissues. Complete separation between implant and the supporting tissues during the push-out procedure was seen in all stimulated experiments. The maximum principle strain is shown in Fig 2.5, and the strain gradually decreased with increasing distance from the interface, with tissue near the bottom of the implant experiencing the highest level of strain. A five degree deviation in removal direction caused more strain, but none of elements were beyond the radiographically

detectable level. The strain pattern was similar among different rigidities of bone (data not shown).

A range of 2754-4437 solid elements were generated on the implant-supporting tissues, and 42-104 cohesive elements were generated for the interface in the *in vivo* interfacial damage FE model (Table 2.3 and Fig 2.3, left panel). We found no significant difference in strain distribution among various angulated loading situations, and the maximum principle strain occurred at a 5 degree angulation load, with the compression site illustrated in Fig 2.3. The strain increased with elevations in interfacial stiffness, and greater defect fill led to a more favorable strain distribution due to fracturing. Although radiographically visible deformation of tissues was noted in several ofour analyses (Table 2.3), these situations were considered beyond the physiological processes of osseointegration. The results from FE analyses confirmed that implant removal did not lead to radiographically detectable deformation.

2.4.3 Biomechanical testing and micro-CT imaging of peri-implant wound repair

Progressive increases in OI score, IS, and MRL were noted in the OS group, and visible separation of cortical bone was evident after push-out in three of the day-21 specimens. However, the biomechanical and structural parameters were still significantly lower ($p<0.05$) compared to the OA group at day 10-14 (Table 2.2).

2.4.4 Correlations between functional apparent modulus and mathematical modulus or structural parameters during early healing

For our FE model of functional homogenization, a range of 2032-4096 solid elements were generated for implant-supporting tissues, 78-111 cohesive elements for the interface, and 348 solid elements for the dental implant. Both FBAM and FCAM were correlated to mathematical moduli for both the OS or OA groups. The most-correlated structural parameters to functional apparent moduli was BMD in the OA defects and BIC in the OS defects. FCAM also demonstrated more correlation to all other structural parameters in the OS defects when compared to FBAM (Table 2.4).

2.4.5 FBAM & FCAM during oral implant osseointegration

For the OS defects, FCAM was the only parameter that demonstrated the significant difference over time ($p<0.01$), and became equivalent to FBAM at day 14. However, in the OS group, FBAM did not change enough to display any significant differences when compared with OA defects at day 14 ($p<0.001$).

2.4.6 Correlations between interfacial resistance and micro-CT/functional parameters

From the innermost layer of the peri-implant area in the OA group, BV and BMC demonstrated the highest correlation to both IS and MRL, when compared with all other concentric layers (Fig 2.6a, d). Using cumulative layer analysis, BMC appeared to better predict IS at the 180 μm-thickness peri-implant layer ($R=0.70$, Fig. 2.6b). Although the micro-CT parameters and MRL were less correlated, the better predictor of MRL from BMD occured at the 180 μm-thickness layer ($R=0.501$, Fig. 2.6e). In the OS group, BV exhibited very weak correlation with both IS and MRL ($R<0.2$) from layer-by-layer

analysis (Fig. 2.6g, j). Using cumulative layer analysis, BMC displayed the highest correlation to both IS (R=0.66) and MRL (R=0.71) at the 576 μm-thickness level (Fig. 2.6h, k). FBAM demonstrated the highest correlation to both biomechanical parameters in the OA group within the 180 μm concentric layer (R>0.8, Fig. 2.6c, f) and FCAM had the highest correlation to both biomechanical parameters in the OS group from around 200 μm-thickness layer (Fig. 2.6i, j).

2.5 Discussion

In this study we combined micro-CT and FE analyses to calculate functional apparent modulus to present the functional capability of the peri-implant tissue. The results demonstrated that both FBAM and FCAM are correlated to mathematical modulus. FBAM is capable of expressing the biomechanical performance in an OA situation, and FCAM can better interpret the functional dynamics in an OS situation. While physical artifacts surrounding the titanium implant do not reflect a reliable bone-implant interfacial relationship (Fig 2.4), we demonstrated that meticulous removal of the implant did not create any significant radiographically detectable deformation through FE analyses (Fig 2.3, Fig. 2.5). Although visible damage did occur in some situations, it was initiated from the bottom of the interfacial tissues and the transition surface of newly-formed bone, which may not have any significant effect on quantitative measurement within a cervical osseous defect.

Our results showed significant enhancement of interfacial biomechanical and structural parameters from days 7 to 10, later accompanied by a progressive increase in the OA group (Table 2.1), which is comparable to the evidence from Franchi et al. [27]. They demonstrated that bone trabeculae quickly filled the initial gap at the bone-implant interface and arranged in a three-dimensional network of arches or bridges, thus offering initial implant stability. In the latter stages, bone deposition occurred within the framework of bone trabeculae, gradually enhanceing implant stability. However, several of our specimens experienced bone fracture during the implant push-out testing. There are two possible explanations: First, the interfacial bonding was tighter than for

trabecular structures, causing the trabecular structures to exceed failure prior to interface failure. Second, the trabecular arrangement of bone in our non-loaded model was unfavorable for distribution of forces, which would promote cracking. Further investigation to determine the mechanical parameters and modeling, using detailed trabecular structure or loading situations, may be necessary for improving damage prediction.

Although modern biomechanical assessments, such as nanoindentation or scanning acoustic microscopy, may provide microscopic mapping of mechanical properties of bone [28,29], the properties regarding the implant interface still cannot be directly measured. The implant interfacial properties can be investigated through functional testing of the implant, yet the heterogeneity of peri-implant tissue is usually neglected [30]. Thus, simulating an implant loading situation and using back-calculation from FE modeling to match the microscopic data may be clinically relevant for evaluating the dynamics of peri-implant tissue repair. Our results demonstrated variations between the mathematical and functional apparent moduli, and the differences in tissue moduli were more evident because of the highly heterogeneous nature and distribution of the tissues evaluated. Correlations between functional apparent modulus and the structural parameters indicated that the function of tissues did not depend on any single parameter. Therefore, the functional apparent modulus can help elucidate the osseous wound healing processes on implant-adjacent osseous wounds. In terms of FBAM, no significant differences in bone maturation between 10 and 14 days within the defect area was observed, which demonstrated that healing was still immature compared with the OA specimens. At 14

days, the tissue within the defect had significantly less FCAM compared with the OA group and there was significant difference between 10 and 14 days, indicating rapid bone apposition towards the implant surface. While bone is the rigidity-dominant tissue within the defect, a higher functional tissue/bone modulus fraction indicated the wound space was occupied by greater amounts of bone or, higher ratios of bone tissues were located near the tissue-implant interface. Since complete defect fill was not found in our osseous defect group (Table 2.1) at 14 days, the equivalent value between FCAM and FBAM revealed that the functional resistance from the newly-formed tissue was similar to the defect being completely occupied by bone tissue. Taken together, from days 10 to day 14, the dynamic profile of FCAM and FBAM indicated the main event in the osseous defect was rapid expansion of mineralized tissue thus providing greater support of the dental implant without significant maturation.

Implant stability is one of the critical factors for evaluating implant success and determining the timing for loading or abutment connection [30]. The relationship between structural parameters and implant stability, as well as the effective correlated range of peri-implant tissue has not been well-established [31]. Therefore, stronger correlations to interfacial resistance from functional apparent modulus has implied that integration of the peri-implant structural information is necessary for predicting the functional performance of the implant system. We have also identified the highest-correlating peri-implant zone as 180 μm in the OA situation, and around 200 μm in the OS situation. Considering this relationship may vary dependent upon the implant geometry and peri-implant status, further validation of these situations is needed.

2.6 Clinical Implications

It is impossible to remove the osseointegrated implant in most clinical situations while evaluating the functional progress of osseointegration. Thus, it is necessary to consider the metal scattering effects under radiographic imaging during clinical use.

The scattering effect on *in vivo* specimens was evaluated using a harvested rat maxilla with an 0.95x2 mm through-and-through osteotomy accompanying with 2.2x1 mm coronal osseous defect was created as described in section 2.3.3. An micro-CT image was taken under 90 kV with copper filter to achieve a final voxel size of 27x27x27 μm^3. After scanning, a 1x2 mm cylinder titanium implant was press-fit into the osteotomy site, and a second micro-CT scan was performed under the same setting. Utilizing Micro-View Analysis (GE Healthcare) software and custom MATLAB® computer algorithms, both of the images were oriented and normalized to the same Honusfield unit (HU). Mesiodistal straight lines crossing the middle of osseous defect (yellow line in Figure 2.7a,c) and osteotomy-only (blue line in Figure 2.7a,c) were made on the central sagittal plane of the osteotomy site respectively. Comparing the Honusfield units of voxels on the line, blurred high-intensity voxels were noted at 126-162 μm concentric area from the implant border in the osseous defect region as well as 108 μm in the osteotomy region (Figure 2.7b,d).

We further investigated the data from the specimens of section 2.3.6, comprised of 10 specimens from OA group (6 for day 10, and 4 for day 14) and 12 specimens from OS group (6 for day 10, and 6 for day 14). Considering the metal scattering was affecting the inner 108-162 μm peri-implant layer, we compared the micro-CT parameters as well as

the functional apparent moduli after cropping the innermost 0, 108, and 162 μm peri-implant layers. Results showed that the value of all the structural parameters and functional apparent moduli increased from day 10 to day 14, and significant difference was noted in both BV and BMC ($p<0.001$, Table 2.5). Removing the scattering-affected peri-implant tissue significantly decreased BV and BMC ($p<0.001$) but increased FBAM and FCAM ($p>0.05$). Although the increase in peri-implant layer removal reduced correlations with measurements from the whole defect area, correlations between non-artifact and artifact situations was strong in all the investigated parameters except BV and FCAM at day 10, and the correlation tended to be stronger over time (Table 2.5).

Layer-by-layer analysis was also performed after cropping 0, 108, and 162 μm peri-implant layer. Without consideration for physical artifacts, BMC (r=0.55-0.75 in IS, and 0.4-0.55 in MRL) was the most correlated structural parameter compared to BV (r=0.45-0.72 in IS, and 0.3-0.45 in MRL) and BMD (r=0.4-0.6 in IS, and 0.3-0.52 in MRL) to interfacial biomechanics in the OA situation. After removing the artifact-affected layer, both BMC and BV of the cumulative peri-implant layer demonstrated slightly lower correlation to IS as well as MRL within 600 μm radial zone, and this correlation tended to decrease with the increasing artifact area (Figure 2.8a-f). However, FBAM revealed strongest correlation over all the structural parameters in both IS and MRL ($r>0.9$) within 300 μm per-implant concentric area (Figure 2.8g,h).

Therefore, in the OS group, both BMC and BMD (r=0.5-0.7) demonstrated a stronger correlation to interfacial biomechanics than BV ($r<0.1$) within 600 μm radial

zone (Figure 2.9a-f) under no physical artifact. Removing the metal-scattering affected regions (108 or 162 μm innermost peri-implant layer) did not cause obvious change of correlations to the interfacial biomechanics in all the structural parameters except for slightly stronger correlations between BMC and MRL (Figure 2.8d), and weaker correlation between BV and IS (Figure 2.9b). FCAM showed the strongest correlation to IS (r=0.75-0.95) as well as MRL (r=0.35-0.95), especially within 200-300 μm radial peri-implant zone (r>0.75, Fig 2.8g,h).

To summarize, the micro-CT parameters and functional apparent moduli were correlated to the interfacial stiffness during osseointegration as well as osseous wound repair after eliminating 108-162 μm artifact-affected layers.

2.7 Conclusion

We conclude that micro-CT imaging can be used to provide three-dimensional information for implant-supporting tissues following implant removal. Both micro-CT and functional apparent modulus are capable of predicting the functional dynamics of implant-supporting osseous tissues and interfacial biomechanics during osseointegration, even after eliminating a 108-162 μm artifact-affected layers. These functional and imaging methods may provide key biomechanical information for the determination of timing of dental implant loading for clinical applications.

2.8 Tables

Table 2.1 Index of Osseointegration

Grade	Definition
0	Minimal contact. Interfacial stiffness < the value of day 7 OA specimens
1	Moderate contact. Interfacial stiffness > the value of day 7 OA specimens; no visible trabecular/cortical bone fracture
2	Trabecular bone fracture. No visible fracture or component loss on micro-CT, with macroscopically visible residual bone on the implant surface.
3	Mild cortical bone fracture. Fracture line on cortical bone detected on micro-CT; no significant bone component separation
4	Major cortical bone fracture. Separation of the bone components

Abbreviations: OA: osteotomy-alone

Table 2.2 Dynamic change of biomechanical, structural, and functional parameters over time

	Osteotomy-Alone Defect (OA)				Ostetomy + Osseous Defect (OS)		
	Day 7 (n=4)	Day 10 (n=6)	Day 14 (n=6)	Day 21 (n=4)	Day 10 (n=6)	Day 14 (n=6)	Day 21 (n=6)
Interfacial stiffness (N/mm)	67.66(42.57)	180.54 (30.79)$^{\#}$	229.16 (34.82)$^{\#}$	290.10 (57.97)$^{\$\#}$	28.82 (25.79)*	77.74 (45.90)*	161.67 (100.96)$^{\&}$
Osseointegration index score	0.50	1.17	2.50$^{\#}$	4.00$^{\$\#}$	0.17*	0.83*	3.33$^{\&}$
Maximal removal load (N)	2.52(1.69)	28.88 (7.93)$^{\#}$	44.65 (10.02)$^{\#}$	N.D.	5.29 (5.99)*	15.46 (7.09)*	N.D.
Bone-implant contact (mm^2)	0.95(0.33)	1.13 (0.21)	1.04 (0.12)	N.D.	0.30 (0.15)*	0.44 (0.21)*	N.D.
Bone volume fraction	0.72(0.04)	0.74 (0.13)	0.77 (0.06)	N.D.	0.43 (0.15)*	0.57 (0.07)*	N.D.
Tissue mineral density (mg/cc)	667.35(63.37)	801.74 (94.12)	823.82 (80.07)$^{\#}$	N.D.	311.28 (80.40)*	383.40 (102.56)*	N.D.
Bone mineral density (mg/cc)	804.58(39.2)	1078.69 (196.32)$^{\#}$	1078.09 (120.03)$^{\#}$	N.D.	583.71 (55.82)*	668.32 (119.09)*	N.D.
Mathematical tissue modulus (GPa)	N.D.	3.362 (0.511)	3.687 (0.107)	N.D.	1.071 (0.125)*	1.506 (0.202)*	N.D.
Functional tissue modulus (GPa)	N.D.	13.031 (1.807)	12.430 (2.965)	N.D.	3.801 (0.356)*	7.939 (1.318)$^{*\&}$	N.D.
Mathematical bone modulus (GPa)	N.D.	11.889 (0.922)	12.176 (1.692)	N.D.	7.687 (0.348)*	7.993 (0.507)*	N.D.
Functional bone modulus (GPa)	N.D.	11.979 (1.670)	12.312 (2.775)	N.D.	7.752 (0.258)*	8.745 (0.662)*	N.D.

* Significant difference to osteotomy-alone group at specific time points ($p<0.001$)

$^{\&}$ Significant difference to day 10 ($p<0.01$)

$^{\#}$ Significant difference to day 7 ($p<0.01$)

parentheses refers to standard deviation

N.D. Not determinable

Table 2.3 Element deformation as visualized radiographically

	Minimal stiffness	Moderate stiffness	Strong stiffness	Maximal stiffness
Osteotomy-alone	0/4133	0/4133	0/4133	2/4133
50% BIC	0/3801	0/3801	0/3801	1/3801
20% BIC	0/3302	0/3302	2/3302	10/3302
Empty defect	0/2352	8/2352	37/2352	84/2352

Radiographically visible deformed elements/total elements of the peri-implant tissue. The elements with more than 2.5% principle strain were defined as radiographically visibly deformed.

Table 2.4 Correlations between micro-CT and functional/mathematical modulus

Parameters	Osteotomy-Alone Defect (OA, n=14) FBAM	Osteotomy-Alone Defect (OA, n=14) FCAM	Osteotomy+Osseous Defect (OS, n=12) FBAM	Osteotomy+Osseous Defect (OS, n=12) FCAM
Functional/mathematical modulus				
R square	0.8925	0.2780	0.5856	0.6762
P value	N.S.	<0.0001	<0.0001	<0.0001
R square to functional apparent modulus*				
Bone-implant contact (BIC)	0.2755	0.2964	0.4243	0.7589
Bone volume fractions (BVF)	0.0869	0.0352	0.0057	0.4857
Tissue mineral density (TMD)	0.1203	0.0566	0.1113	0.4651
Bone mineral density (BMD)	0.8544	0.7364	0.3298	0.3708
R square to mathematical modulus*				
Bone-implant contact (BIC)	0.0604	0.4140	0.1135	0.6204
Bone volume fractions (BVF)	0.1546	0.7168	0.0132	0.4062
Tissue mineral density (TMD)	0.3476	0.6458	0.1231	0.4081
Bone mineral density (BMD)	0.5003	0.1641	0.4937	0.0080

*All the p value between micro-CT and functional/mathematical modulus were < 0.05

Abbreviations: FBAM: functional bone apparent modulus; FCAM: functional composite tissue apparent modulus

Table 2.5 Correlation of structural parameters and functional apparent moduli between artifact and non-artifact situations in osseous defect area

	Mean & standard deviations			Correlation to 0 μm artifact (r)	
	0 μm artifact	108 μm artifact	162 μm artifact	108 μm artifact	162 μm artifact
Bone volume (mm^3)					
Overall (n=12)	0.137(0.012)	0.118(0.012)#	0.111(0.012)#	0.955	0.934
Day 10 (n=6)	0.135(0.006)*	0.117(0.005)*#	0.110(0.005)*#	0.615	0.442
Day 14 (n=6)	0.138(0.016)	0.119(0.017)#	0.111(0.017)#	0.994	0.995
Bone mineral content (10^6 Honusfield unit)					
Overall (n=12)	3.95(0.83)	3.41(0.67)#	3.21(0.62)#	0.989	0.980
Day 10 (n=6)	3.40(0.74)*	2.94(0.57)*#	2.77(0.51)*#	0.984	0.970
Day 14 (n=6)	4.50(0.49)	3.87(0.38)#	3.64(0.35)#	0.971	0.949
Functional bone apparent modulus (GPa)					
Overall (n=12)	7.94(1.28)	8.15(1.39)	8.33(1.42)	0.987	0.956
Day 10 (n=6)	7.67(0.74)	7.87(0.97)	8.09(1.16)	0.964	0.900
Day 14 (n=6)	8.20(1.75)	8.43(1.83)	8.56(1.78)	0.996	0.989
Functional composite tissue apparent modulus (GPa)					
Overall (n=12)	6.03(2.98)	6.63(3.00)	6.79(2.82)	0.982	0.933
Day 10 (n=6)	4.19(0.71)	4.73(1.08)	5.14(1.42)	0.787	0.414
Day 14 (n=6)	7.87(3.35)	8.52(3.20)	8.43(3.05)	0.989	0.961

* Significant difference to day 14

Significant difference to 0 μm artifact situation

2.9 Figures

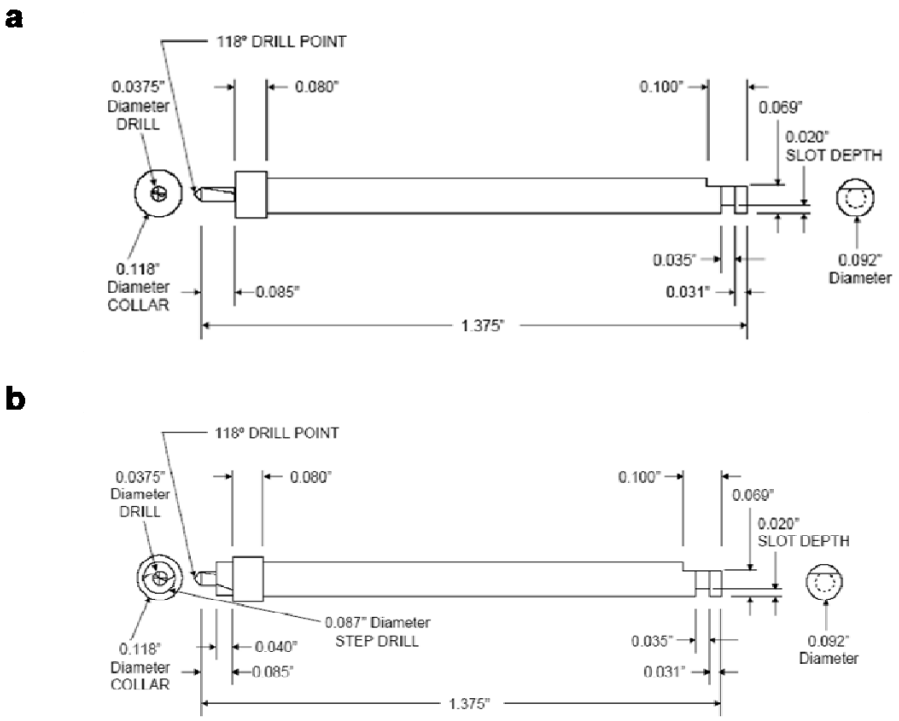

Figure 2.1 Customized step drills for creating (**a**) 0.95x2 mm osteotomy defect and (**b**) 0.95x2 mm osteotomy plus 2.2x1 mm cervical osseous defect.

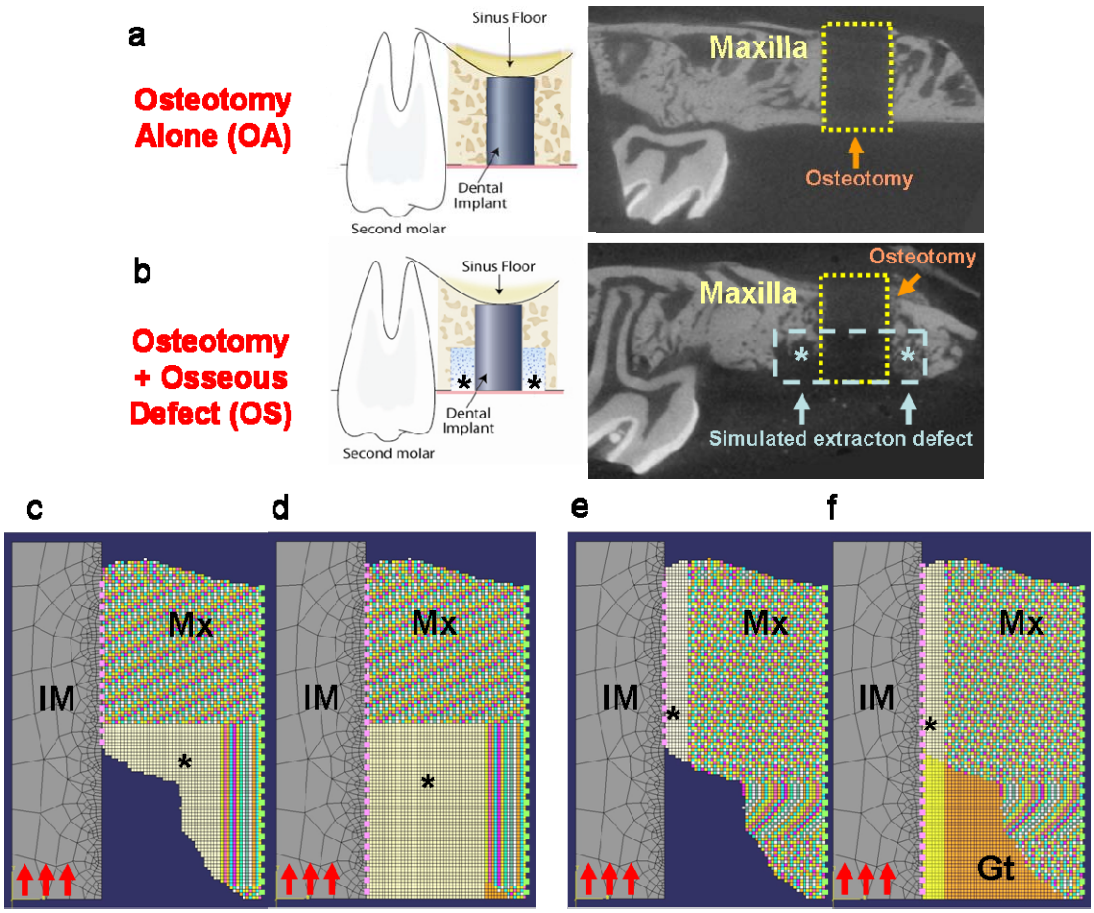

Figure 2.2 ***In vivo*** **dental implant osseointegration model for functional simulations.** The surgical model of osteotomy-only and osseous-defect group are demonstrated in the left panels of (**a, b)**.The right panels demonstrate a slice of micro-CT image from a 10-day specimen after implant removal (the 1x2mm area of osteotomy is marked by the yellow dashed line; the 0.6x1 mm area of simulated extraction defect is marked by blue dash line and asterisks). The optimized FM models are shown on (**c**) FBAM and (**d**) FCAM for evaluation of osseous wound repair, (**e**) FBAM and (**f**) FCAM of interfacial tissue for evaluating the correlation to interfacial biomechanics. Suspended boundary (dash lines in light green) was assumed, and the bone-implant interface (dash lines in pink) was assumed homogenous and simulated using cohesive elements. In each model, the Young's modulus of the mineralized tissue (Mx) was projected from the grayscale of micro-CT

images, whereas the dental implant (IM) and granulation tissue (Gt) was obtained from reference. The Young's modulus of the bone or tissue in the area of interest (asterisk) was calculated from the functional loading from the oral cavity (red arrows). The elasticity of interface was assumed equivalent to the peri-implant element nearby. Osteotomy-alone (OA) and osteotomy with osseous defect (OS) specimens were examined for each simulation (n=12-14 for each group).

Abbreviations: FE: finite element; FBAM: functional bone apparent modulus; FCAM: functional composite tissue apparent modulus

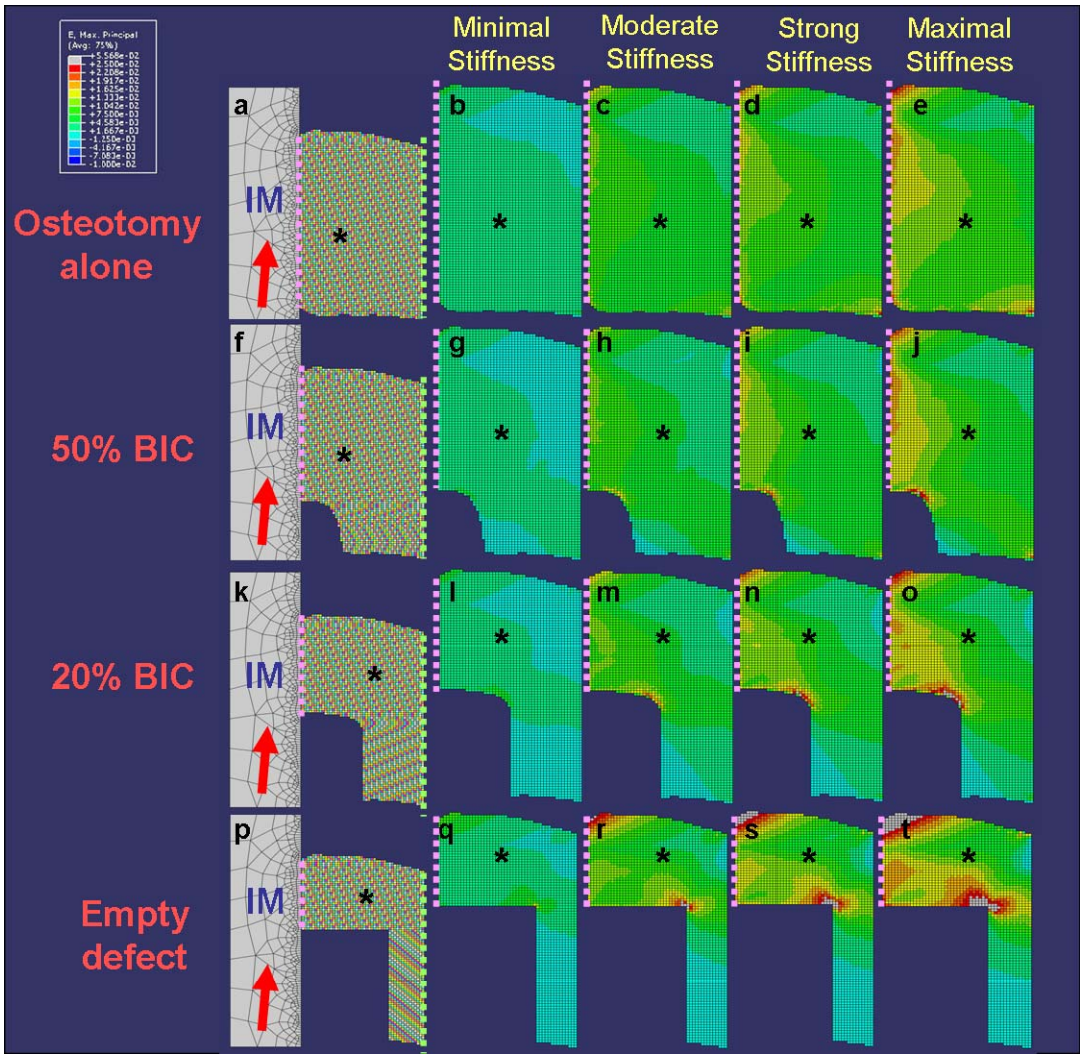

Figure 2.3 Finite element model and maximum principle strain distribution of implant-supporting tissues after implant removal. Four axissymmetric models were generated to evaluate the effects of osseous wound repair over time (**a, f, k, p**).The maximum principle strain of the peri-implant tissue on the compression side (asterisks, and bone-implant interface referred to the dash line) after implant (IM) removal with 5 degree angulations (red arrows on **a,f,k,p**) was recorded (**b-e, g-j, l-o, q-t**). The osseous defect was set as 0.6mm-in-width and 1.0 mm-in-depth surrounding the dental implant (**d**), 20% bone-implant-contact (BIC) referred to normal healing wound at day 10 (**k**), 50% BIC referred to normal healing wound at day 14 (**f**), and osteotomy-only referred to no defect creating specimens (**a**). Suspended boundary

(dash lines in light green on **a,f,k,p**) was assumed, and the bone-implant interface (dash lines in pink) was assumed homogenous and simulated using cohesive elements. Four different interfacial bonding situations were assigned for evaluations, whereas minimal, moderate, strong, and maximal stiffness was assigned according to the record from push out testing on the osteotomy-only group at day 7, 10, 14, and 21 (referred to Table 2.4). The elements with radiographically visible deformation (experienced more than 2.5% strain) were colorized by grey.

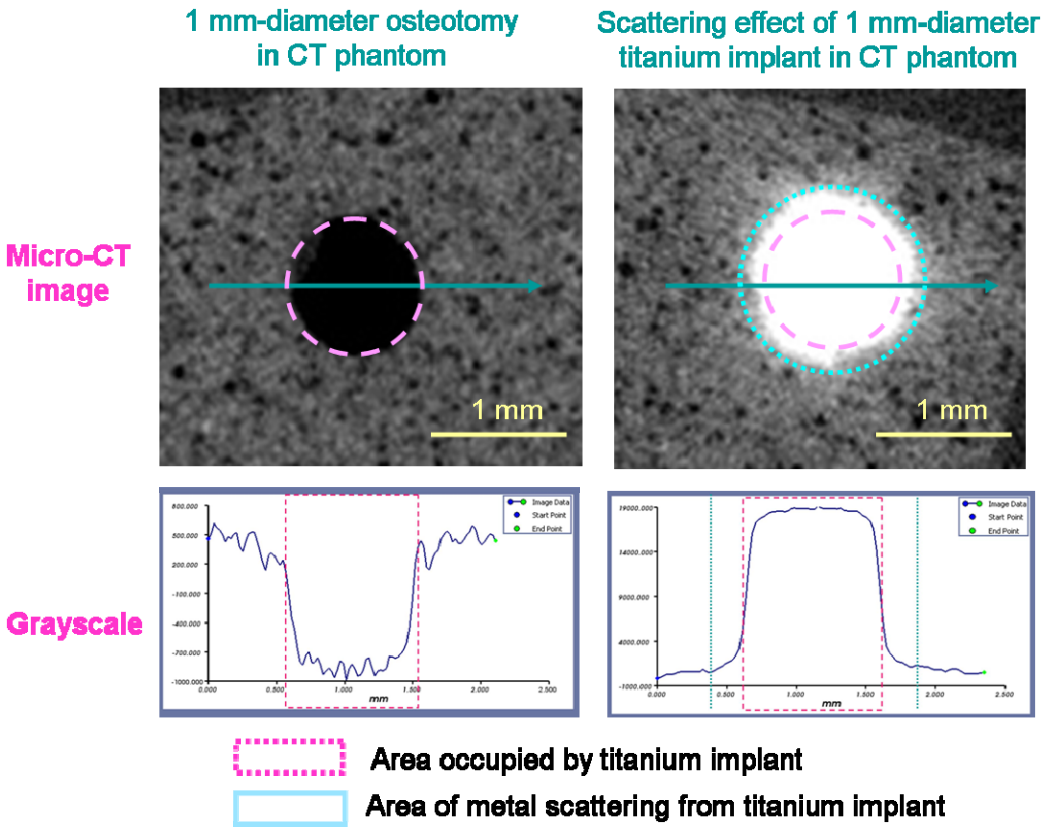

Fig 2.4 Scattering effect from titanium implants installed into CT phantom blocks. Significantly higher intensity gray level pixels extending from the implant border (purple dash line) were noted on the micro-CT images (upper panel, right), and those pixels distributed about 120-150 μm around the implant border (the area between the blue and purple dash lines).

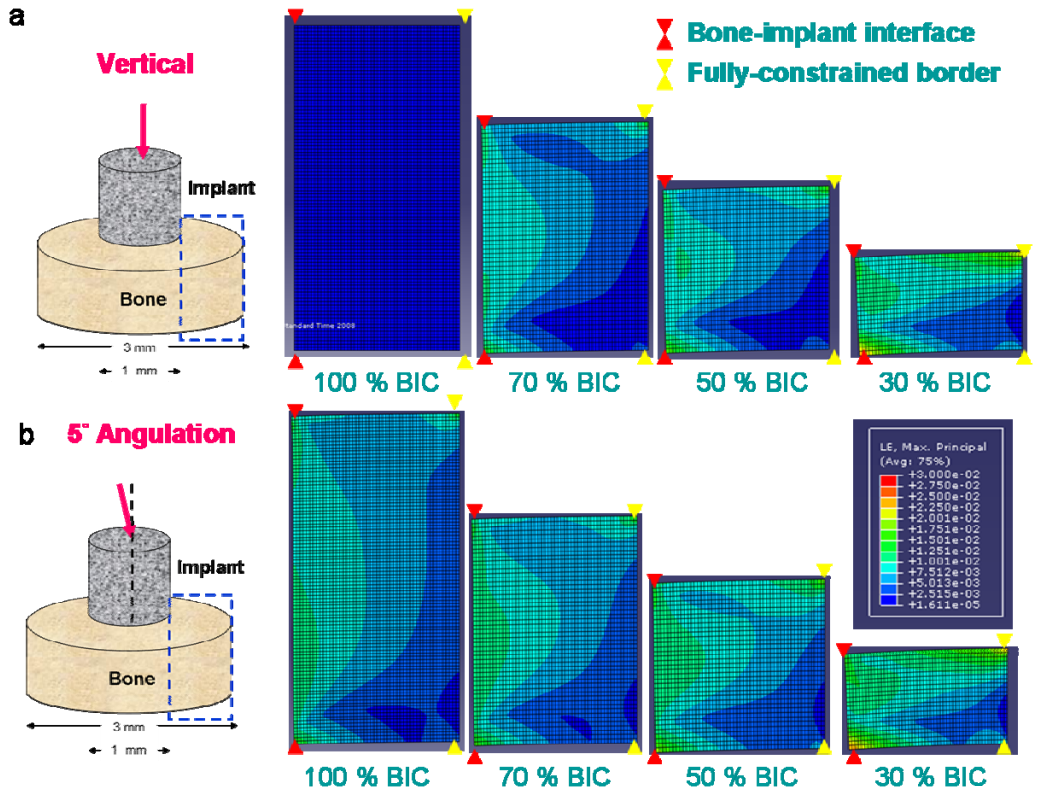

Figure 2.5 The strain distribution of implant-supporting tissue from different bone-implant contact (BIC) ratio and angulation of pushing-out force. The strain distribution of implant removal vertically (upper panel) and 5 degrees of deviation (lower panel) demonstrated that the strain increased with decreasing areas of contact, and the maximum strain occurred near the bottom of the interface. Within a 5 degree deviation of implant removal did not significantly result in radiographic detectable deformation.

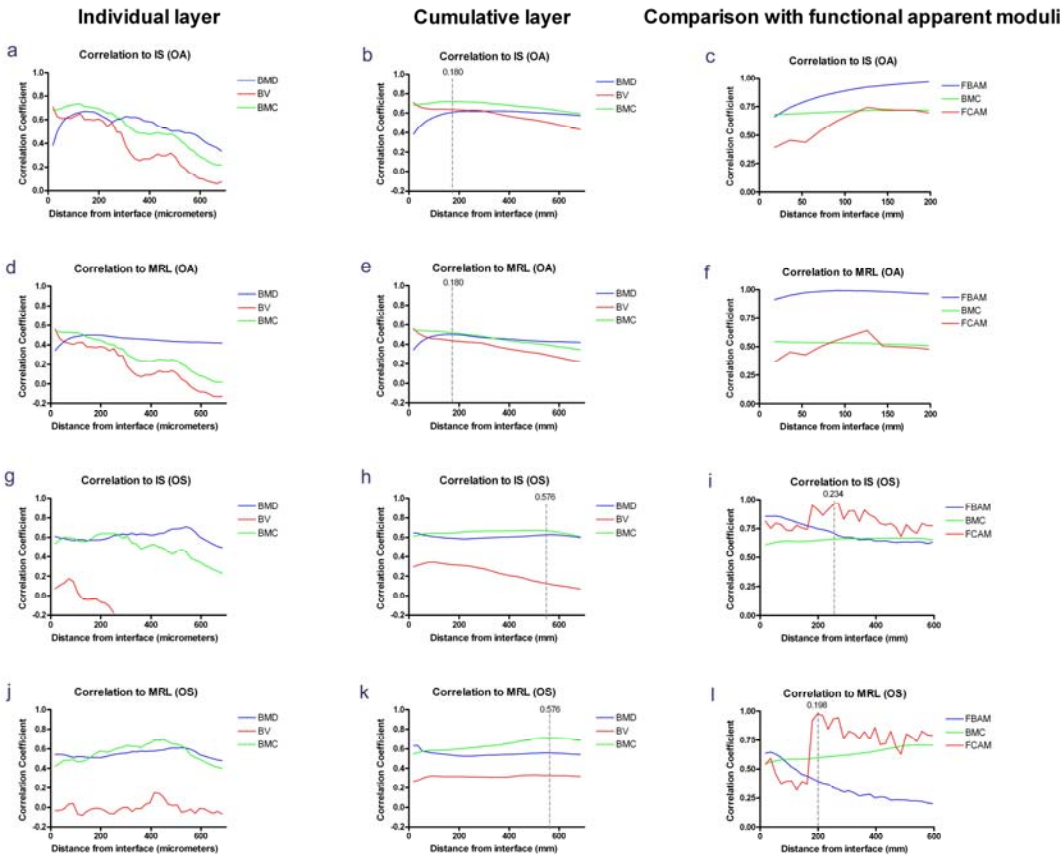

Figure 2.6 Relationship between interfacial resistance and micro-CT/functional parameters. Correlation coefficient of interfacial resistance (IS and MRL) and micro-CT parameters (BMD, BV, BMC) was evaluated by 0.018 mm thick individual concentric peri-implant tissue layer (**a,d,g,j**) and cumulative layer (**b,e,h,k**) in osteotomy-alone (OA) and osteotomy+osseous defect (OS) groups. While stronger correlation between micro-CT parameters and interfacial resistance was noted in the 0.180 mm thickness peri-implant region of OA group (**b,e**), and 0.576 mm in the OS group (**h,k**), further calculation of correlation coefficient of functional parameters (FBAM and FCAM) and interfacial resistance (IS and MRL) was performed within 0.200 mm concentric peri-implant area in the OA group (**c,f**), and 0.600 mm area in the OS group (**i,l**).

Abbreviations: IS: interfacial stiffness; MRL: maximal removal load; BMD: bone

mineral density; BV: bone volume; BMC: bone mineral content; FBAM: functional bone apparent modulus; FCAM: functional composite tissue apparent modulus

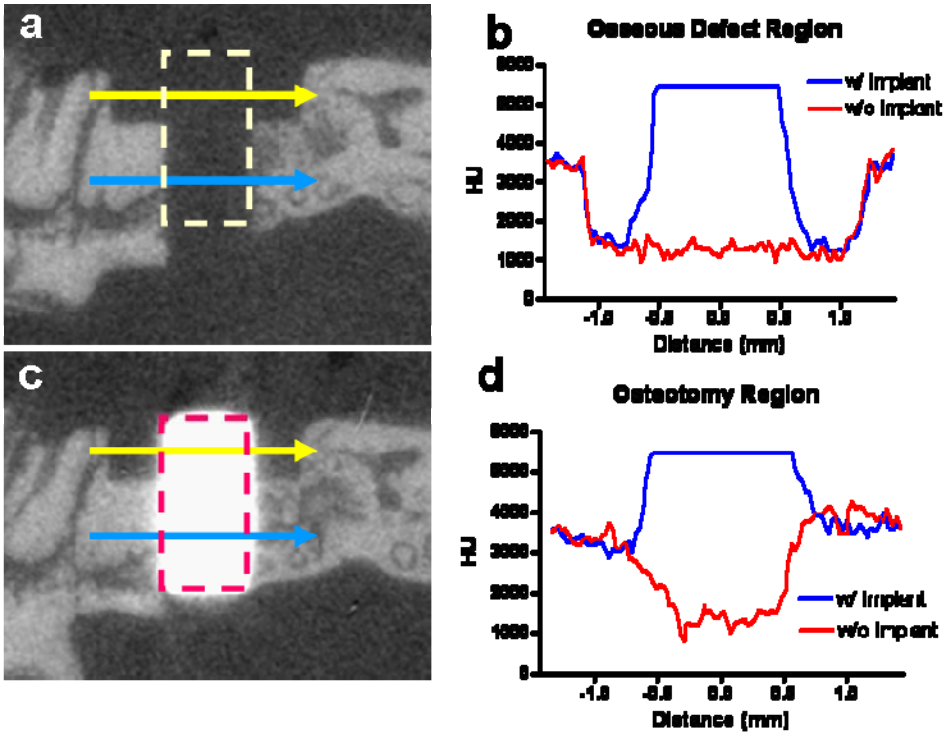

Figure 2.7 *in vivo* Metal Scattering Effects on Micro-CT Imaging

Micro-CT imaging before and after implant placement are shown on (**a,c**). The area marked by the dash line refers to the space occupied by the titanium implant, the yellow line indicates the osteotomy-osseous defect region, and blue line for osteotomy-alone region. (**b**) 126 μm blurred zone on the left and 162 μm on the right side of the implant was noted in the osteotomy-osseous defect region. (**d**) In osteotomy-alone area, an 108 μm scattering-affected zone is noted on the both sides of the implant (HU: Honusfield unit).

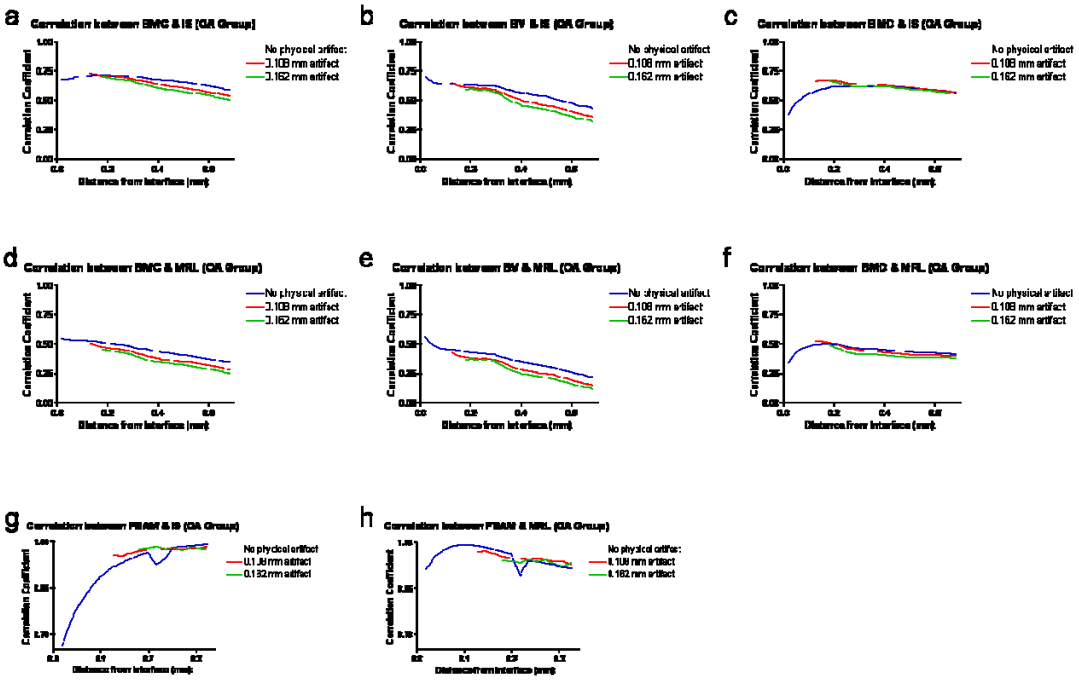

Figure 2.8 Correlation between Artifact And Non-artifact Situations in Osteotomy-alone (OA) Group

Correlation coefficient between structural parameters (BMC, BV, and BMD) and IS (**a,b,c**) as well as MRL (**d,e,f**) was evaluated from cumulative peri-implant layer within 630 μm thickness, and the correlation between FBAM and interfacial biomechanics (IS and MRL) was evaluated within 324 μm concentric zone (**g,h**). In each analysis, either 108 or 162 μm innermost layer was assumed to be affected by metal scattering effect and was removed to investigate the "artifact" situations.

Abbreviations: BMD: bone mineral density; BV: bone volume; BMC: bone mineral content; IS: interfacial stiffness; MRL: maximal removing load; and FBAM: functional bone apparent modulus

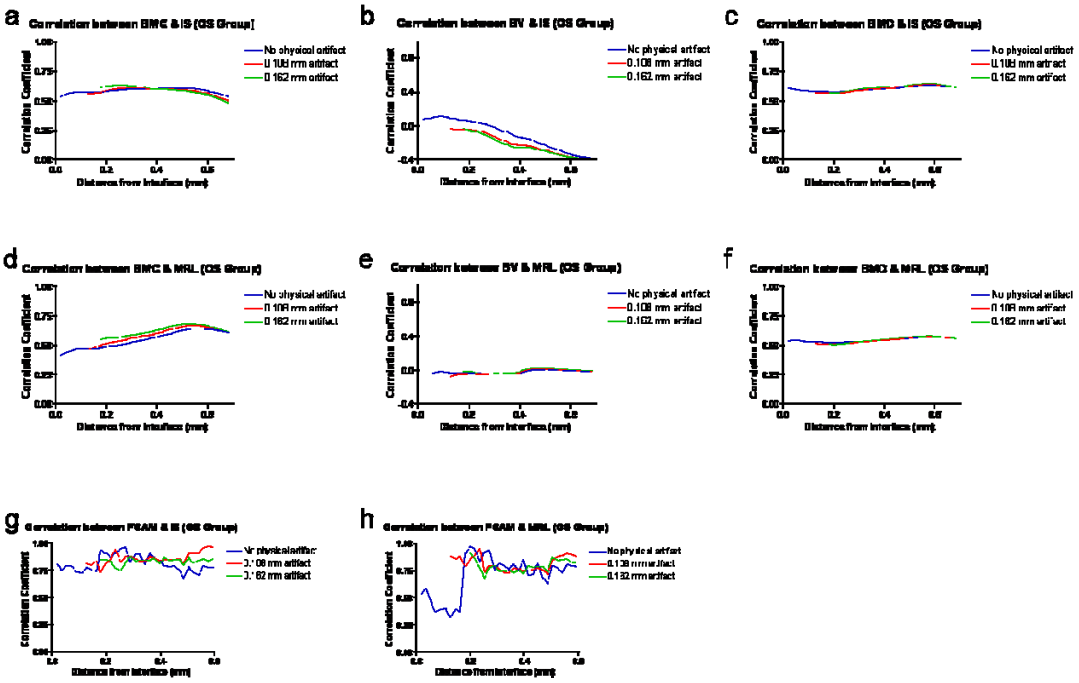

Figure 2.9 Correlation between Artifact And Non-artifact Situations in Osteotomy-osseous Defect (OS) Group

Correlation coefficient between structural parameters (BMC, BV, and BMD) and IS (**a,b,c**) as well as MRL (**d,e,f**) was evaluated from cumulative peri-implant layer within 630 μm thickness, and the correlation between FCAM and interfacial biomechanics (IS and MRL) was evaluated within 612 μm concentric zone (**g,h**). In each analysis, either 108 or 162 μm innermost layer was assumed to be affected by metal scattering effect and was removed to investigate the "artifact" situations.

Abbreviations: BMD: bone mineral density; BV: bone volume; BMC: bone mineral content; IS: interfacial stiffness; MRL: maximal removing load; and FCAM: functional composite tissue apparent modulus

2.10 References

1. Berglundh, T., Abrahamsson, I., Lang, N.P. & Lindhe, J. De novo alveolar bone formation adjacent to endosseous implants. *Clin Oral Implants Res* **14**, 251-62 (2003).
2. Futami, T. et al. Tissue response to titanium implants in the rat maxilla: ultrastructural and histochemical observations of the bone-titanium interface. *J Periodontol* **71**, 287-98 (2000).
3. Stoppie, N., Wevers, M. & Naert, I. Feasibility of detecting trabecular bone around percutaneous titanium implants in rabbits by in vivo microfocus computed tomography. *J Microsc* **228**, 55-61 (2007).
4. Yang, J. & Xiang, H.J. A three-dimensional finite element study on the biomechanical behavior of an FGBM dental implant in surrounding bone. *J Biomech* **40**, 2377-85 (2007).
5. Himmlova, L., Dostalova, T., Kacovsky, A. & Konvickova, S. Influence of implant length and diameter on stress distribution: a finite element analysis. *J Prosthet Dent* **91**, 20-5 (2004).
6. Natali, A.N., Pavan, P.G. & Ruggero, A.L. Analysis of bone-implant interaction phenomena by using a numerical approach. *Clin Oral Implants Res* **17**, 67-74 (2006).
7. Hollister, S.J., Brennan, J.M. & Kikuchi, N. A homogenization sampling procedure for calculating trabecular bone effective stiffness and tissue level stress. *J Biomech* **27**, 433-44 (1994).
8. Renders, G.A., Mulder, L., Langenbach, G.E., van Ruijven, L.J. & van Eijden, T.M. Biomechanical effect of mineral heterogeneity in trabecular bone. *J Biomech* **41**, 2793-8 (2008).
9. Morgan, E.F. et al. Contribution of inter-site variations in architecture to trabecular bone apparent yield strains. *J Biomech* **37**, 1413-20 (2004).
10. Sennerby, L. & Meredith, N. Implant stability measurements using resonance frequency analysis: biological and biomechanical aspects and clinical implications. *Periodontol 2000* **47**, 51-66 (2008).
11. Dunn, C.A. et al. BMP gene delivery for alveolar bone engineering at dental implant defects. *Mol Ther* **11**, 294-9 (2005).
12. Jin, Q., Anusaksathien, O., Webb, S.A., Printz, M.A. & Giannobile, W.V. Engineering of tooth-supporting structures by delivery of PDGF gene therapy vectors. *Mol Ther* **9**, 519-26 (2004).
13. Van Oossterwyck, H. et al. Use of microfocus computerized tomography as a new technique for characterizing bone tissue around oral implants. *J Oral Implantol* **26**, 5-12 (2000).
14. Barrett, J.F. & Keat, N. Artifacts in CT: recognition and avoidance. *Radiographics* **24**, 1679-91 (2004).
15. Stoppie, N. et al. Validation of microfocus computed tomography in the evaluation of bone implant specimens. *Clin Implant Dent Relat Res* **7**, 87-94 (2005).
16. Hansson, S. The implant neck: smooth or provided with retention elements. A biomechanical approach. *Clin Oral Implants Res* **10**, 394-405 (1999).
17. Koca, O.L., Eskitascioglu, G. & Usumez, A. Three-dimensional finite-element analysis of functional stresses in different bone locations produced by implants placed in the maxillary posterior region of the sinus floor. *J Prosthet Dent* **93**, 38-44 (2005).
18. Holmgren, E.P., Seckinger, R.J., Kilgren, L.M. & Mante, F. Evaluating

parameters of osseointegrated dental implants using finite element analysis--a two-dimensional comparative study examining the effects of implant diameter, implant shape, and load direction. *J Oral Implantol* **24**, 80-8 (1998).
19. Keaveny, T.M., Wachtel, E.F., Ford, C.M. & Hayes, W.C. Differences between the tensile and compressive strengths of bovine tibial trabecular bone depend on modulus. *J Biomech* **27**, 1137-46 (1994).
20. Otsu, N. Threshold Selection Method from Gray-Level Histograms. *Ieee Transactions on Systems Man and Cybernetics* **9**, 62-66 (1979).
21. Dhert, W.J. et al. A finite element analysis of the push-out test: influence of test conditions. *J Biomed Mater Res* **26**, 119-30 (1992).
22. Niebur, G.L., Yuen, J.C., Hsia, A.C. & Keaveny, T.M. Convergence behavior of high-resolution finite element models of trabecular bone. *J Biomech Eng* **121**, 629-35 (1999).
23. Keller, T.S. Predicting the compressive mechanical behavior of bone. *J Biomech* **27**, 1159-68 (1994).
24. Ramasamy, J.G. & Akkus, O. Local variations in the micromechanical properties of mouse femur: the involvement of collagen fiber orientation and mineralization. *J Biomech* **40**, 910-8 (2007).
25. Kelly, D.J. & Prendergast, P.J. Prediction of the optimal mechanical properties for a scaffold used in osteochondral defect repair. *Tissue Eng* **12**, 2509-19 (2006).
26. Chevalier, Y., Pahr, D., Allmer, H., Charlebois, M. & Zysset, P. Validation of a voxel-based FE method for prediction of the uniaxial apparent modulus of human trabecular bone using macroscopic mechanical tests and nanoindentation. *J Biomech* **40**, 3333-40 (2007).
27. Franchi, M. et al. Biological fixation of endosseous implants. *Micron* **36**, 665-71 (2005).
28. Fan, Z., Smith, P.A., Eckstein, E.C. & Harris, G.F. Mechanical properties of OI type III bone tissue measured by nanoindentation. *J Biomed Mater Res A* **79**, 71-7 (2006).
29. Bumrerraj, S. & Katz, J.L. Scanning acoustic microscopy study of human cortical and trabecular bone. *Ann Biomed Eng* **29**, 1034-42 (2001).
30. Atsumi, M., Park, S.H. & Wang, H.L. Methods used to assess implant stability: current status. *Int J Oral Maxillofac Implants* **22**, 743-54 (2007).
31. Molly, L. Bone density and primary stability in implant therapy. *Clin Oral Implants Res* **17 Suppl 2**, 124-35 (2006).

CHAPTER 3

EFFECTS OF PLATELET-DERVIED GROWTH FACTOR TREATMENT BY PROTEIN OR GENE DELIVERY ON PROMOTING DENTAL IMPLANT OSSEOINTEGRATION

3.1 Abstract

Platelet-derived growth factor-BB (PDGF-BB) stimulates repair of healing-impaired chronic wounds such as diabetic ulcers and periodontal lesions. However, limitations in predictability of tissue regeneration occur due in part to transient growth factor bioavailability *in vivo*. Here, we report that gene delivery of PDGF-B stimulates repair of oral implant extraction socket defects. Alveolar ridge defects were created in rats (n=100) and were treated at the time of titanium implant installation with a collagen matrix containing an adenoviral (Ad) vector encoding PDGF-B ($5.5x10^8$ or $5.5x10^9$ pfu/ml), Ad encoding luciferase (Ad-Luc; $5.5x10^9$ pfu/ml; control) or recombinant human PDGF-BB protein (rhPDGF-BB, 0.3 mg/ml). Bone repair and osseointegration were measured via backscattered SEM, histomorphometry, microcomputed tomography, and biomechanical assessments. Results demonstrated bone repair was accelerated by Ad-PDGF-B and rhPDGF-BB delivery compared to Ad-Luc, with the high dose of Ad-PDGF-B more effective than the low dose. In summary, gene delivery of Ad-PDGF-B demonstrates regenerative and safety capabilities for bone tissue engineering and

osseointegration in alveolar bone defects comparable to rhPDGF-BB protein delivery *in vivo*.

3.2 Introduction

Oral implants are widely accepted in dental medicine as a reconstructive treatment modality for tooth replacement due to disease, injury, or congenital defects. In clinical situations exhibiting limited alveolar bone availability, growth factor application has been advocated to improve osteogenesis and osseointegration [1]. However, as a result of the transient action and high degradation rate of recombinant proteins *in vivo* [2], the sustained bioactivity of gene therapy vectors has been purported to be an effective alternative for the delivery of growth factor proteins [3,4]. Adenoviral vectors (Ad) have been shown to exhibit a high *in vivo* transduction efficiency [5] with a relatively short expression period compared with other viral-based gene delivery methods, and their effectiveness for promoting initial wound healing without eliciting long-term health concerns in wound healing models [6,7].

Platelet-derived growth factor (PDGF) is a potent mitogen that facilitates wound healing [8] and stimulates bone repair by expanding osteoblastic precursor cells [9,10]. PDGF-BB is FDA-approved for use in the treatment of localized periodontal defects and diabetic ulcers [11-13]. Ad-mediated PDGF-B (Ad-PDGF-B) gene delivery has been shown to enhance periodontal tissue regeneration of tooth-supporting wounds [6,14].

Limited information is available regarding the potential of PDGF-BB on promoting osseointegration of oral implants. In addition, the influence of PDGF-B on the mechanical integrity of an implant interface is unknown. The purpose of this study was to investigate the effects of rhPDGF-BB and Ad-PDGF-B delivered in a collagen matrix on

the osteogenesis and osseointegration of dental implants in an *in vivo* osseointegration model in the rat, and *in vitro* investigations were conducted to supplement the *in vivo* experimental results. This approach demonstrates the ability of Ad-PDGF-B to accelerate oral implant osseointegration. The data support the concept that Ad-PDGF-B gene delivery may be an effective mode of therapy to promote dental implant osseointegration and oral bone repair.

3.3 Materials and Methods

3.3.1 Preparation of Adenovirus-Gene Activated Matrix

Ad-PDGF-B (E1-, E3-deleted adenovirus serotype 5 encoding human platelet-derived growth factor-B) and Ad-Luc (E1-, E3-deleted adenovirus serotype 5 encoding firefly luciferase) have been previously described [6]. In both vectors, transgene expression is under control of the CMV promoter. Titers of virus stocks were determined on embryonic kidney 293 cells by plaque assay and expressed as the particle number per milliliter [7].

Ad-PDGF-B and Ad-Luc were dialyzed into GTS buffer (2.5% glycerol, 25 mM NaCl, 20 mM Tris, pH 8.0) and formulated in bovine fibrillar type I collagen matrix (Matrix Pharmaceutical Inc., Fremont, CA, USA) at a final concentration of 2.6%.

3.3.2 Animal model for evaluating therapeutic effects.

A total of 100 male Sprague-Dawley rats were used in this study and the general timeline for study is shown in Fig 1a. All animal procedures followed the guidelines from the Committee on Use and Care of Animals of the University of Michigan asdescribed in section 2.3.3. A custom cylinder-type titanium mini-implant (gift of Institut Straumann AG, Basel, Switzerland), 1 mm-in-diameter and 2 mm-in-depth, was press-fit into the 0.6x1 mm circumferential surgically-created socket (Fig 3.1b), and the remaining defect was then filled with the type I collagen matrix containing $5.5x10^9$ pfu/ml Ad-Luc, $5.5x10^8$ pfu/ml Ad-PDGF-B, $5.5x10^9$ pfu/ml Ad-PDGF-B, or 0.3 mg/ml rhPDGF-BB (Fig 3.1b). Ad-Luc has not previously exhibited biological activities in dentoalveolar

defects [14] and served as control group in this study. The surgical area was covered by gingival tissue and closed using butyl cyanoacrylate (Periacryl®, Glustitch Inc., Point Roberts, WA, USA). The vital fluorochrome dye, calcein (10 mg/kg), was injected intra-muscularly after 3 days, and antibiotics (268 mg/L ampicillin in 5% dextrose water) were provided in the first 7 days post-operation.

3.3.3 Backscattered SEM and histology

Maxillae containing the implants were harvested upon sacrifice, with one side of maxillae taken for backscattered SEM and histology while the contralateral maxillae were used for biomechanical assessments (*see following section*). The specimens were fixed in 50% ethanol for at least 72 hours and subsequently embedded in epoxy resin. The specimens were then sectioned in the longitudinal direction relative to the implants using a diamond saw blade (Crystalite Co., Westerville OH, USA), then polished to achieve a 50-100 μm final thickness. The tissue mineralization was evaluated under the backscattered mode on Qanta F1B SEM with 45x magnification, calibrated with aluminum and carbon discs [15], and transferred to physical density using bone substitute radiographic phantoms (Gammex Inc., Middleton WI, USA). The photographs were then segmented and threshholded by Otsu's adaptive technique [16]. To eliminate any metal scattering effect, the measured bone-implant interface was defined as the horizontal distance 5μm from the outermost homogenous high-intensity area. The defect borders were projected using the calcein fluorescent images. Bone-area fractions (BAF, the fractions of bone inside the defect to the total area of defect) and Tissue mineral density within the defect (TMD, the total mineral content within the defect divided by the total

area of defect) were measured from backscattered SEM images. Next, histologic staining by methylene blue was performed, with the acid fuschin utilized as the counterstain. Bone-implant contact (BIC, the length of bone contacting the titanium) and defect fill (DF, the fraction of area of tissue regenerated divided by the total area of defect) were measured.

3.3.4 Biomechanical, three-dimensional radiographic, and functional evaluations.

The remaining maxillae were used for biomechanical and micro-CT evaluation and stored in normal saline at -20°C to preserve the mechanical integrity. After thawing at room temperature, the specimens were rapidly secured in acrylic resin, and the implant push-out procedure was performed as described in section 2.3.4. The region from 20% to 80% of the maximum removal load (MRL) was chosen and a linear regression was performed to calculate the interfacial stiffness (IS). A customized osseointegration index (OI) was introduced to further document the interfacial biomechanical behavior (Table 2.1).

Micro-CT scans were performed using an eXplore Locus SP Micro-CT system (GE HealthCare, London, ON, Canada) and reconstructed to voxel size of 18x18x18 μm^3. The spatial relationship of the mini-implant and surrounding tissues was then analyzed using a customized MATLAB® (Mathworks Inc., Natick, MA, USA) algorithm, and segmented with a threshold determined by Otsu's adaptive technique (section 2.3.6) [16]. Several parameters were quantitatively evaluated within the osseous defect areas: (1) Bone volume fraction (BVF): the volume of mineralized tissue within the osseous wound

divided by the volume of osseous wound; (2) Tissue mineral density (TMD): the mineral content of the radiographic-defined mineralized tissue within the osseous wound divided by the volume of osseous wound; After micro-CT evaluations, the images were transferred to create a finite element (FE) mesh, and functional composite tissue apparent modulus (FCAM, rigidity of the whole tissue within the area of interest toward dental implant) were generated as described in section 2.3.7.

3.3.5 Cell culture and gene transfer

Primary bone marrow stromal cells (BMSC) were harvested from the femur of 4-week-old male Sprague-Dawley rats by the aspiration method[17]. The cells were cultured in Dulbecco's Modified Eagle's Medium (DMEM) containing 10% fetal bovine serum (FBS) and supplemented with 100 U/ml of penicillin, 100 mg/ml of streptomycin, and 2.5 mg/ml of amphotericin B until passage 6 to 8. In all experiments, cells were cultured in a low-serum (DMEM containing 1% FBS and antibiotics) tcondition for 24 hours, and then treated with Ad-PDGF-B at a multiplicity of infection of 200, or with 20 ng/ml rhPDGF-BB in low-serum osteogenic medium (DMEM with 1% FBS, 100 μg ascorbic acid, 5 mM β-glycerophosphate, 100 nM dexamethasone, and antibiotics). After 3 hours of treatment in both groups, the media was replaced with fresh. The cells were continuously incubated in low-serum osteogenic medium and harvested at baseline (prior to treatment), 72, and 120 hours post-treatment. Each *in vitro* experiment was performed in triplicate and repeated at least 3 times.

3.3.6 Assay for DNA synthesis

Mitogenic activity of cells was measured from the [^{3}H]thymidine uptake. Briefly, cells were seeded on 12-well plates at 2500 cells/well and 0.5 μCi [^{3}H]thymidine/well was added immediately after Ad-PDGF-B or rhPDGF-BB treatment. Cells were harvested at 5 days post-treatment, fixed with 5% trichloroacetic acid (TCA) for 1 hour at 4°C, then incubated with 1% sodium dodecyl sulfate (SDS) for 1 hour at 55°C and transferred to scintillation vials for measuring tritium levels on a Wallac 1410 liquid scintillation counter. The results are expressed as counts per minute (CPM) in triplicate cell culture wells.

3.3.7 Assay for alkaline phosphatase

Alkaline phosphatase activity was measured by colorimetric procedures. Cells were seeded on 12-well plates at 10000 cells per square centimeter and harvested at 5 days after Ad-PDGF-B or rhPDGF-BB treatment. The cells were lysed by treating with 1mM magnesium chloride and 0.2% NP-40 solutions at 37°C for 15 minutes, and the protein concentrations were determined using a Bio-Rad protein assay (Bio-Rad Laboratories, Hercules, CA, USA). Then, 7 μl of each lysate was assayed for enzyme activity in 96-well plate format with p-nitrophenylphosphate (Sigma-Aldrich, St Louis, MO, USA) at 37°C for 15 minutes, stopped with 0.5 N NaOH, and the absorbance was measured at 415 nm.

3.3.8 PDGF-regulated gene expression

Gene expression was examined by real-time polymerase chain reactions (PCR). The cells were seeded on 12-well plates with 10000 cells per square centimeters density. RNA

was extracted from the cell lysates using RNeasy Micro kit (QIAGEN Inc., Valencia, CA, USA) as described by manufacturer. 12 μl RNA solutions were then mixed with TaqMan Reverse Transcription Reagents (Roche Molecular Sysmtes, Inc., Branchburg, NJ, USA) to make the final volume 50 μl for the reverse-transcription reactions. The solutions were incubated at 25°C for 10 minutes, then 48°C for 30 minutes, and finally inactivated at 95°C for 5 minutes.

For real-time quantitative PCR, ABI Prism Sequence Detection System 7700 (Applied Biosystems, Foster City, CA USA) were used. The thermal condition was: 25°C 10 minutes, 48°C 30 minutes and 95°C 5 minutes. PCR was performed using TaqMan Universal PCR Master Mix (Applied Biosystems). Briefly, a 30 μl PCR reaction was prepared with 0.5 μl cDNA from reverse transcription and 1.5μl mixture of gene specific probe (FAM dye) and primers mixture, including platelet-derived growth factor receptor-beta (PDGFRb, assay id, Rn00709573_m1), runt-related transcription factor-2 (RUNX2, assay id, Rn01512298_m1), and glyceraldehyde-3-phosphate dehydrogenase (GAPDH, assay id: Rn99999916_s1). All the primers and probes were obtained from Applied Biosystems. The thermal condition was: 50°C 2 minutes, 95°C 10 minutes followed by 40 cycles (except 50 cycles for osteocalcin) of 95°C 15 sec and 60°C 1 minute. In each PCR reaction, the standard curve was determined from serial dilution of the specimen harvested prior to treatment (regression correlation coefficient > 98%). All experimental results were then normalized to the value of GAPDH, and the relative expression was presented as the ratio to the baseline.

3.3.9 Statistical Analysis

One-way ANOVA with Tukey test was utilized to analyze the difference of histomorphometric, backscattered SEM, micro-CT, biomechanical, and functional parameters between PDGF-treated (collagen containing 0.3 mg/ml rhPDGF-BB, $5.5x10^8$ or $5.5x10^9$ pfu/ml Ad-PDGF-B) and non-PDGF-treated (collagen alone) groups in each time point. For evaluating the safety profile, the difference of vector replicates, hematological and chemical parameters between experimental (collagen containing $5.5x10^8$ or $5.5x10^9$ pfu/ml Ad-PDGF-B) was evaluated for time-dependent dynamics with control (collagen alone) group using Bonferroni post-tests, and the significance was assessed by repeated-measures ANOVA. The statistical difference was considered with a p value of less than 0.05.

3.4 Results

3.4.1 Animal Model and Experimental Design

A rat dental implant osseointegration wound model was modified for the *in vivo* experiments. To evaluate osteogenesis and osseointegration we delivered collagen matrix containing $5.5x10^9$ pfu/ml Ad-Luc (control), $5.5x10^8$ or $5.5x10^9$ pfu/ml Ad-PDGF-B, or 0.3 mg/ml rhPDGF-BB. To determine the safety profile of the approach collagen matrix alone was utilized as the control and matrix containing $5.5x10^8$ or $5.5x10^9$ pfu/ml of Ad-PDGF-B was used as the test agent.

3.4.2 Ad-PDGF-B and rhPDGF-BB enhance osteogenesis *in vivo*

Based on the descriptive histology (Fig 3.2a), by day 10 we observed a gradual defect resolution over time in all groups. At days 10 and 14, woven bone and primary trabecular bone were noted at the coronal margin (red asterisks) in Ad-Luc-treated specimens, and thicker bone trabeculae and defect fill were evident in all PDGF-treated specimens (black asterisks in $5.5x10^8$ and $5.5x10^9$ pfu/ml Ad-PDGF-B, and rhPDGF-BB). Also at day 14, more mature bone apposition and near-complete defect fill was noted for all PDGF-treated specimens (Fig 3.2a, lower panel). The histomorphometric measurements of the $5.5x10^9$ pfu/ml Ad-PDGF-B and rhPDGF-BB groups showed significantly higher bone-implant contact (BIC) than the Ad-Luc group at day 10 ($p<0.05$, Fig. 3.2b). Further, all PDGF groups revealed higher defect fill (DF) than Ad-Luc at days 10 ($p<0.01$, Fig. 3.2c) and 14 ($p<0.05$, Fig. 3.2c). At day 10, backscattered SEM (BS-SEM) measurements also demonstrated a significant difference between all PDGF-treated groups compared with the Ad-Luc-treated group in both bone-area fraction

(BAF, $p<0.05$, Fig 3.3b) and tissue mineral density (TMD, $p<0.05$, Fig 3.3c). A significant difference between rhPDGF-BB and Ad-Luc in TMD was also noted at day 14 ($p<0.05$, Fig. 3.3c). By day 21, no significant difference for any BS-SEM or histomorphometric parameters could be found among all the groups (data not shown).

3.4.3 Both Ad-PDGF-B and rhPDGF-BB promote osseointegration

The consequence of push-out testing was reflected from the osseointegration index (OI), with all PDGF-treated specimens showing higher scores than Ad-Luc, with significant differences noted between rhPDGF-BB and Ad-Luc at both days 10 and 14 ($p<0.05$, Fig 3.4a). PDGF application tended to improve the interfacial stiffness (IS) and maximum removal loading (MRL) compared to the Ad-Luc group. The rhPDGF-BB treatment demonstrated significantly higher interfacial stiffness (IS) than all other groups at days 10 and 14 ($p<0.05$, Figure 3.4b), and higher maximum removal loading (MRL) than all other groups at day 10 ($p<0.05$, Fig 3.4c). At day 14, the MRL of rhPDGF-BB was significantly higher compared to both the Ad-Luc and the $5.5x10^9$ pfu/ml Ad-PDGF-B groups ($p<0.05$, Fig 3.4c). Significant improvement of IS using $5.5x10^8$ pfu/ml Ad-PDGF-B treatment versus Ad-Luc ($p<0.05$, Fig. 3.4b) was also seen at day 10. Most day 21 specimens experienced cortical bone fractures during the push-out testing (suggestive of strong osseointegration), and no significant differences among all the groups in IS and OI scores were noted (data not shown).

Micro-CT images were analyzed after implant removal, and both the $5.5x10^9$ pfu/ml Ad-PDGF-B and rhPDGF-BB groups displayed significantly higher bone volume

fraction (BVF) and tissue mineral density (TMD) than the $5.5x10^8$ pfu/ml Ad-PDGF-B and Ad-Luc groups at day 10 ($p<0.05$, Fig. 3.4d, e). A significant difference in BVF was found between $5.5x10^9$ pfu/ml Ad-PDGF-B and Ad-Luc at day 14 ($p<0.05$, Fig 3.4d). Both the $5.5x10^9$ pfu/ml Ad-PDGF-B and rhPDGF-BB groups displayed equivalent extents of functional composite tissue apparent modulus (FCAM), which was significantly stiffer than the $5.5x10^8$ pfu/ml Ad-PDGF-B or Ad-Luc groups at day 10 ($p<0.05$, Fig. 3.4f). At day 14, there were no FCAM differences between any of the treatment groups.

3.4.4 PDGFs enhance mitogenesis without causing long-term osteogenic differentiation *in vitro*

Both rhPDGF-BB and Ad-PDGF-B treated cultures demonstrated significant enhancement of mitogenesis from DNA synthesis assay at day 5 ($p<0.05$, Fig 3.5a). However, significantly lower alkaline phosphatase (ALPase) activity was noted in Ad-PDGF-B treatment compared to control at this time ($p<0.05$, Fig 3.5a). No significant difference could be seen among groups at day 3, and progressive cell death was observed after 5 days in all our cultures (data not shown). Further investigations using realtime PCR demonstrated the gene expression level of PDGF receptor-beta (PDGFRb) and runt-related transcription factor-2 (RUNX2) recovered at day 3 in rhPDGF-BB treated specimens (Fig 3.5b) and up to 5 days for AdPDGF-B treatment (Fig 3.5c).

3.5 Discussion

This study demonstrates that both Ad-PDGF-B gene and rhPDGF-BB protein delivery promotes the acceleration of neo-osteogenesis of peri-implant bony defects *in vivo*. The affect on bone apposition were examined through DF from histomorphometry (Fig 3.2c), BAF from BS-SEM (Fig 3.3b), and BVF from micro-CT (Fig 3.4d). From these results, all treatment groups, especially the $5.5x10^9$ pfu/ml Ad-PDGF-B and rhPDGF-BB groups showed significantly greater bone formation compared to the Ad-Luc vector control group at 10 days. Regarding bone maturation, the Ad-Luc-treated defects showed sparse and limited new bone formation and slower bone formation within the defect area compared to the other three groups. By day 14, in the Ad-Luc group, new bone near the base of the defect (Fig. 3.2a) showed thick trabeculae and bone marrow formation suggesting greater maturation, whereas the thin trabeculae and primary woven bone-like structures at the coronal portion of the defects suggests early-stage osteogenesis. However, in all PDGF-treated groups, advanced bone maturation throughout the defect area, especially in the higher dose Ad-PDGF-B and rhPDGF-BB groups, indicates that new bone formation initiated earlier in those two groups compared to controls. Taken together, these results strongly suggest that PDGF delivery, via both the protein and the gene delivery vector, significantly accelerated and enhanced new bone formation in the peri-implant defects, and the higher dose of Ad-PDGF-B showed more favorable results than lower dosage suggesting a dose-dependent effect on osseointegration.

We also presented FCAM predicting the functional contribution of the newly-formed bone through the FE optimization procedures [18]. FCAM is more correlated

to the implant interfacial resistance than any single structural parameter. Significantly higher FCAM from the $5.5x10^9$ pfu/ml Ad-PDGF-B and rhPDGF-BB treatments at day 10 indicates that both PDGF protein and gene delivery stimulates not only osteogenesis but also favorable initial implant function.

Two-dimensional and three-dimensional quantification results between rhPDGF-BB and higher dose Ad-PDGF-B were also comparable (Fig 3.2-4). However, the biomechanical analyses did not show equivalent trends, whereas rhPDGF-BB demonstrated significant improvements versus Ad-Luc for most of the parameters (Fig 3.4a-c). Although the correlation between implant stability and peri-implant structures had been proven in previous research [19,20], this finding may be due to the different delivery profile of PDGF by either Ad or as a protein. While the initial response to a bolus administration of rhPDGF-BB may be robust, the protein's short half-life results in rapid degradation within a few days [2], and a decrease in the mitogenic response. In contrast, Ad-PDGF-B delivery demonstrates a delayed PDGF-BB expression profile that gradually decreases to ~20% of the highest level by day 14 *in vivo* [14]. This finding is consistent with a previous report whereby Ad-PDGF-B prolongs PDGF signaling leading to a delay with respect to timing of osteogenic differentiation [21].

PDGF's effects on osseous wound healing have been reported mechanistically in previous investigations. It had been shown that PDGF signaling is important for chemotaxis and proliferation of osteoblasts and fibroblasts [22,23]. However, PDGF's ability to induce osteogenic lineage differentiation is less clear. Tokudaga et al. [24] reported

PDGFRβ signaling strongly inhibited osteogenic differentiation of mesenchymal stem cells, and Kono et al. [25] further validated that the Erk signaling, which is the subsequent PDGFR pathway, negatively regulated osteogenesis. On the other hand, other evidence implies that PDGF contributes to osteogenic differentiation in more of a downstream mechanism. Huang et al. [26] detected PDGF mRNA expression at both the early proliferation stage and a late differentiation stage of osteoprogenitor cells. Furthermore, Ng et al. [27] showed that PDGFR activation was a key step for the osteogenic lineage differentiation of mesenchymal stem cells, while inhibition of PDGFR resulted in decreased mineralized nodule formation. Kratchmarova et al. [28] reported that PDGF increased new bone formation *in vivo* despite limited influences in osteogenic differentiation *in vitro*. These results imply that the differentiation is promoted at a certain level of expression, such as dose- or time-dependent reactions [22,23]. Donatis et al. [22] reported that a higher concentration of PDGF is favorable for mitogenesis and lower doses for cell motility. Hsieh et al. [23] found that pulse application of PDGF enhances bone formation, but prolonged exposure to PDGF limited *in vitro* bone regeneration. Since osteogenesis involves a cascade of events *in vivo*, varying strategies of PDGF delivery must be considered for different indications. The rhPDGF-BB treatment may be suitable for the needs of rapid bone fill, where it would quickly recruit cells without significantly affecting the time frame of subsequent differentiation. The higher dose of Ad-PDGF-B may be a better choice for a large wound site, in which the sustained PDGF signal would attract cell progenitors for a more extended, but still limited period of time. Thus, given the limited size of the rat maxilla and the high cell proliferative activity, it is necessary to further validate this assumption in a large animal model with more

challenging, critical-size defects.

The angiogenic effect of PDGF, which are similar to the effect of vascular endothelial growth factor (VEGF), may also be favorable for osseous wound repair. During wound healing, angiogenesis is an important event for new tissue regeneration (i.e., providing nutrients and essential signals). The PDGFs have a similar structure to VEGF [29], and PDGF-BB enhances fibroblast growth factor-2 (FGF-2) stimulated VEGF release [30]. PDGFRβ also has an important role in angiogenesis [31]. Therefore, it is reasonable to conclude that PDGF-BB also positively affects angiogenesis and ultimately contributes to bone formation. Considering that dental implant function (with a metallic non-vascularized interface) is largely dependent on the surrounding bone quantity, quality and wound healing microenvironment, these accelerating and enhancing bone formation effects of PDGF may promote greater bone volume for earlier implant placement and loading.

3.6 Conclusions

This investigation demonstrates the first reported use of Ad-PDGF-B administration to promote alveolar bone repair and osseointegration in alveolar ridge defects. These findings suggest that Ad-PDGF-B stimulates osseointegration that is comparable with delivery of PDGF-BB protein.

3.7 Figures

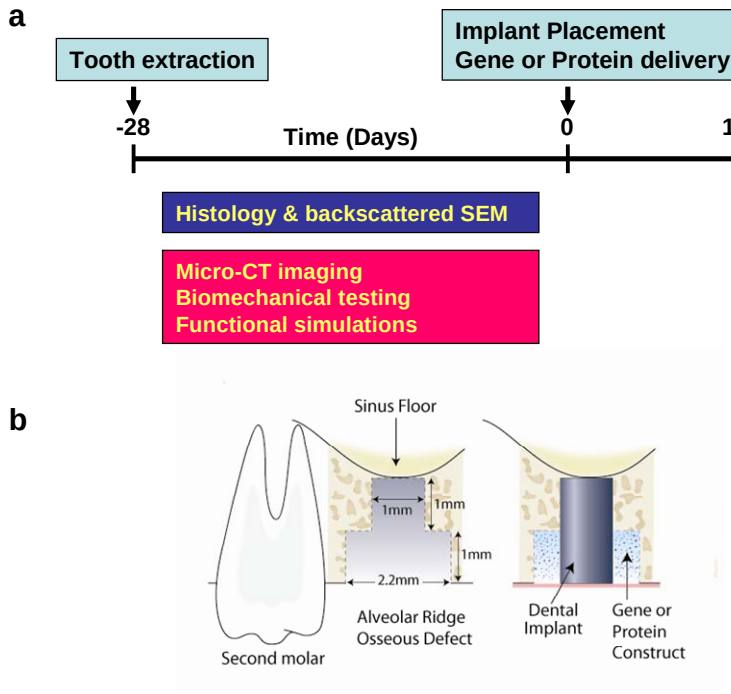

Figure 3.1 Experimental design (a) and experimental model illustration (b). Implant surgery was performed four weeks following maxillary first molar extraction. To create a consistent and reproducible defect, custom-made step drills were used. After dental implant placement, the bone defect was filled with $5.5x10^9$ pfu/ml Ad-Luc, $5.5x10^8$ pfu/ml Ad-PDGF-B, $5.5x10^9$ pfu/ml Ad-PDGF-B or 0.3 mg/ml rhPDGF-BB formulated with the collagen matrix for evaluating osseointegration (n=6-8/group/time point). Histomorphometric and backscattered SEM measurements were done at days 10, 14 and 21 after implant installation, and three dimensional evaluations (micro-CT imaging) as well as functional assessments (biomechanical testing and functional simulations) were done at days 10 and 14 after implant installation. For evaluating the safety profile, the bone defect was filled with $5.5x10^8$ pfu/ml Ad-PDGF-B, $5.5x10^9$ pfu/ml Ad-PDGF-B, or collagen matrix alone. The hematology, chemical chemistry, and vector dissemination were evaluated over a period of 35 days (n=6/group/time point).

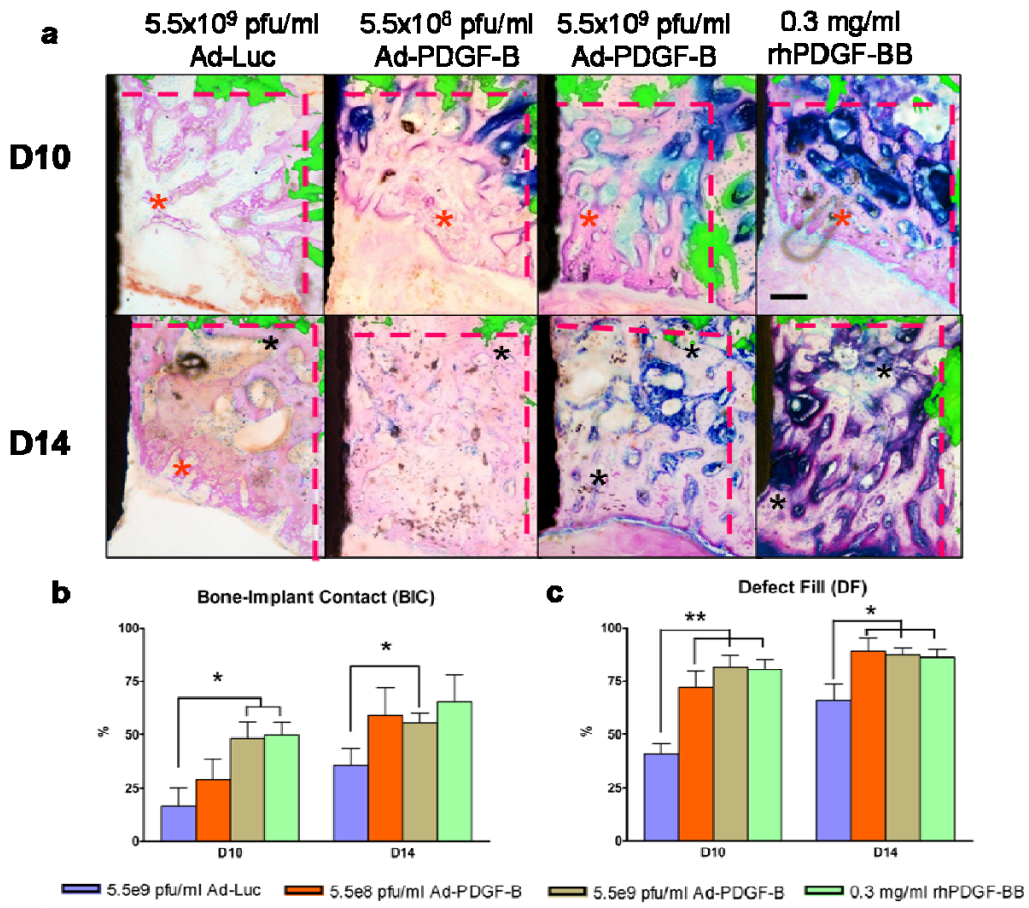

Figure 3.2 Histologic view of each group for 10 days and 14 days (a) and 2-D evaluations; bone-to-implant contact (BIC) (b), defect fill (c). (**a**) Histologic images were overlapped by fluorescent images made by calcein injection 3 days after surgery. The fluorescence indicates the original defect boundaries. The results of Ad-Luc defects show sparse bone formation at day 10 and a lesser degree of bone maturation at 10 and 14 days. All the PDGF-related specimens showed increased new bone formation at 10 and 14 days compared to Ad-Luc group. Scale bar in top right panel represents 200 μm. (Original magnification: ×40). (**b**) In BIC analysis, $5.5x10^9$ pfu/ml Ad-PDGF-B and rhPDGF-BB groups showed significantly higher ratio than the control group at 10 days and $5.5x10^9$ pfu/ml Ad-PDGF-B showed significantly higher ratio than control group at 14 days. (**c**) In defect fill analysis, all three PDGF treatment groups showed higher fractions than Ad-Luc treated defects at 10 and 14 days. Black area in left side: dental implant, black asterisks; matured new bone, red asterisks; young new bone, and dashed line; borders of the osseous defect. Data are

presented as mean and bars indicate standard error measurement (n=6-8).* $p<0.05$, ** $p<0.01$, *Abbreviations: BIC: bone to implant contact; DF: defect fill.*

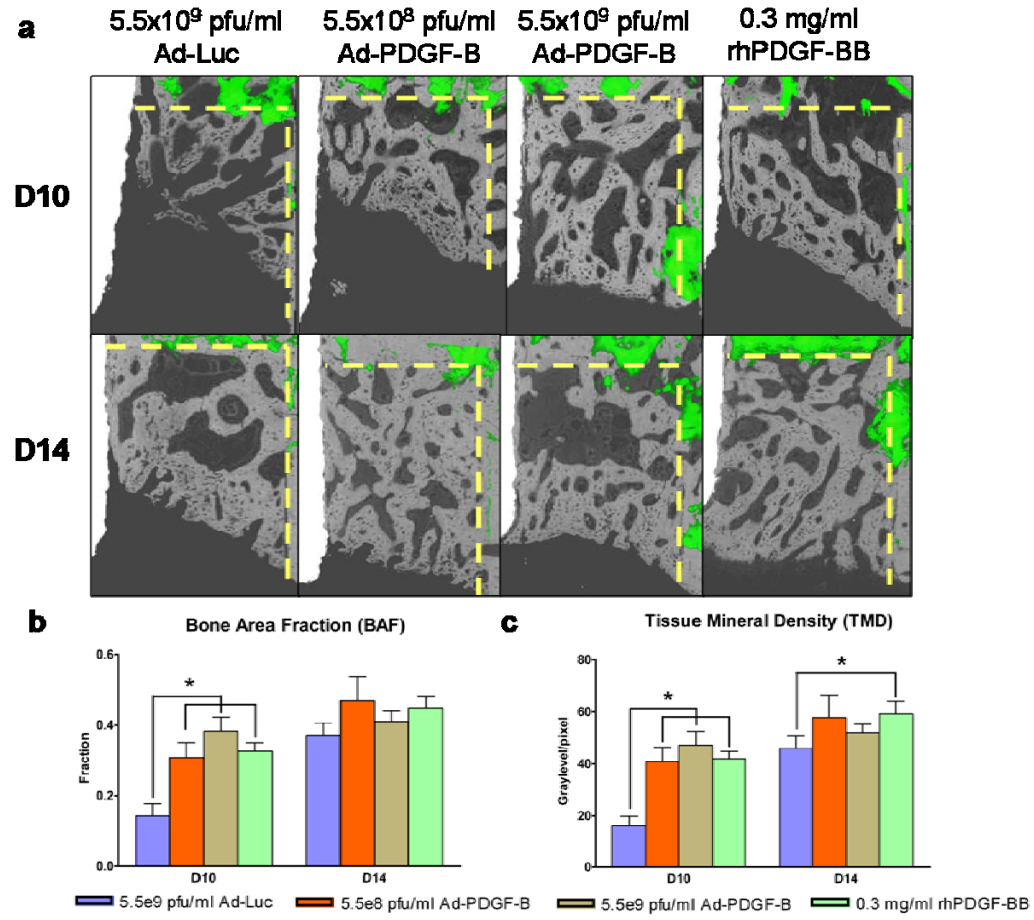

Figure 3.3 Back-scattered SEM (BS-SEM) images (a) and 2-D evaluations; bone area fraction (b), and tissue mineral density (c).

(**a**) BS-SEM images were merged with fluorescent images (dashed line; borders of the osseous defect.). The BS-SEM images show mineralized tissue against the oral implant surface. (Original magnification: ×42) (**b**) The three PDGF treatment groups showed a significant difference in bone area fraction at 10 days compared to the control group. (**c**) The three PDGF groups also showed significant differences in tissue mineral density at 10 days and the rhPDGF-BB group showed significance at 14 days compared to Ad-Luc defects. Data are presented as mean and bars indicate standard error measurement (n=6-8). * $p<0.05$.

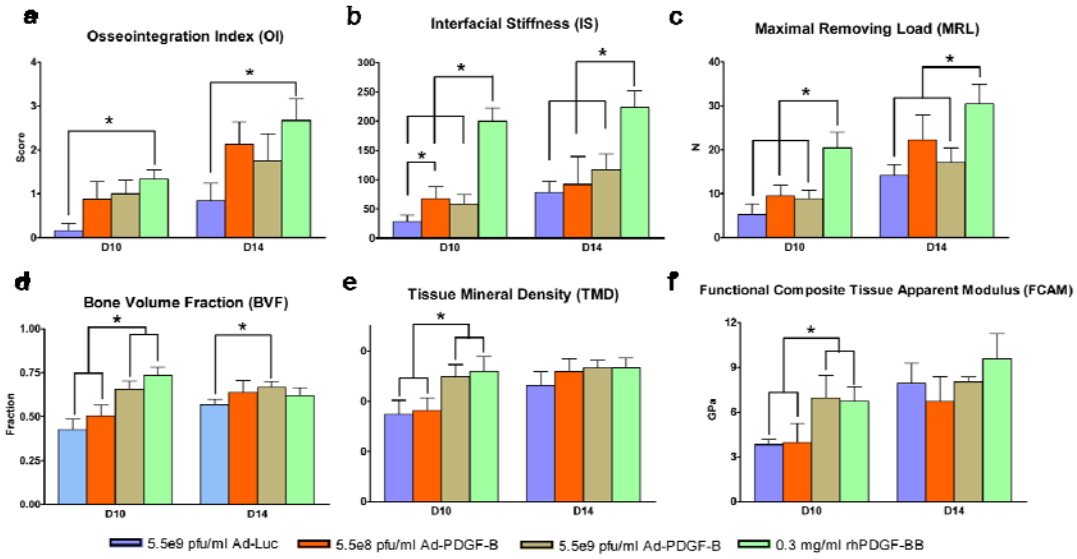

Figure 3.4 Biomechanical and microCT/functional stimulations demonstrate that Ad-PDGFB and PDGF-BB improve osseointegration *in vivo*. Osseointegration index (**a**), Interfacial stiffness (**b**), maximum removing load (**c**), showed significant differences between rhPDGF-BB treatment and the other three groups. Bone volume fractions (**d**), tissue mineral density (**e**), and functional tissue modulus (**f**) demonstrate that $5.5x10^9$ pfu/ml Ad-PDGF-B and rhPDGF-BB displayed significant differences compared to $5.5x10^8$ pfu/ml AD-PDGF-B and Ad-Luc groups. There were no significant differences in tissue mineral density and functional composite tissue apparent modulus at day 14. Data are presented as mean and bars indicate standard error measurement (n=6-8). * $p<0.05$, *Abbreviations: FCAM: functional composite tissue apparent modulus.*

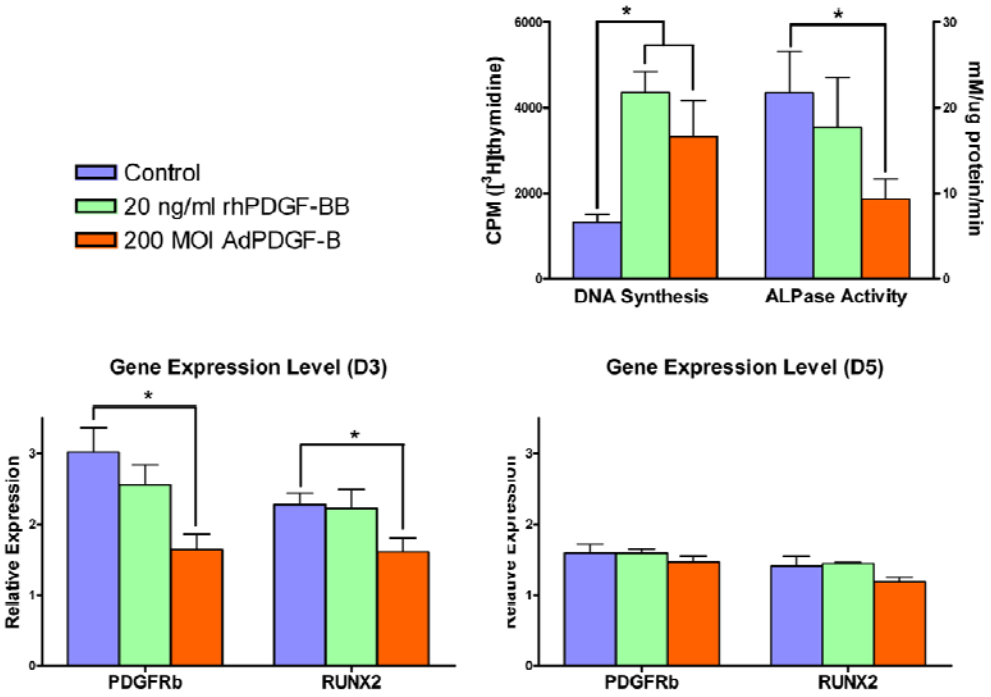

Figure 3.5 ***In vitro*** **results of rhPDGF-BB and AdPDGF-B treatment in osteogenic induction environment.** Effects of 3 hours treatment of 20 ng/ml rhPDGF-BB and 200 MOI AdPDGF-B were compared for DNA synthesis ability and ALPase activity after 5 days (**a**). The DNA synthesis was significantly increased in both the two groups and ALPase was significantly decreased in AdPDGF-B group. The gene expression level were compared after 3 and 5 days (**b**,**c**). The expression of PDGFRb and RUNX2 was still downregulated in AdPDGF-B treatment at day 3 but recovered at day 5. * $p<0.05$, *Abbreviations: CPM: counts per minute; ALPase: alkaline phosphatase; PDGFRb: platelet-derived growth factor receptor-beta; RUNX2: runt-related transcription factor 2*

3.8 References

1. Wikesjo, U.M., Sorensen, R.G. & Wozney, J.M. Augmentation of alveolar bone and dental implant osseointegration: clinical implications of studies with rhBMP-2. *J Bone Joint Surg Am* **83-A Suppl 1**, S136-45 (2001).
2. Lynch, S.E. et al. The effects of short-term application of a combination of platelet-derived and insulin-like growth factors on periodontal wound healing. *J Periodontol* **62**, 458-67 (1991).
3. Fang, J. et al. Stimulation of new bone formation by direct transfer of osteogenic plasmid genes. *Proc Natl Acad Sci U S A* **93**, 5753-8 (1996).
4. Ramseier, C.A., Abramson, Z.R., Jin, Q. & Giannobile, W.V. Gene therapeutics for periodontal regenerative medicine. *Dent Clin North Am* **50**, 245-63, ix (2006).
5. Ghosh, S.S., Gopinath, P. & Ramesh, A. Adenoviral vectors: a promising tool for gene therapy. *Appl Biochem Biotechnol* **133**, 9-29 (2006).
6. Chang, P.C. et al. Adenovirus Encoding Human Platelet-Derived Growth Factor-B Delivered to Alveolar Bone Defects Exhibits Safety and Biodistribution Profiles Favorable for Clinical Use. *Hum Gene Ther* (2009).
7. Gu, D.L. et al. Adenovirus encoding human platelet-derived growth factor-B delivered in collagen exhibits safety, biodistribution, and immunogenicity profiles favorable for clinical use. *Mol Ther* **9**, 699-711 (2004).
8. Barrientos, S., Stojadinovic, O., Golinko, M.S., Brem, H. & Tomic-Canic, M. Growth factors and cytokines in wound healing. *Wound Repair Regen* **16**, 585-601 (2008).
9. Anusaksathien, O., Jin, Q., Zhao, M., Somerman, M.J. & Giannobile, W.V. Effect of sustained gene delivery of platelet-derived growth factor or its antagonist (PDGF-1308) on tissue-engineered cementum. *J Periodontol* **75**, 429-40 (2004).
10. Canalis, E., McCarthy, T.L. & Centrella, M. Effects of platelet-derived growth factor on bone formation in vitro. *J Cell Physiol* **140**, 530-7 (1989).
11. Nevins, M. et al. Platelet-derived growth factor stimulates bone fill and rate of attachment level gain: results of a large multicenter randomized controlled trial. *J Periodontol* **76**, 2205-15 (2005).
12. Uhl, E., Rosken, F., Sirsjo, A. & Messmer, K. Influence of platelet-derived growth factor on microcirculation during normal and impaired wound healing. *Wound Repair Regen* **11**, 361-7 (2003).
13. Simion, M., Rocchietta, I., Monforte, M. & Maschera, E. Three-dimensional alveolar bone reconstruction with a combination of recombinant human platelet-derived growth factor BB and guided bone regeneration: a case report. *Int J Periodontics Restorative Dent* **28**, 239-43 (2008).
14. Jin, Q., Anusaksathien, O., Webb, S.A., Printz, M.A. & Giannobile, W.V. Engineering of tooth-supporting structures by delivery of PDGF gene therapy vectors. *Mol Ther* **9**, 519-26 (2004).
15. Traini, T., Degidi, M., Iezzi, G., Artese, L. & Piattelli, A. Comparative evaluation of the peri-implant bone tissue mineral density around unloaded titanium dental implants. *J Dent* **35**, 84-92 (2007).
16. Otsu, N. Threshold Selection Method from Gray-Level Histograms. *Ieee Transactions on Systems Man and Cybernetics* **9**, 62-66 (1979).
17. Maniatopoulos, C., Sodek, J. & Melcher, A.H. Bone formation in vitro by stromal cells obtained from bone marrow of young adult rats. *Cell Tissue Res* **254**, 317-30 (1988).

18. Chang, P.C., Seol, Y.J., Kikuchi, N., Goldstein, S.A. & Giannobile, W.V. *In vivo* FEA predicts functional oral implant osseointegration. *J Dent Res* ***in press***.
19. Gabet, Y. et al. Parathyroid hormone 1-34 enhances titanium implant anchorage in low-density trabecular bone: a correlative micro-computed tomographic and biomechanical analysis. *Bone* **39**, 276-82 (2006).
20. Ramp, L.C. & Jeffcoat, R.L. Dynamic behavior of implants as a measure of osseointegration. *Int J Oral Maxillofac Implants* **16**, 637-45 (2001).
21. Lin, Z., Sugai, J.V., Jin, Q., Chandler, L.A. & Giannobile, W.V. Platelet-derived growth factor-B gene delivery sustains gingival fibroblast signal transduction. *J Periodontal Res* **43**, 440-9 (2008).
22. De Donatis, A. et al. Proliferation versus migration in platelet-derived growth factor signaling: the key role of endocytosis. *J Biol Chem* **283**, 19948-56 (2008).
23. Hsieh, S.C. & Graves, D.T. Pulse application of platelet-derived growth factor enhances formation of a mineralizing matrix while continuous application is inhibitory. *J Cell Biochem* **69**, 169-80 (1998).
24. Tokunaga, A. et al. PDGF receptor beta is a potent regulator of mesenchymal stromal cell function. *J Bone Miner Res* **23**, 1519-28 (2008).
25. Kono, S.J. et al. Erk pathways negatively regulate matrix mineralization. *Bone* **40**, 68-74 (2007).
26. Huang, Z., Nelson, E.R., Smith, R.L. & Goodman, S.B. The sequential expression profiles of growth factors from osteoprogenitors [correction of osteroprogenitors] to osteoblasts in vitro. *Tissue Eng* **13**, 2311-20 (2007).
27. Ng, F. et al. PDGF, TGF-beta, and FGF signaling is important for differentiation and growth of mesenchymal stem cells (MSCs): transcriptional profiling can identify markers and signaling pathways important in differentiation of MSCs into adipogenic, chondrogenic, and osteogenic lineages. *Blood* **112**, 295-307 (2008).
28. Kratchmarova, I., Blagoev, B., Haack-Sorensen, M., Kassem, M. & Mann, M. Mechanism of divergent growth factor effects in mesenchymal stem cell differentiation. *Science* **308**, 1472-7 (2005).
29. Andrae, J., Gallini, R. & Betsholtz, C. Role of platelet-derived growth factors in physiology and medicine. *Genes Dev* **22**, 1276-312 (2008).
30. Tokuda, H. et al. Potentiation by platelet-derived growth factor-BB of FGF-2-stimulated VEGF release in osteoblasts. *J Bone Miner Metab* **26**, 335-41 (2008).
31. Zhang, J. et al. Differential roles of PDGFR-{alpha} and PDGFR-{beta} in angiogenesis and vessel stability. *Faseb J* ***in press***(2008).

CHAPTER 4

SAFETY PROFILE OF PLATELET-DERIVED GROWTH FACTOR TREATMENT BY ADENOVIRAL-VECTOR GENE DELIVERY ON ALVEOLAR BONE DEFECTS

4.1 Abstract

Platelet-derived growth factor (PDGF) gene therapy offers promise for tissue engineering of tooth-supporting alveolar bone defects. To date, limited information exists regarding the safety profile and systemic biodistribution of PDGF gene therapy vectors when delivered locally to periodontal osseous defects. The aim of this preclinical study was to determine the safety profile of adenovirus encoding the PDGF-B gene (AdPDGF-B) delivered in a collagen matrix to periodontal lesions. Standardized alveolar bone defects were created in rats, followed by delivery of matrix alone or containing $5.5x10^8$ or $5.5x10^9$ pfu/ml AdPDGF-B. The regenerative response was confirmed histologically. Gross clinical observations, hematology, and blood chemistries were

monitored to evaluate potential systemic involvement. Bioluminescence and QPCR were utilized for assessing vector biodistribution. Results showed that no significant histopathological changes were noted during the investigation. Minor elevation in one specific blood chemistry parameter was observed, however, all other values were within the normal range for all groups. Bioluminescence analysis revealed slight vector distribution at the axillary lymph nodes during the first 2 weeks then a subsequent return to baseline levels. AdPDGF-B was well-contained within the localized osseous defect area without viremia or distant organ involvement. These results indicate that AdPDGF-B delivered in a collagen matrix exhibits acceptable safety profiles for consideration of human clinical studies.

4.2 Introduction

Platelet-derived growth factor (PDGF) is a member of the multifunctional polypeptide family, which is composed of disulfide-bonded A, B, C, or D polypeptide chains to form a homo- or heterodimeric molecule [1]. PDGF is highly expressed in inflammatory cells, damaged bone, platelets, and mesenchymal cells [2]. PDGF mediates mitogenesis and chemotaxis of mesenchymal cells and osteoblasts through tyrosine-phosphorylated signaling pathways [3,4]. In oral tissues, PDGF also facilitates chemotaxis, matrix deposition, and attachment of periodontal ligament cells [5-7]. Delivery of PDGF-BB has also demonstrated enhancement of periodontal wound repair [8], regeneration preclinically [9] and in humans [10].

Although exogenous growth factors improve the soft and hard tissue healing response, more sophisticated delivery methods are necessary to ensure adequate protein concentration and specific cell targeting to defect sites [11]. Recombinant adenoviruses (Ads) have been utilized as gene delivery vectors due to several unique features: (1) High transduction efficiency in both dividing and non-dividing cells; (2) Ads do not induce apparent phenotypic changes in transduced cells; and (3) Ads do not integrate into the host genome and remain episomal [12-14]. Compared to recombinant growth factors,

adenovirus encoding PDGF gene sequences (AdPDGF) can successfully transduce cells, prolong growth factor expression, and induce downstream signaling pathways [15].

The use of adenoviral vectors to the head and neck for salivary gland repair have been previously studied and are now in clinical development [16,17]. Matrix-mediated delivery of DNA vectors has the potential to localize the vector and transgene products within the immediate delivery site [12]. We have previously shown that AdPDGF-B delivery in collagen significantly improves cementogenesis and osteogenesis *in vivo* [18]. A preclinical investigation using the AdPDGF-B/collagen combination in a rabbit dermal wound model revealed robust localized wound healing responses with minimal systemic vector dissemination [14].

Based on our current knowledge, no data exists describing the systemic effects of adenoviral vector delivered to the osseous craniofacial complex. In this study we sought to evaluate the safety profile for the local, collagen matrix-mediated delivery of AdPDGF-B for the promotion of alveolar bone healing. Vector copy number and expression at the defect site and various organs were quantified, and systemic hematology and blood chemistry were evaluated. In combination with histological findings, the data

in the present study further support the clinical development of matrix-enabled gene therapy for periodontal wound regeneration.

4.3 Materials and Methods

4.3.1 Adenoviral Vectors

E1-, E3-deleted human adenovirus serotype 5 vectors encoding transgenes under control of the cytomegalovirus promoter were employed in this study. Adenovirus encoding human platelet-derived growth factor-B (AdPDGF-B) and adenovirus encoding firefly luciferase (AdLuc) are utilized for gene transfer. Titers of virus stocks were determined on embryonic kidney 293 cells by plaque assay and expressed as the plaque-forming units (pfu) per milliliter. Two different doses of adenoviral vectors were examined in this study, $5.5x10^8$ pfu/ml and $5.5x10^9$ pfu/ml in 20 μl collagen matrix. These dose levels were equivalent to Ad-PDGFB concentrations previously described [18].

4.3.2 Preparation of Adenovirus-Gene Activated Matrix.

The AdPDGF-B and AdLuc were dialyzed into GTS buffer (2.5% glycerol, 25 mM NaCl, 20 mM Tris, pH 8.0) and formulated in bovine fibrillar type I collagen matrix (Matrix Pharmaceutical Inc., Fremont, CA, USA) to a final concentration of 2.6%.

4.3.3 Periodontal Alveolar Bone Wound Model and AdPDGF-B Treatment

All animal experiments were approved by the University of Michigan Institutional

Animal Care and Use Committee. A total of 144 (75 male, and 69 female) 10-week old Sprague-Dawley rats (weighing 250-300 grams) were utilized in this investigation. The general timeline, grouping criteria, and study design are shown in Figure 4.1A and total gender distributions for each experiment described separately.

Two different adenovirus-gene activated matrices were prepared immediately prior to surgery, containing 5.5 x 10^8 pfu/ml (low-dose), 5.5 x 10^9 pfu/ml (high-dose) of AdPDGF-B, and collagen matrix alone. For surgical operations, the animals were anesthetized with ketamine (50 mg/kg) and xyzaline (10 mg/kg), followed by analgesia as needed with buprenex (0.1-0.5 mg/kg, Reckitt Benckiser Healthcare Ltd., Hull, England). A standardized 3 x 2 x 1 mm osseous defect was created in the buccal plate overlying the mandibular first molar and second molar tooth roots as previously described [18]. The exposed roots were carefully denuded of periodontal ligament, cementum, and superficial dentin. Then 20μl of adenovirus/collagen matrix were delivered to the defects, filling them to entirety. The wounds were closed by suturing the superficial musculature layers and approximating the skin by surgical clips. The rats received analgesics on the following day as needed for up to 7 days post-surgery. The animals also received supplemental antibiotics (ampicillin 268 μg/L of dextrose in

distilled water) for 7 days. The surgical clips were removed 10 days following surgery. Six rats without any surgical interventions (no treatment) were also included to compare the surgical procedure to no treatment on body homeostasis.

4.3.4 Body Weight and Clinical Observations

24 male rats were equally divided into four group (high-dose AdPDGF-B, low-dose AdPDGF-B, collagen matrix only, and no treatment). The body weight of those animals was measured during the first three weeks. Clinical observation was focused on evaluation of the gross signs of swelling and lesions at days 3-35 as noted in Figure 4.1A.

4.3.5 Tissue Harvesting, Histological, and Histopathological Observations

Upon sacrifice, the submandibular lymph nodes, axillary lymph nodes, brain, lung, heart, liver, spleen, kidney, and testes from male rats, and the entire tissue within defect area as well as ovaries from female rats were harvested using sterile scissors for each of the specific tissues and organs. The instruments were sterilized between tissue harvests using a glass bead sterilizer. The ipsilateral organs were chosen, and for organs with abundant DNA (heart, lung, liver, spleen, kidney, sex organs, and brain), sectioning was done at the center of each specimen. Half of the selected tissues were then preserved in a

-80°C freezer for DNA extraction, and the remaining half were fixed with 10% formalin for 24 hours and transferred to 75% ethanol for subsequent histological and histopathological analysis. The defect mandibulae were decalcified with 10% acetic acid, 4% formaldehyde, and 0.85% NaCl for 3 weeks. Then, decalcified mandibulae and the organ specimens were dehydrated in step gradients of ethanol and embedded in paraffin. Sections from two different regions (border and central level of defect) were made in mandibular samples and 3-6 slices from the central-cut sections (5-8 μm in thickness). Hematoxylin and eosin staining was performed on all histological sections followed by pathological examination. The time points for analyses were from days 3 to 35 as described in Figure 4.1A. A thorough histopathological examination was performed for all sections.

4.3.6 Kinetics of Luciferase Expression by AdLuc/GAM in vivo.

Adenovirus encoding luciferase (AdLuc) was formulated at concentrations of 5.5 x 10^8 (low-dose, n=6, 3 per gender) and 5.5 x 10^9 pfu/ml (high-dose, n=6, 3 per gender) in 20 μl collagen matrix. The luciferase expression within each of the animals was measured using the Xenogen *In Vivo* Imaging System (Xenogen Corp., Alameda, CA, USA). To standardize the images, the cut-off threshold was set as 5,000 p/sec/cm^2/sr to reduce the

background signals, and the yield threshold was set at 13,000 p/sec/cm^2/sr. The amplitude of luciferase expression was calculated by subtracting the intensity of luciferin signal before and 12-15 minutes after luciferin (Promega Co., Madison, WI, USA) injection (4 mg luciferin/25 g body weight). The time points for evaluation are described in Figure 4.1A.

4.3.7 Hematology and Blood Chemistry.

All procedures were performed by the animal health diagnostic laboratory in the Unit for Laboratory Animal Medicine (ULAM) at the University of Michigan. 24 male rats were equally divided into four groups (high-dose AdPDGF-B, low-dose AdPDGF-B, collagen alone, and no treatment), and blood was drawn from the day prior to surgery through 35 days post-operation (Figure 4.1A). 50 μl whole blood from each rat was placed into a tube containing EDTA anticoagulant for hematological specimens and a complete blood cell count (CBC) with automatic differential was performed. 200 μl serum was drawn from each animal and the chemical parameters examined were alkaline phosphatase, calcium, phosphorus, creatinine kinase, albumin, globulin, total protein, BUN, creatinine, AST, ALT, bilirubin, T. bilirubin, amylase, glucose, and cholesterol.

4.3.8 Quantitative PCR (QPCR) Assay

Quantitative TaqMan PCR was used to determine the vector copy number of AdPDGF-B in the bloodstream and organs. The primers used for quantitative real time PCR (QPCR) bridging the vector backbone and PDGF-BB prepro region were: sense --5'-GGATCTTCGAGTCGACAAGCTT-3'; anti-sense --5'-ATCTCATAAAGCTCCTCGGGAAT-3'; internal fluorogenic probe --5'-CGCCCAGCAGCGATTCATGGTGAT-3'. QPCR was performed by using TaqMan Universal PCR Master Mix (Applied Biosystems). Briefly, a 30 μl PCR reaction was prepared with 500 ng DNA and 1.5μl mixture of gene fluorogenic probe and primers. The thermal conditions were: 50°C 2 min, 95°C 10 min followed by 45 cycles of 95°C, 15 sec and 60°C, 1 min, and the resulting amplicon was detected by ABI Prism 7700 sequence detection instrument (Applied Biosystems). The standard curve was determined by using a range of 10^1 to 10^5 AdPDGF-B particles (regression correlation coefficient > 95%). The possibility of cross-reactivity was evaluated by adding adenoviral vector encoding PDGF-A, PDGF-1308 (dominant-negative mutant PDGF), bone morphogenetic protein-7, noggin, bone sialoprotein, Luciferase, and GFP for comparison. No enhancement or inhibition of signal was noted when tissues were spiked with these vectors.

For blood DNA, the samples were collected from 6 rats per gender (total of 12 per group) in the four groups (high-dose AdPDGF-B, low-dose AdPDGF-B, collagen matrix only, and no treatment) prior to surgery, and throughout 35 days after gene delivery (Figure 1A). 50 μl whole blood was isolated and DNA was obtained by QIAamp DNA blood Mini kit (QIAGEN Inc., Valencia, CA, USA). For organ and tissue DNA, the total tissue in the defect area and surrounding musculature, submandibular lymph node, axillary lymph nodes, brain, lung, heart, liver, kidney, spleen, and sex organs (testes and ovaries) were excised from 3 rats in each of the three groups (high-dose AdPDGF-B, low-dose AdPDGF-B, and collagen matrix only) post-sacrifice, and triplicate experiments were performed. The time points analyzed were from 3 to 35 days (Figure 4.1A). Each PCR reaction contained 500 ng test DNA without spiking. Pre-study experiments demonstrated expected signal enhancement using AdPDGF-B spiking (500 copies per reaction, *data not shown*). The limitation of detection was 30 copies per 500 ng test DNA for all the specimens.

4.3.9 Statistical Analysis

ANOVA was utilized to evaluate the differences of body weights, hematological and chemical parameters between experimental and control groups. The test groups were

evaluated for time-dependent dynamics with collagen and non-surgical groups using Bonferroni post-tests, and the significance was assessed by repeated-measures ANOVA. The results are presented as the mean ± SD of measurements, with a p value of less than 0.05 being considered statistically significant.

4.4 Results

4.4.1 Clinical Observations and Body Weight

All animals survived throughout the entire experimental period and among all surgically-treated animals, no significant adverse events were noted beyond local swelling at the treatment sites, presumably due to the surgical procedures. Body weight changes were normalized using day 0 as baseline, and the measures of weight change were evaluated as fractions relative to baseline weight. Results showed that following surgical treatment, all animals suffered slight weight loss within the first 2 days, however, they consistently gained weight over the course of the study. No significant weight changes were found among the three surgical groups at all time points (Figure 4.1B).

4.4.2 Histology and Histopathology

At 2 weeks following surgery, early bone formation could be observed within the defect area (Figure 4.2A, upper panels). Nearly complete bone bridging of the alveolar bone wounds was noted in both AdPDGF-B treated groups, whereas there was limited bridging in the collagen only animals. Cementogenesis could be seen in both AdPDGF-B-treated groups at 2 weeks but not in the collagen matrix group, and the defects treated with high-dose [$5.5x10^9$ pfu/ml] AdPDGF-B revealed more cementum

formation compared to other groups (Figure 4.2A, lower panels). At 35 days, the bone had completely bridged all of the defects area, and the fractions of defect fill became consistent in all animals. Animals receiving high-dose Ad-PDGFB demonstrated greater evidence for cementogenesis along the tooth root (Figure 4.2B).

Macroscopic evaluations of the harvested organs revealed no meaningful changes except mild enlargement of submandibular lymph nodes in AdPDGF-B treated (both high-dose and low-dose) and collagen matrix only groups within the first week post-surgery. Evaluation of histological sections showed occasional but mild inflammatory infiltration in lymph nodes, spleen, and liver in all groups. However, no significant histopathological signs were noted beyond the suspected alterations associated with the surgical operation. In particular, no evidence of viral inclusions was observed for any of the evaluated tissues and organs.

4.4.3 Hematology and Blood Chemistry

Blood was analyzed from each animal prior to surgery through 35 days post-operation (Figure 4.1A). Also, blood from six animals in the no treatment group was collected for comparison. All parameters for hematology and blood chemistry were

consistent among groups and were generally within the normal range. Although there were some minor changes, we found no significant differences in complete blood count (CBC) and clinical chemistry parameters among all treatment groups throughout the period of observation (Tables 4.1 and 4.2). There were several animals in both the high-dose and low-dose groups that revealed significant changes in amylase, however the majority of the values were within the normal range. At day 28, the animals in the low-dose group demonstrated significant elevation in their serum glucose, but those levels returned to baseline range by day 35.

4.4.4 Vector Expression by Bioluminescence

Whole body image analysis of animals treated with AdLuc/collagen matrix revealed a transduction and distribution profile from adenoviral gene delivery over the course of the experiment. The bioluminescent luciferase expression was detected in the head and neck region for all AdLuc/collagen-treated animals (n=6 per group), with the level of expression higher in animals receiving high-dose AdLuc compared with the low dose animals (Figure 4.3A). For the low-dose AdLuc-treated group, the luciferase expression gradually decreased to undetectable levels at the treated sites by 14 days without any spreading to distant organs for time points thereafter (Note in Figure 4.3A whole body

imaging, upper panel shows some luminescence on Day 28 (animal's right side)). Results also showed a gradually decreasing expression of luciferase in the head and neck region within 2 weeks in the high-dose AdLuc-treated animals. Further, the high-dose treated animals yielded a weak signal detected in the axillary lymph node area of 3 animals, and one animal showed liver expression at one week. However after 2 weeks, no signal was detected in any distant organs of any animal (Figure 4.3B). To further investigate the persistent, low-level expression of AdLuc signal in two high-dose treated animals, bioluminescent imaging was performed until sacrifice at 75 days post-treatment. The defect mandible, surrounding musculature, axillary lymph nodes, liver, and gonadal organs were harvested and images were captured for bioluminescent quantification. The results revealed that a very weak signal was restricted to only the surrounding musculature (<10 p/sec/mm^2/sr), and no signal was detected in the defect site (*data not shown*). Additionally, no significant gender differences in AdLuc expression were revealed however, a somewhat lower signal was noted at day 1 in the head and neck region of female rats receiving high-dose AdLuc treatment ($p<0.05$, data not shown).

4.4.5 Biodistribution by Quantitative PCR

The specificity of our PCR primers and the sensitivity of the assay were determined

prior to analysis of the study samples. We measured no primer cross-reaction with adenovirus encoding bone sialoprotein, bone morphogenetic protein-7, luciferase, noggin, PDGF-A, PDGF-1308, or GFP (data not shown). The sensitivity and detection limit of our PCR assays was 30 virus copies per 500 ng DNA. Within the AdPDGF-B treated area, viral vector could be detected within the first week in DNA from both high-dose and low-dose treated animals. The number of vector copies gradually decreased to undetectable levels after two weeks (Table 4.3). Vector copies measured in the blood were below the detection limit for all animals over the total period of observation. The PCR assay measured a very low level of vector within spleen DNA of one animal at 3 days post-treatment, and within lung of another animal at 2 weeks post-treatment, however no significant vector DNA was detected in organs or tissues from the treatment groups for the remainder of the experimental time points (Table 4.3). These values were below the detection limit and compared similarly to vector values at the defect site, which were low-to below detection level. Upon examination of histological sections from the tissues (spleen and lung) positive for AdPDGF-B DNA, we found no inflammation-related phenotype or other pathological findings when compared to tissue sections from collagen matrix-treated animals.

4.5 Discussion

PDGF-BB protein has demonstrated its strong potential for soft and hard tissue repair and is available for clinical use [10,13,19]. However, due to the high degradation rate and transient persistence *in vivo*, the treatment outcome is not entirely predictable for clinical applications [20]. Gene delivery utilizing an adenoviral vector provides sustained and stable transduction efficiency *in vitro* [15]. These data confirm and extend on those of Jin et al [18] demonstrating significant enhancement of tooth-supporting alveolar bone and cementum regeneration *in vivo* using gene-activated matrices containing Ad-PDGFB.

While a number of studies focus on the safety profile of adenoviral-mediated gene therapy, few of them have addressed the local delivery of vectors using a gene activated matrix and none related to the periodontium or localized bone defects. Studies have shown that direct systemic administration of adenoviral vectors can result in acute toxicity and hepatic pathology [21-23] . Systemic dissemination can be reduced and the efficacy/toxicity ratio can be improved by local gene delivery [24]. With localized delivery, the vector likely enters the systemic circulation via the leaky microvessels and systemically disseminates within 10 minutes [24], with the inflammatory infiltrate within liver observed after 15 minutes in mice [21]. In this study, we employed matrix

(collagen)-enabled gene delivery for localized administration to alveolar bone defects. The vector dissemination in our animals beyond the alveolar bone area was limited, demonstrating a well-contained localization of the gene activated matrix.

Studies have shown that nearly 99% of systemically-delivered adenoviral vectors will eventually accumulate in the liver, and are rapidly taken up by Kupffer cells and hepatocytes [25,26]. The Kupffer cells might distribute to the lung and spleen via circulation, but in this study we did not detect any significant vector quantities in those organs. No significant elevation of the enzymes specific in those organs further demonstrates a limited systemic influence due to this approach. Although transgene luciferase expression was found in the axillary lymph nodes, spleen, and lung of a few adenoviral vector-treated animals at 2 weeks post-administration (with no expression in these organs at later time points), the level was only slightly greater than background and no accompanying toxicological signs or histopathological changes were found. We also noted no treatment-related toxicity throughout the 35 day period. The majority of the hematological and clinical chemistry parameters were within normal ranges and the only significant difference was noted for amylase, and is derived primarily from the pancreas, parotid gland, and some from the liver, which is one of the major enzymes to digest

starch into a simple sugars. Changes in serum amylase may represent a normal physiologic process, acute or chronic pancreatitis, or concomitance of ongoing diseases [27]. Moreover, lipase is a more sensitive and specific marker to diagnose pancreatitis [28], and the lipase level in all animals did not change significantly. However, it is highly possible that the amylase came from the parotid salivary gland that was located in very close proximity to the surgical field. The parotid gland in rats is non-encapsulated as compared to the gland in humans. We cannot rule-out this area at early time points. At later time points when we measured the luciferase signal from the harvested organs, no detectable signal was found in any of the parotid glands, but mainly in the surrounding musculature (Figure 4.3). *In vivo* bioluminescence generated by expression of the luciferase transgene permitted quantification and localization of transgene expression and provided a non-invasive, dynamic, and comprehensive monitoring of vector expression at the whole body level [29,30]. As little as 10^4 luciferase-expressing recombinant adenoviruses are capable of producing luminescence in the liver [31], which is significantly higher in sensitivity than possible with QPCR [30], making bioluminescence a more sensitive evaluation of biodistribution and subsequent vector activity. In the early time periods we detected vector in the defect area of adenovirus-treated animals, which reached undetectable levels by day 14. This result is supportive of those reported by Jin et al [18],

which showed the luciferase signal decreased to 20% by day 14 and reached an undetectable level by day 28 compared with the expression at day 1. Moreover, given that PDGF is expressed *in vivo* over about 10 days in periodontal wounds following injury [32], this gene therapy approach demonstrates a similar expression profile that may be favorable for therapeutic application.

Another potential concern regarding viral vectors is the host immunity, including innate and adaptive immune responses [33]. In terms of adaptive immune response, the adenoviral antigens activated the cytotoxic T lymphocytes (CTL) to destroy the transduced cells, and the humoral virus-neturalizing antibody reduced transduction efficiency and promoted macrophage opsonization [34]. The innate immunity is characterized by temporary production of cytokines/chemokines, causing local or systemic inflammation [33]. We did not find any significant inflammation at the vector delivery site in our animals, and acceleration of osseous defect repair, accompanied with obvious vector signal expression during the first two weeks, implied that the vectors did not exhibit significant local immunity. Non-detectable levels of vector dissemination resulted in minimal vector distribution in the distant organs, especially spleen, lung, and liver, which are the major sites of inflammatory cytokine production [35]. Since we found

no significant alteration of hematological or clinical chemistry parameters, we conclude that the dose regimen is appropriate for treatment of periodontal osseous defect without causing significant local and systemic immune responses.

On the other hand, a delayed but persistent humoral response to adenovirus has been reported in several preclinical and clinical investigations [36,37], and this response represents the major obstacle for readministration, as the generation of neutralizing antibodies reduces the transduction efficiency on the host cells [23,38]. Thus, a temporary blockade of the immune response may be necessary for allowing vector readministration. Immunoregluation from the coadministration of IFN-γ, IL-12, adenoviral proteins, inhibition of cytokine lymphotoxin-α, or inhibition of antigen-presenting T cell costimulation, has demonstrated its ability to achieve favorable transduction efficiency from repeated vector applications [39-42]. Sequential application of Ad with an alternative serotype may also prevent the effects from the neutralizing antibodies [43]. However, the local and systemic alterations from immunomodulation, as well as the dose regimen for repeated Ad application, must still be carefully evaluated.

4.6 Safety Profile to Oral Implant Osseous Wounds

According to Chapter 3, the efficacy of AdPDGF-B in promoting osseointegration has been proven. While the safety profile of AdPDGF-B delivery to a mandibular periodontal osseous defect was determined in earlier sections within this chapter, we planned a series of experiments to investigate the preclinical safety profile of the peri-implant osseous defect on maxillae.

A total of 18 male Sprague-Dawley rats were utilized in this part of study, and the general timeline and examinations are listed in Figure 4.4. The surgical and implantation procedures followed the procedures described in section 3.3.5, where a 0.6x1 mm circumferential osseous defect was created surrounding the 1x2 mm cylinder oral titanium implant on bilateral maxillae and filled with collagen matrix alone (control) or matrix containing $5.5x10^8$ or $5.5x10^9$ pfu/ml AdPDGF-B. Blood was drawn from all animals prior to implantation (baseline) and through 1-35 days post-implantation. Vector dissemination was examined using qPCR (as described in section 4.3.8) from blood DNA extracted at baseline, days 1, 2, 3, 4, 5, 6, 7, 14, 21, 28, and 35 (Figure 4.4). The hematological and clinical chemical parameters were evaluated as described in section 4.3.7 at baseline, day 3, 7, 14, 21, 28, and 35 days (Figure 4.4). The clinical symptoms

and signs were also observed over the period of 35 days post-implantation.

Results demonstrated a mild, localized swelling that subsided after day 3 in both control and AdPDGF-B treated animals. All animals survived through the end of study without displaying any significant clinical symptoms . The level of vector replicates in all the AdPDGF-B treated animals was below the detection limit, indicating no significant vector dissemination within the 5 weeks (Table 4.4). The majority of hematological and clinical chemistry parameters were within the normal range and none of them demonstrated any significant difference between adenoviral or non-adenoviral treatment (Table 4.5-6). Based on these results, we conclude that AdPDGF-B demonstrated preclinical acceptable safety profile on delivery to the maxillary peri-implant osseous wounds.

4.7 Conclusion

The results from our experiments demonstrate that local administration of AdPDGF-B with gene activated matrix is safe when delivered to tooth-supporting alveolar bone defects. No treatment-related toxicity or systemic involvement was found. Although vector particle DNA was detectable during the first two weeks primarily in the osseous defects, the titer was very low and quickly attenuated at subsequent time points. These results support the further clinical development of AdPDGF-B for regeneration therapy for oral and craniofacial bone application.

4.8 Tables

Table 4.1. Hematological Analyses for AdPDGF-B Delivery in Periodontal Osseous Defects *

Hematological Parameters	Prior to surgery			Day 3			Day 7			Day 14		
	Col	L-Ad	H-Ad	Col	L-Ad	H-Ad	Col	L-Ad	H-Ad	Col	L-Ad	H-Ad
WBC (K/µl)	12.53 (1.84)	12.87 (2.21)	13.99 (2.98)	13.08 (1.98)	8.491 (1.428)	16.27 (2.29)	12.57 (4.75)	12.07 (3.97)	16.90 (2.19)	16.07 (3.15)	13.01 (2.79)	14.64 (0.86)
Neutrophil (K/µl)	3.081 (0.887)	4.184 (0.910)	4.534 (1.343)	3.493 (0.665)	2.448 (0.559)	4.985 (0.660)	4.365 (2.170)	2.781 (1.032)	6.019 (0.678)	6.599 (2.293)	4.134 (1.228)	4.811 (0.663)
Lymphocyte (K/µl)	8.641 (1.481)	7.908 (1.593)	8.753 (1.595)	8.784 (1.449)	5.484 (0.949)	10.16 (1.259)	7.455 (2.674)	8.491 (2.754)	9.651 (1.673)	8.683 (1.870)	8.025 (1.575)	8.974 (0.500)
Monocyte (K/µl)	0.765 (0.239)	0.745 (0.166)	0.604 (0.180)	0.735 (0.220)	0.516 (0.175)	0.841 (0.169)	0.558 (0.299)	0.764 (0.312)	1.141 (0.182)	0.687 (0.079)	0.694 (0.174)	0.711 (0.112)
Eosinophil (K/µl)	0.033 (0.023)	0.021 (0.015)	0.074 (0.048)	0.056 (0.048)	0.043 (0.029)	0.134 (0.075)	0.158 (0.119)	0.029 (0.016)	0.05 (0.043)	0.073 (0.079)	0.133 (0.063)	0.083 (0.096)
Basophil (K/µl)	0.005 (0.008)	0.009 (0.010)	0.024 (0.035)	0.008 (0.010)	0.003 (0.005)	0.026 (0.036)	0.043 (0.041)	0.009 (0.008)	0.03 (0.044)	0.027 (0.048)	0.026 (0.031)	0.016 (0.038)
RBC (M/µl)	7.273 (0.599)	8.164 (0.488)	6.88 (0.646)	7.745 (1.210)	6.709 (0.506)	6.223 (0.426)	5.716 (1.068)	7.606 (1.213)	7.344 (0.600)	6.763 (0.481)	7.043 (0.344)	7.344 (0.224)
Hb (g/dl)	14.91 (0.78)	17.35 (1.72)	13.94 (1.42)	15.25 (2.56)	13.29 (1.10)	12.58 (0.97)	11.35 (2.29)	15.38 (1.95)	15.58 (1.09)	13.51 (0.69)	14.45 (0.60)	15.038 (0.532)
Hct (%)	44.91 (4.53)	51.24 (2.98)	41.76 (4.09)	47.2 (7.67)	40.43 (2.88)	37.64 (2.31)	33.5 (6.37)	44.66 (6.58)	44.74 (5.69)	40.54 (3.40)	41.75 (1.46)	43.89 (1.18)
MCV (fl)	61.7 (1.86)	62.79 (1.20)	60.67 (1.37)	60.9 (1.53)	60.31 (1.74)	60.54 (0.73)	58.52 (1.14)	58.85 (1.37)	62.85 (1.13)	59.89 (1.80)	59.36 (1.20)	59.79 (1.18)
MCH (pg)	20.55 (0.99)	21.24 (1.04)	20.27 (0.76)	19.69 (0.81)	19.8 (0.37)	20.19 (0.30)	19.77 (0.58)	20.33 (1.27)	21.23 (0.47)	20.01 (0.98)	20.54 (1.09)	20.48 (0.34)
MCHC (g/dl)	33.33 (1.75)	33.81 (1.81)	33.39 (0.84)	32.28 (0.75)	32.86 (1.06)	33.4 (0.71)	33.82 (1.09)	34.55 (1.61)	34.03 (1.03)	33.47 (1.59)	34.65 (1.56)	34.288 (0.954)
RDW (%)	15.44 (0.55)	16.2 (0.52)	15.01 (0.32)	16.01 (0.63)	15.76 (0.61)	15.88 (0.46)	15.92 (0.50)	17.65 (0.76)	16.89 (0.67)	16.39 (0,98)	16.29 (0.42)	16.63 (0.37)

n=6/group. The number in this table demonstrates the average value of parameters from the each group and the number in the parentheses refers to the standard deviations. No significant differences were noted among the AdPDGF-B and collagen matix groups during early time points, as well as beyond 14 days (data not shown). *Abbreviations used: Col:collagen matrix only group, L-Ad: $5.5x10^8$ pfu/ml AdPDGF-B treated group, H-Ad: $5.5x10^9$ pfu/ml AdPDGF-B treated group; WBC: white blood cells; RBC: red blood cells; Hb: hemoglobin; Hct: hematocrit; MCV: mean corpuscular volume; MCH: mean corpuscular hemoglobin; MCHC: mean corpuscular hemoglobin concentration; RDW: red blood cell distribution width*

Table 4.2. Clinical Chemistry Analyses For Ad-PDGF-B Delivery in Periodontal Osseous Defects *

Clinical Chemistry Parameters	Prior to surgery			Day 3			Day 7			Day 14		
	Col	L-Ad	H-Ad	Col	L-Ad	H-Ad	Col	L-Ad	H-Ad	Col	L-Ad	H-Ad
Albumin (g/dl)	2.814 (0.135)	2.763 (0.130)	2.657 (0.181)	2.65 (0.648)	2.657 (0.172)	2.825 (0.116)	2.543 (0.113)	2.95 (0.141)	2.788 (0.181)	2.786 (0.177)	2.913 (0.125)	3.133 (0.234)
ALPase (U/l)	260.43 (23.52)	255 (53.18)	239 (31.09)	185.5 (59.34)	238.43 (35.45)	166.63 (29.61)	200.86 (37.66)	205.75 (58.94)	153.38 (27.69)	232.29 (29.19)	232.63 (42.45)	251.67 (43.48)
ALT (U/l)	67.14 (8.30)	89 (8.45)	87.25 (7.50)	72.88 (8.92)	79.86 (4.06)	79.88 (8.15)	100.57 (10.47)	79.38 (9.96)	81 (5.04)	84.86 (5.05)	86.5 (7.58)	79.5 (19.99)
Amylase (U/l)	1881.14 (186.95)	1831 (188.36)	1554.17 (267.61)	1905.38 (388.61)	1857.43 (544.49)	1770 (251.95)	2494.86[#] (844.40)	1705.75 (310.88)	1785.13 (328.22)	1990.71 (525.58)	1879.38 (195.60)	2085.33 (44.004)
AST (U/l)	71.86 (9.91)	79.38 (9.32)	79.88 (8.97)	69.5 (20.76)	83.5 (16.55)	69.88 (5.19)	126.14 (111.67)	77.57 (13.23)	70.5 (11.43)	66.43 (11.77)	90.5 (26.46)	93.25 (16.34)
Bilirubin (mg/dl)	20.14 (3.34)	19.5 (3.70)	19 (2.16)	21.25 (2.49)	20 (2)	22.13 (2.59)	24.86 (1.86)	21.38 (2.39)	19.13 (1.64)	22.57 (1.62)	23.75 (3.45)	24.17 (1.33)
Calcium (mg/dl)	10.11 (0.25)	10.29 (0.19)	10.16 (0.28)	10.54 (1.30)	10.23 (0.28)	10.49 (0.15)	10.41 (0.25)	10.35 (0.23)	10.35 (0.12)	10.86 (0.24)	10.28 (0.18)	10.83 (0.23)
Cholesterol (mg/dl)	83.29 (7.13)	78 (9.20)	63.86 (11.81)	78.71 (29.37)	80.29 (8.16)	90 (7.01)	80 (6.90)	80.38 (7.03)	81.13 (2.80)	84.43 (10.88)	77.38 (10.32)	82.33 (5.86)
Creatine Kinase (U/l)	166.67 (28.25)	190.63 (51.90)	176.86 (47.36)	178.5 (70.13)	259.83 (133.13)	142.63 (33.18)	156.20 (38.46)	244.57 (106.69)	219.38 (64.16)	121.71 (28.96)	186.88 (61.42)	197.75 (61.41)
Creatinine (mg/dl)	0.4 (0.058)	0.35 (0.053)	0.329 (0.049)	0.363 (0.052)	0.386 (0.038)	0.4 (0)	0.386 (0.038)	0.388 (0.035)	0.3 (0.053)	0.4 (0)	0.388 (0.035)	0.629 (0.399)
Glucose (mg/dl)	230.43 (18.39)	227.88 (27.22)	229 (35.77)	217.65 (24.22)	221.57 (19.15)	191 (33.815)	245.29 (53.94)	232 (29.99)	229.88 (30.19)	192.14 (7.67)	212.5 (39.75)	200.4 (10.69)
Phosphorus (mg/dl)	7.657 (0.660)	7.4 (0.490)	6.743 (0.395)	7.225 (0.585)	6.214 (0.157)	6.663 (0.434)	6.671 (0.340)	7.65 (0.537)	7.45 (0.407)	5.9 (2.62)	7.325 (0.486)	6.833 (0.115)
T. Bilirubin (mg/dl)	0.1 (0)	0.1 (0)	0.1 (0)	0.275 (0.456)	0.114 (0.038)	0.113 (0.035)	0.1 (0)	0.175 (0.139)	0.213 (0.210)	0.1 (0)	0.113 (0.035)	0.1 (0)
Total Protein (g/dl)	5.629 (0.325)	5.625 (0.205)	5.557 (0.276)	5.95 (0.680)	5.529 (0.250)	5.925 (0.128)	5.586 (0.219)	5.863 (0.250)	5.8 (0.278)	5.943 (0.190)	5.938 (0.262)	6.443 (0.351)
Globulin (g/dl)	2.814 (0.227)	2.838 (0.106)	2.886 (0.107)	3.288 (1.272)	2.957 (0.162)	3.1 (0.093)	3.043 (0.151)	2.925 (0.128)	3.025 (0.128)	3.157 (0.140)	3.013 (0.146)	3.25 (0.152)

* All comparisons to collagen matrix group. [#] Significant difference to collagen matrix group ($p<0.05$; n=6/group). The number in this table demonstrates the mean value of parameters from each group and the number in the parentheses refers to the standard deviations. The serum amylase of both AdPDGF-B treated groups revealed significant differences with respect to the collagen matrix group and was within the normal range for time points beyond 14 days. *Abbreviations used: Col: collagen matrix only group, L-Ad: $5.5x10^8$ pfu/ml AdPDGF-B treated group, H-Ad: $5.5x10^9$ pfu/ml AdPDGF-B treated group; ALPase: alkaline phosphatase; ALT: alanine transaminase; AST: aspartate transaminase; T. Bilirubin: total bilirubin*

TABLE 4.3. AdPDGF-B PCR Results in Bloodstream and Distant Organs in Periodontal Osseous Defect Model

Organ/Tissue	Treatment	No Treatment	D3	D7	D14	D21	D28	D35
Whole tissue from osseous defect	Collagen matrix	N	N	N	N	N	N	N
	$5.5x10^8$ pfu/ml AdPDGF-B	N	3/3 (301)	2/3 (137)	1/3 (84)	N	N	N
	$5.5x10^9$ pfu/ml AdPDGF-B	N	3/3 (45,930)	3/3 (6,097)	N	N	N	N
Blood	Collagen matrix	N	N	N	N	N	N	N
	$5.5x10^8$ pfu/ml AdPDGF-B	N	N	N	N	N	N	N
	$5.5x10^9$ pfu/ml AdPDGF-B	N	N	N	N	N	N	N
Lung	Collagen matrix	N	N	N	N	N	N	N
	$5.5x10^8$ pfu/ml AdPDGF-B	N	N	N	1/3 (38)	N	N	N
	$5.5x10^9$ pfu/ml AdPDGF-B	N	N	N	N	N	N	N
Spleen	Collagen matrix	N	N	N	N	N	N	N
	$5.5x10^8$ pfu/ml AdPDGF-B	N	1/3 (31)	N	N	N	N	N
	$5.5x10^9$ pfu/ml AdPDGF-B	N	N	N	N	N	N	N
Brain, SLN, ALN, heart, liver, kidney, sex organs (testes or ovaries)	Collagen matrix	N	N	N	N	N	N	N
	$5.5x10^8$ pfu/ml AdPDGF-B	N	N	N	N	N	N	N
	$5.5x10^9$ pfu/ml AdPDGF-B	N	N	N	N	N	N	N

Abbreviations used: SLN: submandibular lymph nodes; ALN: axillary lymph nodes.

The n value is 3 per group for organ analyses and 12 per group for blood analyses. Test sample DNAs yielding signals below the limit of detection (< 30 vector particles / 500 ng DNA) are reported as "negative" (N). The number in this table demonstrates the "positive" animals in each group and the number in the parentheses refers to the mean vector copy number per 500 ng DNA from the positive animals.

Table 4.4 Vector Dissemination from Delivering AdPDGF-B in Oral Implant Osseous Wounds

	Collagen matrix alone	$5.5x10^8$ pfu/ml AdPDGF-B	$5.5x10^9$ pfu/ml AdPDGF-B
Baseline	Negative	Negative	Negative
Day 1	Negative	Negative	Negative
Day 2	Negative	Negative	Negative
Day 3	Negative	Negative	Negative
Day 4	Negative	Negative	Negative
Day 5	Negative	Negative	Negative
Day 6	Negative	Negative	Negative
Day 7	Negative	Negative	Negative
Day 14	Negative	Negative	Negative
Day 21	Negative	Negative	Negative
Day 28	Negative	Negative	Negative
Day 35	Negative	Negative	Negative

The n value is 6 per group. Test sample DNAs yielding signals below the limit of detection (< 30 vector particles / 500 ng DNA) are reported as “Negative”. The primer had no cross-reaction with adenovirus encoding bone sialoprotein, bone morphogenetic protein-7, luciferase, noggin, PDGF-A, PDGF-1308, or GFP

Table 4.5 Hematological Analyses for AdPDGF-B Delivery in Oral Implant Osseous Wounds

Hematological Parameters	Prior to surgery			Day3			Day 7			Day 14		
	Col	L-Ad	H-Ad	Col	L-Ad	H-Ad	Col	L-Ad	H-Ad	Col	L-Ad	H-Ad
WBC (K/μl)	11.87 (2.99)	10.55 (1.58)	12.15 (2.69)	9.67 (2.82)	11.04 (1.49)	11.81 (1.67)	14.70 (5.22)	11.97 (4.44)	12.15 (2.78)	10.90 (3.98)	11.36 (3.02)	12.23 (3.25)
Neutrophil (K/μl)	2.988 (0.909)	2.462 (0.914)	3.512 (0.995)	2.807 (1.161)	4.542 (1.397)	3.323 (0.778)	4.438 (1.994)	4.340 (2.913)	3.887 (0.878)	3.343 (1.600)	4.547 (2.489)	3.527 (1.272)
Lymphocyte (K/μl)	8.160 (1.355)	7.487 (0.699)	7.840 (1.511)	6.452 (2.962)	5.943 (0.918)	7.768 (1.391)	9.400 (3.051)	6.905 (1.234)	7.658 (2.086)	6.933 (2.103)	6.162 (0.785)	7.988 (1.845)
Monocyte (K/μl)	0.635 (0.311)	0.560 (0.139)	0.550 (0.179)	0.305 (0.091)	0.488 (0.128)	0.648 (0.147)	0.643 (0.299)	0.707 (0.128)	0.493 (0.307)	0.537 (0.307)	0.593 (0.227)	0.540 (0.147)
Eosinophil (K/μl)	0.073 (0.039)	0.048 (0.019)	0.190 (0.158)	0.100 (0.082)	0.058 (0.034)	0.057 (0.028)	0.165 (0.128)	0.157 (0.224)	0.102 (0.122)	0.085 (0.060)	0.048 (0.018)	0.160 (0.118)
Basophil (K/μl)	0.007 (0.012)	0.003 (0.005)	0.052 (0.064)	0.015 (0.023)	0.015 (0.023)	0.007 (0.010)	0.055 (0.053)	0.035 (0.067)	0.002 (0.004)	0 (0)	0.007 (0.010)	0.013 (0.014)
RBC (M/μl)	8.713 (0.305)	8.315 (0.405)	7.388 (0.783)	8.033 (0.585)	8.300 (0.893)	8.082 (0.449)	7.558 (0.493)	7.502 (0.329)	7.925 (0.344)	7.277 (1.257)	7.933 (0.701)	7.963 (0.492)
Hb (g/dl)	16.03 (0.56)	15.53 (0.40)	15.20 (0.64)	15.05 (0.62)	15.13 (1.72)	14.63 (0.78)	13.85 (1.07)	13.65 (0.46)	14.38 (0.58)	14.37 (1.86)	15.68 (1.42)	14.67 (0.23)
Hct (%)	51.68 (2.22)	48.27 (2.76)	42.97 (4.51)	47.50 (3.68)	48.033 (4.88)	47.88 (2.31)	45.02 (3.14)	43.60 (1.71)	47.32 (1.88)	43.95 (8.27)	46.77 (4.35)	48.23 (2.15)
MCV (fl)	59.33 (2.25)	58.07 (1.47)	58.18 (1.64)	59.13 (2.29)	57.90 (1.56)	59.30 (1.43)	59.58 (2.23)	58.20 (0.85)	59.72 (1.59)	60.25 (2.48)	58.97 (2.05)	60.65 (1.72)
MCH (pg)	18.42 (0.74)	18.70 (0.87)	20.77 (2.30)	18.78 (0.89)	18.27 (1.15)	18.13 (0.64)	18.33 (1.14)	18.23 (0.74)	18.13 (0.55)	19.92 (1.40)	19.77 (0.38)	18.47 (1.18)
MCHC (g/dl)	31.05 (0.94)	32.25 (1.59)	35.68 (3.79)	31.75 (1.47)	31.52 (1.64)	30.53 (0.55)	30.77 (1.07)	31.30 (1.07)	30.40 (0.26)	33.12 (2.95)	33.55 (0.81)	30.47 (1.49)
RDW (%)	14.05 (0.42)	13.97 (0.53)	14.10 (0.57)	14.23 (0.49)	14.25 (0.72)	14.10 (0.64)	15.27 (0.72)	15.05 (0.88)	14.50 (0.59)	15.90 (0.43)	15.77 (0.55)	15.55 (0.38)

* All comparisons to collagen group. n=6/group. The number in this table demonstrates the average value of parameters from the each group and the number in the parentheses refers to the standard deviations. No significant differences were noted among the AdPDGF-B and collagen matrix groups during early time points, as well as beyond 14 days (data not shown). *Abbreviations used: Col:collagen matrix only group, L-Ad: $5.5x10^8$ PFU/ml AdPDGF-B treated group, H-Ad: $5.5x10^9$ PFU/ml AdPDGF-B treated group; WBC: white blood cells; RBC: red blood cells; Hb: hemoglobin; Hct: hematocrit; MCV: mean corpuscular volume; MCH: mean corpuscular hemoglobin; MCHC: mean corpuscular hemoglobin concentration; RDW: red blood cell distribution width*

Table 4.6 Clinical Chemical Analyses for AdPDGF-B Delivery in Oral Implant Osseous Wounds

Clinical Chemical Parameters	Prior to surgery			Day3			Day 7			Day 14		
	Col	L-Ad	H-Ad	Col	L-Ad	H-Ad	Col	L-Ad	H-Ad	Col	L-Ad	H-Ad
Albumin (g/dl)	2.900 (0.200)	3.100 (0.210)	2.750 (0.055)	2.733 (0.216)	2.783 (0.223)	2.917 (0.223)	2.667 (0.216)	2.600 (0.126)	2.917 (0.117)	2.750 (0.243)	2.700 (0.420)	2.783 (0.194)
ALP (U/l)	200.67 (29.49)	253.50 (28.81)	207.50 (36.30)	183.67 (45.70)	195.50 (45.05)	141.17 (30.64)	177.83 (41.80)	163.50 (28.39)	192.17 (40.63)	204.00 (46.43)	227.83 (51.34)	200.00 (36.78)
ALT (U/l)	89.67 (7.74)	88.17 (6.68)	90.33 (8.55)	75.00 (8.60)	76.67 (13.31)	69.50 (3.78)	87.50 (22.82)	85.50 (7.23)	89.83 (15.96)	85.83 (10.46)	78.83 (8.11)	89.67 (11.27)
Amylase (U/l)	2182.17 (119.59)	2054.5 (333.84)	2019.67 (209.93)	1706.67 (256.08)	1335.00 (246.33)	1487.50 (155.96)	1779.00 (189.74)	1589.50 (232.52)	1764.17 (188.13)	1893.17 (226.83)	1742.00 (504.32)	1945.67 (219.46)
AST (U/l)	81.33 (16.67)	78.33 (9.42)	80.83 (12.95)	91.50 (12.42)	115.00 (42.68)	88.33 (17.10)	97.83 (23.70)	71.50 (10.88)	98.00 (11.51)	73.00 (9.38)	85.50 (10.58)	83.50 (14.15)
Bilirubin (mg/dl)	19.67 (1.37)	21.83 (1.47)	23.33 (1.86)	23.33 (2.25)	24.00 (1.67)	20.67 (1.03)	21.67 (1.63)	19.33 (1.03)	22.83 (1.47)	21.67 (1.86)	29.67 (14.60)	22.33 (2.07)
Calcium (mg/dl)	11.18 (0.70)	10.78 (0.23)	10.63 (0.15)	10.28 (0.16)	10.32 (0.23)	10.60 (0.23)	10.47 (0.22)	10.57 (0.29)	10.35 (0.25)	10.52 (0.22)	10.58 (0.26)	10.80 (0.27)
Cholesterol (mg/dl)	87.17 (17.97)	87.50 (13.07)	81.00 (7.69)	99.33 (14.31)	106.83 (13.12)	95.33 (7.31)	83.00 (20.95)	83.83 (9.81)	82.33 (7.45)	90.50 (17.07)	93.17 (16.10)	84.33 (15.34)
Creatine Kinase (U/l)	105.83 (11.86)	94.67 (12.04)	104.50 (36.54)	426.5 (72.45)	403.50 (146.06)	153.00 (119.30)	302.50 (132.63)	115.67 (55.85)	346.33 (117.08)	83.50 (35.80)	244.83 (110.49)	94.83 (22.48)
Creatinine (mg/dl)	0.283 (0.041)	0.383 (0.041)	0.383 (0.041)	0.383 (0.041)	0.400 (0.063)	0.333 (0.082)	0.433 (0.234)	0.367 (0.052)	0.400 (0)	0.350 (0.055)	1.700 (3.184)	0.400 (0)
Glucose (mg/dl)	181.00 (18.98)	187.33 (3.44)	283.33 (52.30)	225.17 (48.06)	251.00 (77.69)	226.33 (39.62)	243.17 (127.82)	275.83 (33.58)	209.83 (23.20)	255.83 (58.81)	223.83 (62.07)	295.83 (40.92)
Phosphorus (mg/dl)	5.983 (0.313)	5.767 (0.497)	5.300 (0.498)	5.567 (0.383)	5.533 (0.524)	5.700 (0.704)	5.733 (0.625)	5.250 (0.367)	5.983 (0.417)	5.700 (0.228)	6.500 (1.942)	5.467 (0.372)
T. Bilirubin (mg/dl)	0.167 (0.052)	0.117 (0.041)	0.167 (0.082)	0.117 (0.041)	0.217 (0.240)	0.400 (0.642)	0.250 (0.207)	0.167 (0.103)	0.183 (0.075)	0.200 (0.155)	0.150 (0.122)	0.217 (0.117)
Total Protein (g/dl)	6.517 (0.256)	6.550 (0.217)	6.017 (0.117)	6.217 (0.343)	6.267 (0.344)	6.467 (0.484)	6.233 (0.207)	5.850 (0.207)	6.300 (0.141)	6.183 (0.204)	6.150 (0.689)	6.067 (0.314)
Globulin (g/dl)	3.617 (0.407)	3.483 (0.041)	3.283 (0.147)	3.467 (0.186)	3.483 (0.133)	3.567 (0.273)	3.533 (0.695)	3.250 (0.152)	3.400 (0.632)	3.383 (0.117)	3.560 (0.114)	3.300 (0.141)

* All comparisons to collagen group. n=6/group. The number in this table demonstrates the average value of parameters from the each group and the number in the parentheses refers to the standard deviations. No significant differences were noted among the AdPDGF-B and collagen matrix groups during early time points, as well as beyond 14 days (data not shown). *Abbreviations used: Col:collagen matrix only group, L-Ad: $5.5x10^8$ PFU/ml AdPDGF-B treated group, H-Ad: $5.5x10^9$ PFU/ml AdPDGF-B treated group; ALP: alkaline phosphatase; ALT: alanine transaminase; AST: aspartate transaminase; T. Bilirubin: total bilirubin*

4.9 Figures

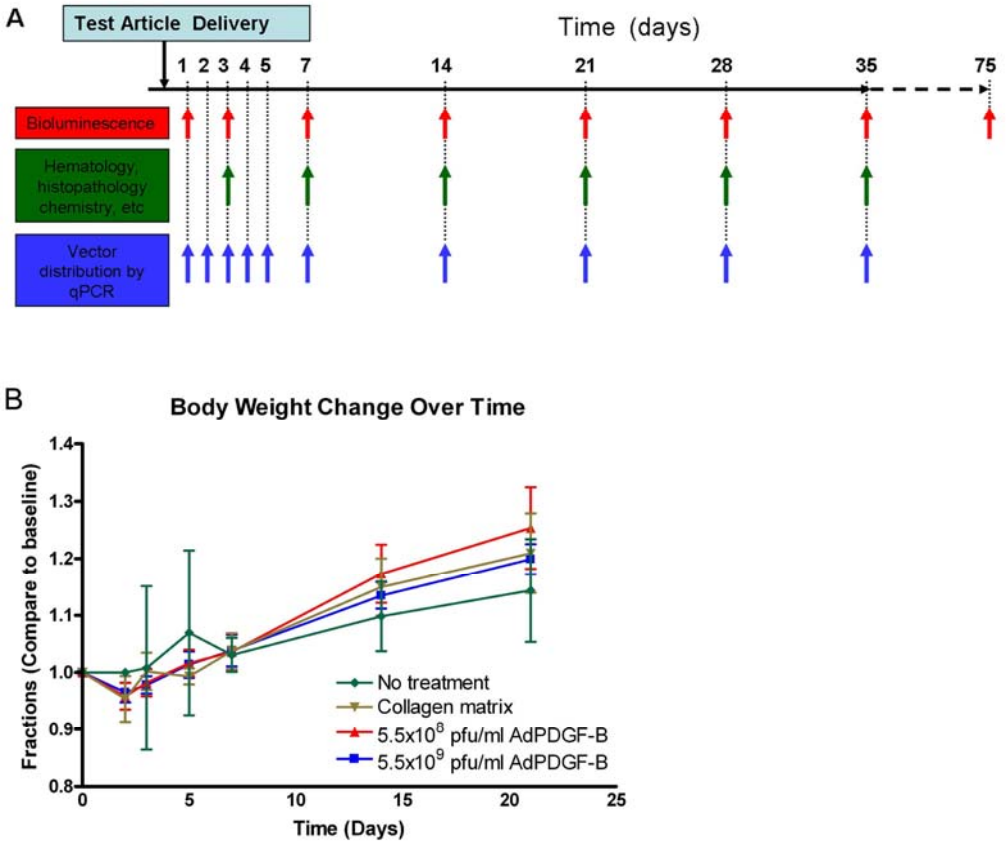

Fig 4.1 General study design and body weight change over time. (**A**) Five treatment groups ($5.5x10^8$ pfu/ml AdLuc/collagen, $5.5x10^9$ pfu/ml AdLuc/collagen, $5.5x10^8$ pfu/ml AdPDGF-B/collagen, $5.5x10^9$ pfu/ml AdPDGF-B/collagen, and collagen matrix only) were investigated. The observation time points were over a period of 35 days on a weekly basis while 2 animals in $5.5x10^9$ pfu/ml AdLuc/collagen group were observed for 75 days. Non-treated animals (neither surgical defect nor adenovirus-collagen mixture application) were also included in experiment of systemic involvement and clinical observation. (**B**) All the surgically-treated animals experienced transient body weight loss in the first few days post-treatment but thereafter continuously gained weight throughout the study period.

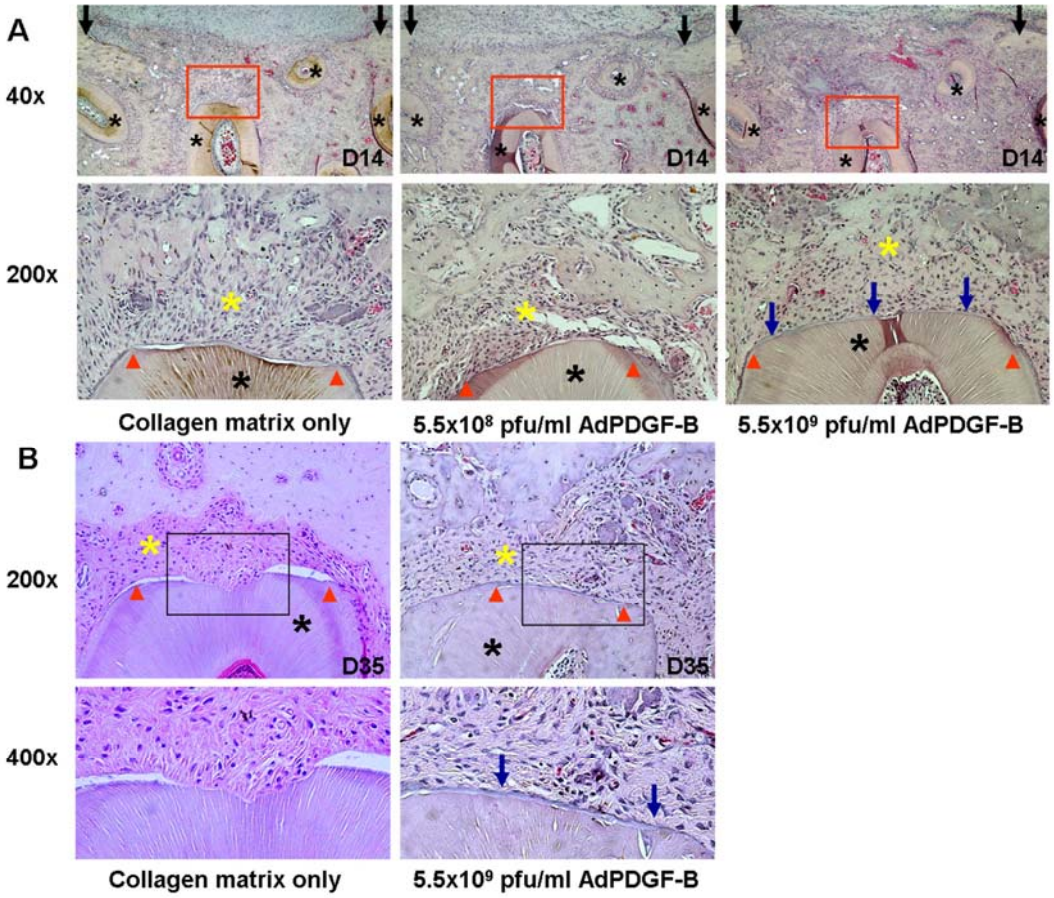

Fig 4.2 PDGF Gene Delivery Promotes Periodontal Tissue Regeneration *in vivo*. (**A**) Limited bone formation and bridging occurred in the wound treated by collagen matrix only compared to AdPDGF-B/collagen treated defects at 14 days. More newly-formed cementum structure (blue arrows) was observed in high-dose ($5.5x10^9$ pfu/ml) AdPDGF-B/collagen treated sites. Inset red boxes demonstrate higher magnification images of tooth/cementum/periodontal ligament (PDL)/bone interfaces. (**B**) At 35 days, $5.5x10^9$ pfu/ml AdPDGF-B treated defect demonstrated significant amount of root cementum compared to the defect treated by collagen matrix only. Red arrowheads indicate the edges of exposed tooth dentin surface, blue arrows as new cementum, black asterisks as tooth roots, and yellow asterisks as the area of PDL. (All the images are in transverse orientation and stained by hematoxylin and eosin).

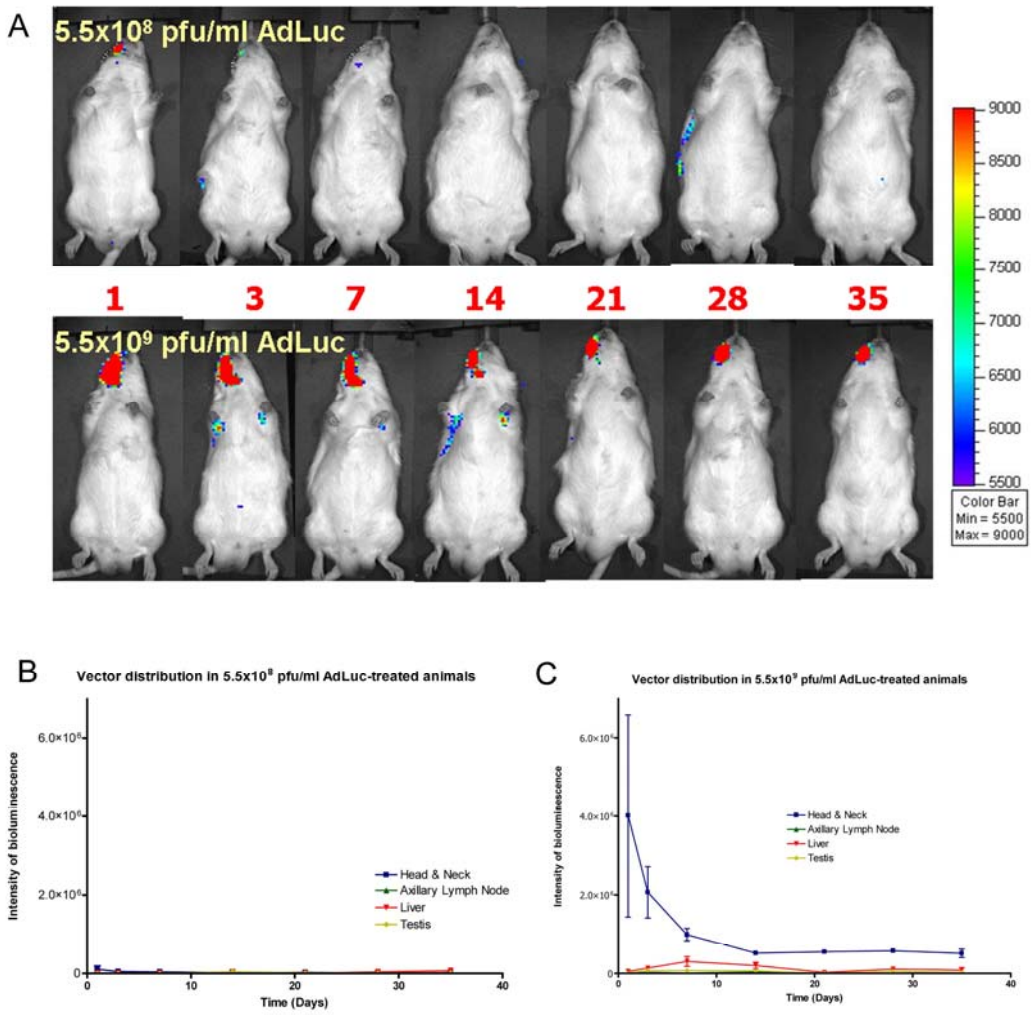

Fig 4.3. Vector Transduction Efficiency and Systemic Distribution from Bioluminescence (**A**) Majority of the luciferin signal is restricted within the alveolar bone defect region with minimal systemic involvement. The signals in distant organs were absent after 14 days for both dose level groups. (**B**) Mild vector expression was noted in the animals treated by $5.5x10^8$ pfu/ml AdLuc during the first 3-7 days. (**C**) $5.5x10^9$ pfu/ml AdLuc-treated animals demonstrated significant vector expression during the first 14 days, followed by a decrease of vector expression in the head and neck region over time. The high dose group also showed modest vector expression in liver (1/6 positive at day 14) and axillary lymph nodes (1/6 positive at day 3, and 2/6 positive at both day 7 and 10). The n value of each treatment group is 6 (3 per gender). The intensity of bioluminescence within the region-of-interest below 5,000 p/sec/cm^2/sr in each selected region was defined as "negative" (N).

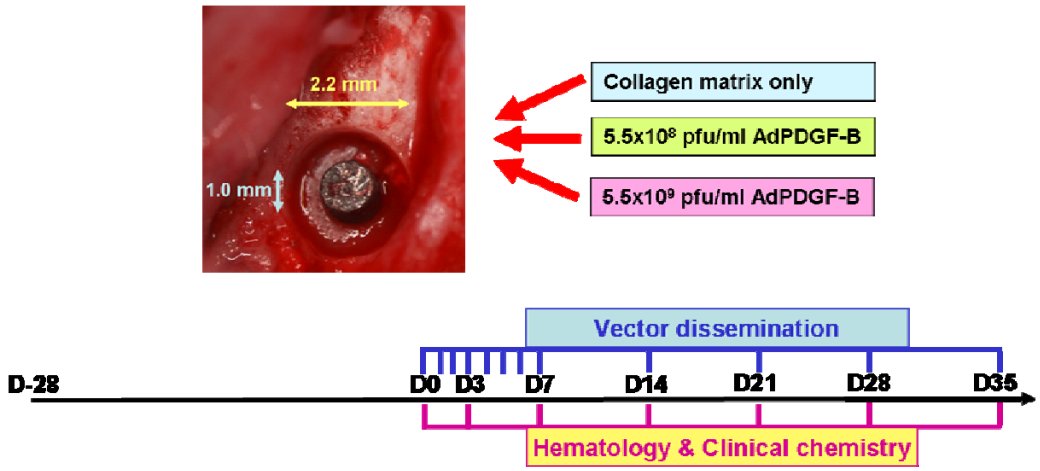

Figure 4.4 General Study Design and Timeline of Maxillary Peri-implant Safety

The maxillary first molars were extracted 28 days prior to implant surgery. During implantation, the 1 mm in diameter and 2 mm in depth cylinder type titanium implant was placed on the rat maxillae and 2.2 mm in diameter and 1 mm in depth osteotomy was created to achieve a 0.6x1 mm peri-implant circumferential bony defect. The defect was then filled with collagen matrix alone or matrix containing $5.5x10^8$ or $5.5x10^9$ pfu/ml AdPDGF-B. Within a observation period of 35 days, the vector dissemination was examined through qPCR from the blood DNA, and hematology and clinical chemistry were evaluated to determine the possible systemic involvements.

4.10 References

1. Andrae, J., Gallini, R. & Betsholtz, C. Role of platelet-derived growth factors in physiology and medicine. *Genes Dev* **22**, 1276-312 (2008).
2. Southwood, L.L., Frisbie, D.D., Kawcak, C.E. & McIlwraith, C.W. Delivery of growth factors using gene therapy to enhance bone healing. *Vet Surg* **33**, 565-78 (2004).
3. Ronnstrand, L. & Heldin, C.H. Mechanisms of platelet-derived growth factor-induced chemotaxis. *Int J Cancer* **91**, 757-62 (2001).
4. Fiedler, J., Etzel, N. & Brenner, R.E. To go or not to go: Migration of human mesenchymal progenitor cells stimulated by isoforms of PDGF. *J Cell Biochem* **93**, 990-8 (2004).
5. Haase, H.R., Clarkson, R.W., Waters, M.J. & Bartold, P.M. Growth factor modulation of mitogenic responses and proteoglycan synthesis by human periodontal fibroblasts. *J Cell Physiol* **174**, 353-61 (1998).
6. Karimbux, N.Y., Sirakian, A., Weber, H.P. & Nishimura, I. A new animal model for molecular biological analysis of the implant-tissue interface: spatial expression of type XII collagen mRNA around a titanium oral implant. *J Oral Implantol* **21**, 107-13; discussion 114-5 (1995).
7. Zaman, K.U., Sugaya, T. & Kato, H. Effect of recombinant human platelet-derived growth factor-BB and bone morphogenetic protein-2 application to demineralized dentin on early periodontal ligament cell response. *J Periodontal Res* **34**, 244-50 (1999).
8. Cooke, J.W. et al. Effect of rhPDGF-BB delivery on mediators of periodontal wound repair. *Tissue Eng* **12**, 1441-50 (2006).
9. Park, J.Y. & Davies, J.E. Red blood cell and platelet interactions with titanium implant surfaces. *Clin Oral Implants Res* **11**, 530-9 (2000).
10. Nevins, M. et al. Platelet-derived growth factor stimulates bone fill and rate of attachment level gain: results of a large multicenter randomized controlled trial. *J Periodontol* **76**, 2205-15 (2005).
11. Ramseier, C.A., Abramson, Z.R., Jin, Q. & Giannobile, W.V. Gene therapeutics for periodontal regenerative medicine. *Dent Clin North Am* **50**, 245-63, ix (2006).
12. Chandler, L.A. et al. FGF2-Targeted adenovirus encoding platelet-derived growth factor-B enhances de novo tissue formation. *Mol Ther* **2**, 153-60 (2000).
13. Dunn, C.A. et al. BMP gene delivery for alveolar bone engineering at dental implant defects. *Mol Ther* **11**, 294-9 (2005).
14. Fromigue, O., Modrowski, D. & Marie, P.J. Growth factors and bone formation in osteoporosis: roles for fibroblast growth factor and transforming growth factor beta. *Curr Pharm Des* **10**, 2593-603 (2004).
15. Chen, Q.P. & Giannobile, W.V. Adenoviral gene transfer of PDGF downregulates gas gene product PDGFalphaR and prolongs ERK and Akt/PKB activation. *Am J Physiol Cell Physiol* **282**, C538-44 (2002).
16. Voutetakis, A. et al. Sorting of transgenic secretory proteins in rhesus macaque parotid glands following adenoviral mediated gene transfer. *Hum Gene Ther* (2008).
17. Cotrim, A.P., Sowers, A., Mitchell, J.B. & Baum, B.J. Prevention of irradiation-induced salivary hypofunction by microvessel protection in mouse

salivary glands. *Mol Ther* **15**, 2101-6 (2007).
18. Jin, Q., Anusaksathien, O., Webb, S.A., Printz, M.A. & Giannobile, W.V. Engineering of tooth-supporting structures by delivery of PDGF gene therapy vectors. *Mol Ther* **9**, 519-26 (2004).
19. Lan, J., Wang, Z., Wang, Y., Wang, J. & Cheng, X. The effect of combination of recombinant human bone morphogenetic protein-2 and basic fibroblast growth factor or insulin-like growth factor-I on dental implant osseointegration by confocal laser scanning microscopy. *J Periodontol* **77**, 357-63 (2006).
20. Huang, Y.C., Kaigler, D., Rice, K.G., Krebsbach, P.H. & Mooney, D.J. Combined angiogenic and osteogenic factor delivery enhances bone marrow stromal cell-driven bone regeneration. *J Bone Miner Res* **20**, 848-57 (2005).
21. Ni, S. et al. Evaluation of biodistribution and safety of adenovirus vectors containing group B fibers after intravenous injection into baboons. *Hum Gene Ther* **16**, 664-77 (2005).
22. Lenaerts, L., Verbeken, E., De Clercq, E. & Naesens, L. Mouse adenovirus type 1 infection in SCID mice: an experimental model for antiviral therapy of systemic adenovirus infections. *Antimicrob Agents Chemother* **49**, 4689-99 (2005).
23. Nunes, F.A., Furth, E.E., Wilson, J.M. & Raper, S.E. Gene transfer into the liver of nonhuman primates with E1-deleted recombinant adenoviral vectors: safety of readministration. *Hum Gene Ther* **10**, 2515-26 (1999).
24. Wang, Y. et al. Characterisation of systemic dissemination of nonreplicating adenoviral vectors from tumours in local gene delivery. *Br J Cancer* **92**, 1414-20 (2005).
25. Manickan, E. et al. Rapid Kupffer cell death after intravenous injection of adenovirus vectors. *Mol Ther* **13**, 108-17 (2006).
26. Hackett, N.R. et al. Use of quantitative TaqMan real-time PCR to track the time-dependent distribution of gene transfer vectors in vivo. *Mol Ther* **2**, 649-56 (2000).
27. Garrison, R. Amylase. *Emerg Med Clin North Am* **4**, 315-27 (1986).
28. Tietz, N.W., Huang, W.Y., Rauh, D.F. & Shuey, D.F. Laboratory tests in the differential diagnosis of hyperamylasemia. *Clin Chem* **32**, 301-7 (1986).
29. Kwok, A.W., Finkelstein, J.A., Woodside, T., Hearn, T.C. & Hu, R.W. Insertional torque and pull-out strengths of conical and cylindrical pedicle screws in cadaveric bone. *Spine* **21**, 2429-34 (1996).
30. Nash, T.J. et al. Effect of platelet-derived growth factor on tibial osteotomies in rabbits. *Bone* **15**, 203-8 (1994).
31. Honigman, A. et al. Imaging transgene expression in live animals. *Mol Ther* **4**, 239-49 (2001).
32. Green, R.J., Usui, M.L., Hart, C.E., Ammons, W.F. & Narayanan, A.S. Immunolocalization of platelet-derived growth factor A and B chains and PDGF-alpha and beta receptors in human gingival wounds. *J Periodontal Res* **32**, 209-14 (1997).
33. Sakurai, H., Kawabata, K., Sakurai, F., Nakagawa, S. & Mizuguchi, H. Innate immune response induced by gene delivery vectors. *Int J Pharm* **354**, 9-15 (2008).
34. Schagen, F.H., Ossevoort, M., Toes, R.E. & Hoeben, R.C. Immune responses against adenoviral vectors and their transgene products: a review of strategies for evasion. *Crit Rev Oncol Hematol* **50**, 51-70 (2004).

35. Koizumi, N. et al. Fiber-modified adenovirus vectors decrease liver toxicity through reduced IL-6 production. *J Immunol* **178**, 1767-73 (2007).
36. Xu, X.L. et al. Immune response and effect of adenovirus-mediated human BMP-2 gene transfer on the repair of segmental tibial bone defects in goats. *Acta Orthop* **76**, 637-46 (2005).
37. Li, J.L. et al. A phase I trial of intratumoral administration of recombinant oncolytic adenovirus overexpressing HSP70 in advanced solid tumor patients. *Gene Ther* **16**, 376-82 (2009).
38. Michou, A.I. et al. Adenovirus-mediated gene transfer: influence of transgene, mouse strain and type of immune response on persistence of transgene expression. *Gene Ther* **4**, 473-82 (1997).
39. Benihoud, K. et al. Efficient, repeated adenovirus-mediated gene transfer in mice lacking both tumor necrosis factor alpha and lymphotoxin alpha. *J Virol* **72**, 9514-25 (1998).
40. Ilan, Y. et al. Oral tolerization to adenoviral antigens permits long-term gene expression using recombinant adenoviral vectors. *J Clin Invest* **99**, 1098-106 (1997).
41. Yang, Y., Trinchieri, G. & Wilson, J.M. Recombinant IL-12 prevents formation of blocking IgA antibodies to recombinant adenovirus and allows repeated gene therapy to mouse lung. *Nat Med* **1**, 890-3 (1995).
42. Haegel-Kronenberger, H. et al. Inhibition of costimulation allows for repeated systemic administration of adenoviral vector in rhesus monkeys. *Gene Ther* **11**, 241-52 (2004).
43. Parks, R., Evelegh, C. & Graham, F. Use of helper-dependent adenoviral vectors of alternative serotypes permits repeat vector administration. *Gene Ther* **6**, 1565-73 (1999).

CHAPTER 5

SUMMARY AND FUTURE WORK

5.1 Summary

There are three main aspects which have been addressed in this dissertation: a FE optimization process to represent the structural and functional dynamics of implant osseointegration; an investigation on PDGF delivery to accelerate osseointegration; and a study on evaluation of systemic preclinical safety profile of localized adenovirus-mediated gene therapy.

Restoration of masticatory function is one of the primary reasons for using dental implants. Their main functional capability is believed to rely on the biomechanical properties of implant-supporting tissues. The main contribution of **Chapter 2** was to confirm the importance of peri-implant structures on the process of osseointegration through functionally homogenizing the peri-implant tissue. Micro-CT images were

utilized, because they are the only available technique which provides spatial information of mineralization while also being favorable for evaluating peri-implant tissue based on the insignificant, yet radiographically visible damage following implant removal. The homogenization of peri-implant tissue can be achieved by convergence of the results from FEA under presumptive tissue properties, functional loads, and boundary conditions. Functional apparent moduli (FBAM and FCAM) generated via this optimization process were more correlated to each structural parameter than was mathematical moduli. Furthermore, while current clinical measurements provide limited functional information without comparable structural information of osseointegration, in **Chapter 2** the most functionally-relevant peri-implant segment was also identified using layer-by-layer structural and functional comparisons. Based on the micro-CT measurements, the strongest functional-relevant area was within 200 μm from the implant surface, and tended to increase with pre-existing circumferential osseous defects. The functional apparent moduli offer a better match to the interfacial biomechanics and restrict the strongest functional-relevant area to a 200 μm thickness with the existence of osseous defects by FCAM. Under the influence of metal scattering effects from micro-CT images (108-162 μm concentric area), the functional-relevance is still valid within 250 μm peri-implant layers. This ‘critical’ functionally-relevant area is thought to have clinical

significance during the healing and prognosis evaluation of osseointegration.

For the second part of my dissertation, in **Chapter 3**, I validated that PDGF gene delivery is a feasible approach to accelerate implant osseointegration. Although prolonged PDGF expression via gene delivery may affect the progression of differentiation *in vitro*. The effect may insure persistent recruitment of mesenchymal stem cells (MSCs) or osteoprogenitor cells during early wound healing and remain supportive for further bone regeneration *in vivo*. This dissertation reported that delivery of recombinant PDGF protein (rhPDGF-BB) can accelerate early peri-implant osseous wound repair based on two-dimensional, three-dimensional, and functional evaluations. The therapeutic effect of Ad-mediated PDGF gene (AdPDGF-B) delivery was dose-dependent, with $2.5x10^{11}$ vp/ml AdPDGF-B exhibiting more favorable osteogenesis than $2.5x10^{10}$ vp/ml, possibly indicating the minimal effective dose of AdPDGF-B treatment. AdPDGF-B also demonstrated a comparable tendency as rhPDGF-BB for osseous wound fill, however, the functional resistance tended to be weaker during early healing, due to considerable amounts of PDGF affecting delayed maturation of newly-regenerated bone which later recovered. Thus, PDGF demonstrated its promotive effects during early osseointegration, and the dosage and temporal expression profiles

play determinable roles on the progress of functional recovery.

The major contribution of the third portion of this dissertation was to confirm the safety profile of AdPDGF-B delivery for dental use. In **Chapter 4**, I revealed that most of the vectors were eliminated with very minimal systemic leakage. The local existence and expression of vector was rapidly cleared within two weeks without compromising the healing capabilities. Systemically, neither significant vector dissemination nor vector-related pathologic changes were observed, indicating an acceptable preclinical safety profile. Thus, AdPDGF-B is considered safe when using the therapeutic dose for oral wound healing applications.

In summary, this dissertation has developed a working methodology in order to radiographically, and functionally, evaluate the dynamics of oral implant osseointegration. Based on this approach, we have demonstrated that PDGF is feasible to accelerate oral implant osseointegration via gene delivery without eliciting any significant safety concerns.

5.2 Future Work

In this dissertation, we have validated the concept that functional homogenization of peri-implant tissue can reflect the growth pattern of implant-supporting tissues as well as the biomechanical resistance of the interface within a specific range of tissue. Based on the described methodology, it is possible and therefore necessary to advance to a large animal model in order to utilize a clinically-designed implant system which can gather more clinically relevant information. However, to simplify the iterative process, we technically homogenized the three dimensional structure to a single plane and assumed micro-isotropic properties projected from a previous reference. Therefore, the resolution of the clinically-available computed tomography system is quite limited (~100 μm) such that any unrealistic assumption may cause significant deviation from actual circumstances. Thus, establishment of a three-dimensional FE model will allow further consideration for the properties of bone tissue and prove more relevant for clinical diagnostic purposes.

The differential osteopromotive effects *in situ* of PDGF recombinant protein and gene delivery implies that the temporal PDGF expression profile may influence the progress of osseointegration. Further confirmation of this hypothesis *in vitro* is necessary

for understanding the specific osteoconductive mechanisms of PDGF. We will also attempt to investigate compromised conditions, such as within a diabetic or geriatric model, due to the short observation window in the described model.

We have demonstrated an acceptable preclinical safety profile of AdPDGF-B within the aspects of vector kinetics. Additional work on vector-related immunogenicity and carcinogenesis will be proposed to provide further safety information. Finally, we will investigate the most effective, therapeutic, and safe dose of AdPDGF-B within a large animal model to ultimately develop AdPDGF-B therapy for human clinical applications.